

VESSEL BIFURCATION DETECTION IN SCALE SPACE

by

Daniel-Marian Baboiu

MSc in Physics, University of Bucharest, 1991

PhD in Physics, University of Central Florida, 1998

A THESIS SUBMITTED IN PARTIAL FULFILLMENT
OF THE REQUIREMENTS FOR THE DEGREE OF
MASTER OF SCIENCE
in the School
of
Computing Science

© Daniel-Marian Baboiu 2011
SIMON FRASER UNIVERSITY
Spring 2011

All rights reserved. However, in accordance with the Copyright Act of Canada, this work may be reproduced without authorization under the conditions for Fair Dealing. Therefore, limited reproduction of this work for the purposes of private study, research, criticism, review and news reporting is likely to be in accordance with the law, particularly if cited appropriately.

APPROVAL

Name: Daniel-Marian Baboiu

Degree: Master of Science

Title of Thesis: Vessel Bifurcation Detection in Scale Space

Examining Committee: Bradley Bart, Senior Lecturer,
Computing Science, Simon Fraser University
Chair

Dr. Ghassan Hamarneh, Associate Professor,
Computing Science, Simon Fraser University
Senior Supervisor

Dr. Brian Funt, Professor,
Computing Science, Simon Fraser University
Supervisor

Dr. Mark S. Drew, Professor,
Computing Science, Simon Fraser University
Examiner

Date Approved: March 3, 2011



SIMON FRASER UNIVERSITY
LIBRARY

Declaration of Partial Copyright Licence

The author, whose copyright is declared on the title page of this work, has granted to Simon Fraser University the right to lend this thesis, project or extended essay to users of the Simon Fraser University Library, and to make partial or single copies only for such users or in response to a request from the library of any other university, or other educational institution, on its own behalf or for one of its users.

The author has further granted permission to Simon Fraser University to keep or make a digital copy for use in its circulating collection (currently available to the public at the "Institutional Repository" link of the SFU Library website <www.lib.sfu.ca> at: <<http://ir.lib.sfu.ca/handle/1892/112>>) and, without changing the content, to translate the thesis/project or extended essays, if technically possible, to any medium or format for the purpose of preservation of the digital work.

The author has further agreed that permission for multiple copying of this work for scholarly purposes may be granted by either the author or the Dean of Graduate Studies.

It is understood that copying or publication of this work for financial gain shall not be allowed without the author's written permission.

Permission for public performance, or limited permission for private scholarly use, of any multimedia materials forming part of this work, may have been granted by the author. This information may be found on the separately catalogued multimedia material and in the signed Partial Copyright Licence.

While licensing SFU to permit the above uses, the author retains copyright in the thesis, project or extended essays, including the right to change the work for subsequent purposes, including editing and publishing the work in whole or in part, and licensing other parties, as the author may desire.

The original Partial Copyright Licence attesting to these terms, and signed by this author, may be found in the original bound copy of this work, retained in the Simon Fraser University Archive.

Simon Fraser University Library
Burnaby, BC, Canada

Abstract

Several methods have been proposed for segmentation of vessels, many based on scale-space. However, none of the existing methods for blood vessel segmentation is appropriate for extension to bifurcation detection. Existing bifurcation detection algorithms use an inherently serial track and detect approach, requiring a seed point. We present a comprehensive scale space analysis of vascular bifurcations, resulting in a simple, novel algorithm for direct detection of blood vessel bifurcation points based not only on spatial variation across scales, but also on the variation at a single spatial point across scales, without training data or seed points. We present an analytical model for the bifurcation evolution with scale, combined with eigenvalue analysis to create a "bifurcationness" filter. We reveal, for the first time, a hybrid structure of bifurcations in scale-space. The algorithm was tested for validation in both 2D and 3D, with synthetic data and medical images.

Keywords: scale-space, bifurcation detection, Hessian eigenvalue, multiscale, interest points, vascular enhancement, codimension, local features

Index of Notations

Notation	Use
I	Signal intensity in the image; also used to represent the image as a whole
$I(x, y)$	Signal intensity at pixel (x, y)
L	The scale space family of the image
σ	Scale
s	Scale parameter, $s = \sigma^2$
w	width or characteristic width of an image feature
$L(\mathbf{x}, s)$ or $L(\mathbf{x}, \sigma)$	Intensity of the point at \mathbf{x} in the scale space, at scale σ or scale parameter s ($s = \sigma^2$). Unless otherwise specified, roman letters are the variance, while greek letters are used for the standard deviation, or width of the kernel
\mathcal{H}	The Hessian operator. Used with argument, $\mathcal{H}(I)$, or without argument, as a simplification
DoH	Determinant of Hessian, $\text{Det}(\mathcal{H})$
λ_i	The i -th eigenvalue of a tensor
\hat{e}_i	Unit vector
$L_0, L(\mathbf{x}, 0)$	The first slice in the scale space of the image. Identical with the original image.
I_x, L_x, I_{xy} , etc	Coordinate variables used as subscript mean the partial derivative of the corresponding quantity with respect to that coordinate. Multiple subscripts may be used to signify higher order derivatives.
δ	Codimension
D	Number of dimensions of an image

Notation	Use
Λ	The quantity used to calculate the codimension, either scale-space intensity or its non-scale-normalized Laplacean
α	Bifurcation ratio: the diameter ratio of the smaller daughter vessel and the larger daughter vessel

Contents

Approval	ii
Abstract	iii
Index of Notations	iv
Contents	vi
List of Tables	viii
List of Figures	ix
List of Listings	xi
1 Introduction	1
1.1 Interest Points in Image Processing	3
1.2 Our Approach	7
2 Introduction to Scale-Space	9
2.1 The Concept of Scale-Space	9
2.2 Properties of Scale-Space	13
3 Vessels and Bifurcations in Scale-Space	16
3.1 Tensorial Description of Vascular Structures	16
3.2 Vessel Response in Scale Space	19
3.3 Bifurcation Response in Scale-Space	32

4	Implementation of the Bifurcation Detector	36
4.1	First Implementation	37
4.2	Eigenvalue Analysis of Vascular Bifurcations	40
4.2.1	Eigenvalue Analysis in 2D	40
4.2.2	Eigenvalue Analysis in 3D	43
4.3	Comparison with corner detectors	51
4.4	Computation Cost	61
4.5	Conclusion	62
5	Results	64
5.1	Statistics of 2D Bifurcation Detection	66
5.2	Localization Errors	75
5.3	Results on Clinical Data	78
5.4	Results in 3D	80
5.5	Limitations	83
6	Conclusion and Future Directions	86
A	Geometry of Vascular Bifurcations	89
A.1	Bifurcation Ratio	90
A.2	Bifurcation angles	92
B	Helper Routines	98
B.1	Drawing a Cylinder in Matlab	98
B.1.1	Geometry	98
B.1.2	Matlab Implementation	99
B.2	Generating a 2D Bifurcation	103
B.3	Local Maxima in Matlab	104
C	Analysis of the Frangi Vesselness	106
	Bibliography	115

List of Tables

3.1	Summary of formulae for calculating codimension using scale-space variation in intensity and Laplacian	28
4.1	Possible patterns of bright structures in 2D and 3D, based on Hessian eigenvalues and codimension	38
4.2	Eigenvalue functions for 2D bifurcations, filtered for areas with all eigenvalues negative	41
4.3	Eigenvalue functions for 3D bifurcations (sections), filtered for areas with all eigenvalues negative.	44
4.4	Eigenvalue functions for 3D bifurcations (isosurfaces), filtered for areas with all eigenvalues negative.	45
4.5	Detectors for 3D bifurcations (sections), filtered for areas with all eigenvalues negative.	46
4.6	Detectors for 3D bifurcations (isosurfaces)	47

List of Figures

2.1	Evolution of two Gaussian structures in scale-space	14
2.2	Evolution of two rectangular profiles in scale-space	14
3.1	Decomposing a symmetric tensor (top) into its components	18
3.2	Frangi's vesselness applied to a synthetic bifurcation	19
3.3	Geometry for calculating scale-space response of a vessel	20
3.4	Decay of intensity at the center of vessel with scale	22
3.5	Codimension for 2D structures	30
3.6	Codimension for 3D structures	31
3.7	A simple model of a vascular bifurcation, represented as a set of three simple straight vessels, in both 2D and 3D	32
3.8	Scale space response of an ideal 2D bifurcation	33
3.9	Influence of deviation from mathematical model on bifurcation response in scale-space	35
4.1	Initial images for testing detectors	54
4.2	Response of corner detectors for a 2D synthetic symmetric bifurcation	55
4.3	Response of corner detectors for a 2D synthetic strongly asymmetric bifurcation	56
4.4	Response of corner detectors for a 2D noisy angiogram	58
4.5	Response of corner detectors for a retinal image	60
5.1	Bifurcation detection results on a fractal tree	65
5.2	Bifurcation detection on a fractal tree with noise	66
5.3	2D Test bifurcations without noise	67
5.4	2D Test bifurcations with low Gaussian noise	68
5.5	2D Test bifurcations with high Gaussian noise	69

5.6	2D Test bifurcations with low Salt&Pepper noise	70
5.7	2D Test bifurcations with high Salt&Pepper noise	71
5.8	95% detectability areas for synthetic bifurcations with Gaussian noise	73
5.9	95% detectability areas for synthetic bifurcations with Salt and Pepper noise	74
5.10	Bifurcation detection: distribution of location errors	76
5.11	Bifurcation detection: normalized location errors	77
5.12	Displacement of the detected position of a symmetric bifurcation with scale	78
5.13	Results of applying the bifurcation detection to a retinal image	79
5.14	DRIVE retinal image processed for bifurcation detection	80
5.15	The original Luboz phantom, embedded in a block	81
5.16	Bifurcations detected in a 3D phantom	82
5.17	An illustration of detected bifurcations in 3D	84
5.18	Difficult situations in retinal images	85
5.19	Overlap of bifurcation and crossing in retinal images	85
A.1	Data and regression line obtained for 160 paired flow-diameter measurement	91
A.2	Measurements of branch diameters in different parts of the arterial tree by Zamir	93
A.3	Small displacements are applied to the bifurcation point to obtain the optimality condition.	94
A.4	Measurements of the branching angles from the arterial tree of a rat compared with theoretical curves	96
A.5	Measurements of the angle between the daughter branches compared with theoretical curves	96
A.6	Measurements of the angle between the parent vessel and the plane of the daughter vessels.	97
B.1	Geometry used for generating a single cylinder image	99
C.1	Comparison of vesselness enhancement filters	110
C.2	Transfer function for the Gaussian penalty and the linear transfer	112
C.3	Comparison of vesselness enhancement filters applied retinal image	113
C.4	Comparison of vesselness enhancement filters applied synthetic 3D bifurcation	113

List of Listings

- B.1 Matlab routine used to generate a single bifurcation branch 100
- B.2 Generating a bifurcation in 2D 103
- B.3 Detecting local maxima in Matlab 104

Chapter 1

Introduction

An increasingly aging population leads to an increased necessity for medical diagnosis. This, combined with a chronic deficit of qualified medical personnel and with the ever increasing volume of data from modern medical equipment, leads to the necessity to automate diagnosis as much as possible. Many times, the relevant medical data is drowned not only in noise from the data acquisition equipment, but also in real data with little or no relevance to the task at hand. Blood vessels are a prime candidate for automation, as cardiac vascular accidents are a leading cause of death, and brain vascular accidents are, if not deadly, at least with extremely severe consequences. The bifurcations of blood vessels are of particular interest, since clinical studies (see, e.g., [50, 45] and references therein), as well as numerical simulations [19], showed that blood vessel bifurcations are a major site for occurrence of cardiovascular diseases; for example, extracranial bifurcation arteriosclerosis is likely a common cause of stroke. Blood flow reaching a bifurcation creates an area of low velocity and high pressure [19] as well as areas of high shear [19, 18], generating turbulence even in continuous flow [18]. In support of a hemodynamic effect is the well-defined tendency for plaques to occur at the ostia of the vessels arising from the aorta, branch points, and along the posterior wall of the abdominal aorta where there are disturbed flow patterns. Areas of disturbed, turbulent flow and low shear stress are prone to arteriosclerosis, while those with smooth, laminar flow seem protected [24]. Alterations in the functions of vascular endothelial cells induced by fluid shear stress may play a pivotal role in both the development and prevention of vascular diseases; these results suggest that steady laminar shear stress induces cell cycle arrest. Derangement of the steady laminar flow may release cells from this inhibition and induce cell proliferation, which, in turn, may cause atherosclerosis through the induction

of EC stability disruption [2]. To this day, bifurcation lesions, especially in the coronary setting, are among the most challenging lesions for diagnosis and treatment, and is one of the fields still in search of a major advance[10].

Automatic detection of bifurcations is important for non-medical reasons as well, most importantly for person authentication via biometrics. Some of the modern personal authentication devices use the retina blood vessel pattern. This is a unique pattern in each individual and it is almost impossible to forge a pattern in a false individual. This pattern does not change over the life of the individual, unless a serious pathology appears in the eye. In most common diseases, the topology is not affected, although lesions may occur (points or small regions) and must be eliminated from the set of landmarks [36]. Traditional retinal-based systems use the whole arterial-venous tree structure as the feature pattern; to improve robustness and speed, the pattern is reduced to a set of landmarks (bifurcations and crossovers of retinal vessels). Bifurcation detectors will also be useful for minimal path approaches that require manual specification of seed points [39]. The detected bifurcations can replace these seeds.

Many methods have been devised for imaging blood vessels, but separating them from acquired data has been a challenge. While significant progress has been made over the years in the segmentation of the vessels themselves, automatic detection of bifurcation points remains a significant difficulty. Several approaches have been proposed, for example based on centerline extraction [38] or on active models (snakes [30] and vessel crawlers [32]). However, the centerline-based methods either do not handle bifurcations (in some cases because the response function tracked decreases at bifurcations) or have difficulties ensuring continuity at vessel junctions. An early tracking-based method is described in [9], and the authors state that “most” of the bifurcations are detected, but do not give any quantitative results. A comprehensive review [22] groups vessel extraction techniques in six families, including artificial intelligence approaches. These appear to be the most promising in terms of sensitivity and accuracy ([51] reports success rate of 97%). However, methods based on artificial intelligence are computationally expensive and require training data, and even the Artificial Intelligence method described in [51] uses a track-and-detect approach, requiring a seed. A more recent review [25] states that bifurcation detection is still one of the most challenging tasks in automated blood vessel segmentation, with only a handful of papers specifically dedicated to bifurcation detection. In some of the papers, the difficulties encountered by vessel

segmentation algorithms are used as clues for the presence of bifurcation. For example, in [3], changes in vessel width estimate is used as a clue for bifurcations.

A technique with high promise for accurate bifurcation detection is based on selection of a local region of interest for more extensive processing. However, algorithms based on analysis in a moving window are computationally expensive, and computationally efficient algorithms require preselection of candidate regions with separate methods. For example, the method proposed in [1] uses a clustering method, where bifurcations are detected by the emergence of several principal directions. In [8], bifurcations are detected by tracking vascular branches and analyzing the binary connected components on the surface of a sphere that moves along them.

1.1 Interest Points in Image Processing

Interest points (or feature points) extraction is an important task in computer vision and image processing. It provides input information for further operations, such as image registration, structure from motion, image retrieval, motion estimation, object recognition, etc. Due to their importance in computer vision, feature points must satisfy a number of requirements:

- it has a clear, preferably mathematically well-founded, definition,
- it has a well-defined position in image space,
- the local image structure around the interest point is rich in terms of local information contents, such that the use of interest points simplify further processing in the vision system,
- it is stable under local and global perturbations in the image domain, including deformations as those arising from perspective transformations (sometimes reduced to affine transformations, scale changes, rotations and/or translations) as well as illumination/brightness variations, such that the interest points can be reliably computed with high degree of reproducibility.
- Optionally, the notion of interest point should include an attribute of scale, to make it possible to compute interest points from real-life images as well as under scale changes.

A thorny problem is a proper, local description of vascular bifurcations in images. To date, such a description (i.e., in terms of differential geometry) does not exist for vascular bifurcations or other similar structures, in part due to large variability of real bifurcations. This is an area of very active research in other fields as well, such as DTMRI (where the structures of interest are neural tracts). The simple, tensor-based representation has significant limitations. In particular this method is unable to represent asymmetric structures. To overcome this, various techniques have been developed, based on more general Orientation Distribution Functions, such as Q-Ball Imaging [43] or tractosemas [4]. In fact, all these methods generate a sampling of a radial function signifying the likelihood of a structure in that direction. These directions are sampled almost uniformly on a sphere, based on tessellation of a regular polyhedron, typically an icosahedron. This is not a compact description, since it places at each point a descriptor consisting of several hundreds, if not thousands of numbers.

Historically, the notion of interest points goes back to the earlier notion of corner detection, where corner features were in early work detected with the primary goal of obtaining robust, stable and well-defined image features for object tracking and recognition of three-dimensional CAD-like objects from two-dimensional images. Structures with a point-like localization are usually classified as either corners or blobs. In practice, however, most corner detectors are sensitive not specifically to corners, but to local image regions which have a high degree of variation in all directions. The classical example in this category is the Moravec corner detector [33]. This corner detector takes a small window, typically square, 3×3 to 7×7 , centered on the pixel. Then, the same window is displaced on the 8 neighboring pixels and the sum of squared intensity differences between the corresponding pixels in the two windows (centered and displaced). This sum of squared intensities is calculated for all 8 displacements, and the *minimum* of these is taken as cornerness measure.

The use of interest points also goes back to the notion of regions of interest, which have been used to signal the presence of objects, often formulated in terms of the output of a blob detection step. While blob detectors have not always been included within the class of interest point operators, there is no rigorous reason for excluding blob descriptors from this class. Both have the same localization properties, and some works use them interchangeably, or use only one term in a generic sense (e.g., corner) meaning any image feature that is useful for of establishing point correspondence between images [21]. For the most common types of blob detectors, each blob descriptor has a well-defined point, which

may correspond to a local maximum, a local maximum in the operator response or a center of gravity of a non-infinitesimal region. In all other respects, the blob descriptors also satisfy the criteria of an interest point defined above. It is true that a number of blob descriptors contain complementary information. But these additional attribute should not disqualify blob descriptors from being included within the class of interest points.

Corners are defined as the intersection of at least two edges, which are themselves defined as the boundary between blocks with different color, intensity, etc. The class of corner detectors sensitive to large variations of intensity in all directions also includes the intensity curve level approach. This approach looks to detect points where the curvature of level curves and the gradient magnitude are simultaneously high. A differential way to detect such points is to compute the rescaled level curve curvature, which also autodetects the scale of the local feature. Larger scale values will be associated with rounded corners of large spatial extent while smaller scale values will be associated with sharp corners with small spatial extent.

Another class of corner detectors processes the image to transform it into one with rich information by extracting at each point a *structure tensor*. Since corners, just like edges, are defined at the boundary between blocks, their mathematical description is based on the gradient. Therefore, the structure tensor is based on the gradient vector (I_x, I_y) , taking into account some smoothing. The single-point structure tensor is a stick tensor (for the stick/ball classification, see Section 3.1). The smoothing (the term was used in the early papers) or averaging (term used in more recent papers) is applied to the tensor itself. It can also be interpreted as a voting process, with every point in the image “voting” for the dominant gradient direction in its neighborhood. Strong gradients give more weight to their neighborhood, while gradients of different directions combine to give a less directional tensor (a ball tensor, or at least a tensor with a strong ball component).

The well-known Harris corner detector [17] is actually defined based on the sum of squared differences between two patches, one over the area and one slightly displaced (they call it “autocorrelation detector”), similar to the Moravec corner detector. However, it improves significantly on it by extending it analytically (the Moravec detector is anisotropic, since it only calculates displacements in the 8 adjacent directions). It uses the Taylor series expansion around the point investigated. Harris and Stephens note that the corner measure must be a function of the eigenvalues alone, on grounds of rotational invariance. Also, Harris states in his original paper that it is attractive use the trace and determinant of

the structure matrix, since this avoids explicit eigenvalue decomposition, and the trace and determinant of a structure tensor are also rotation invariant. We must remember that at the time Harris wrote his paper, calculating the square root needed to compute the eigenvalues was 10, maybe 20 times slower than calculating the product of two numbers.

In [42], Shi and Tomasi follow a similar method, using a small window around the point. They conclude that the symmetric structure tensor must be both above the noise level (meaning that the eigenvalues must be large), and well conditioned (meaning that the eigenvalues can not differ by orders of magnitude). A large and a small eigenvalue correspond to a unidirectional pattern; two large eigenvalues can represent corners or other patterns that can be tracked reliably. They conclude that in practice it is sufficient to use the smaller eigenvalue, as long as it is greater than a predefined threshold.

Using the ball/stick decomposition is interpretation in Section 3.1, the Shi-Tomasi corner detector simply looks for regions with strong ball component, regardless the stick component, while the Harris detector tries to find a balance between the two.

Since corners are the intersection of at least two edges, one might be tempted to look at vascular bifurcations as the intersection of three “lines”, and to apply corner detectors for their detection. But the bifurcation location itself, as intersection of centerlines of participating vessels, is *within* the vessel (where signal intensity is at an extremum – an area of low gradient), while all the corner detectors are designed to work at the boundary between a bright and a dark area (areas with high change rate in signal intensity, with high gradient). They might work on 2D images to detect the high curvature areas occurring in the areas where the vessels join at the boundary between vessels and the surrounding tissues. But this approach needs to group together the corner signals corresponding to the same bifurcation (2 or 3 – depending on bifurcation geometry, since in highly asymmetric bifurcations the two largest vessels are almost on the same line, therefore a corner is not present). We will discuss this aspect more extensively in Section 4.3 when we investigate the performance of various candidates for bifurcation detection. This approach is even more complicated in 3D, where the boundary between the vessels and the surrounding tissues is not a corner, but looks more like a saddle. The isosurface perpendicular to the gradient vector has *two* curvatures, the largest of which is considered for the corneriness measure. Therefore, corner detectors are not directly applicable to bifurcation detection. However, there is another class of localized tensor-based criteria that can be adapted for work with other tensor measures, the blob detectors. Unlike corners, blobs are defined as areas either

brighter or darker than the surroundings, therefore unconnected to other structures in the original image. In a way, these can be seen as an extension of corner detectors, using the Hessian matrix instead of the structure tensor. The classical operators for blob detection are the Laplacian and Determinant of Hessian (DoH), which can be adapted to detect the scale of the features [26, 28]. Another classic blob detector is the Difference of Gaussians, but this can be seen as a discrete approximation for the Laplacian. To these we can add the ball component of the Hessian (mathematically represented by the smallest eigenvalue, similar to the Shi-Tomasi corner detector – more on this later). All of these operators are rotation-invariant and easy to apply in scale-space.

1.2 Our Approach

In 1998, Frangi et al. [13] used the framework of scale-space to separate blood vessels from background based on a simple second-order operator. Essentially, this approach represents the vessels as extrema in the image intensity; therefore, they can be described by the tensor obtained from the second-order derivatives. This tensor describes an ellipsoid, whose long axis is the direction of the vessel. This approach does not detect the bifurcation points; in fact, the vesselness measure defined drops significantly at bifurcation points (although not to 0). The drop is significant when the bifurcation is close to ideal (straight semi-infinite vessel, splitting symmetrically into straight semi-infinite vessels), leading to disconnected vessel segments.

The approach we propose is a simple and direct method, based on the scale space behavior of bifurcations. In the current implementation, it only uses simple image processing techniques, such as background subtraction (the background is approximated with a coarse blurred version of the image) and contrast/brightness adjustment (although this step is necessary mostly for visualization). Since the evolution of an image in the scale-space (at coarser scales) can be obtained from the intensity distribution at any of the finer scales, the background removal step can be eliminated (a constant – or quasi-constant – background does not evolve in scale-space) at the cost of increasing the complexity of the algorithm. As a result of using the scale-space – essentially progressive Gaussian smoothing of the initial image – the method proposed is robust to relatively small amounts of noise. We did not employ any other vessel enhancement techniques; future research will investigate the effect of such preprocessing methods on enhancing the reliability of the algorithm. The

tests of the algorithm were done with 2D images (synthetic as well as clinical), as well as 3D. The detectability tests were done only on 2D images, due to the necessity to obtain a large number of data points for statistically significant results (run time for a single isolated bifurcation, even with a small region of interest around, is about 100 times longer in 3D than in 2D). However, the results are general; since vascular bifurcations are mostly planar, the results can be easily extended for volumetric data. Without loss of generality, we assume bright structures on a dark background; for dark structures on bright background, the algorithm can easily be adapted by reversing either the selection condition or by reversing the contrast in the preprocessing stage.

In this research we used the common scale-space approach – define an operator, then detect its maxima in both space (for localization) and scale (related to the size of the bifurcating vessels). The operator itself is in the same family as other corner and blob detectors, since it is supposed to detect localized structures. There is nothing new in scale-space analysis of images, or in using the Hessian and its eigenvalue analysis, alone or in scale-space. However, this is the first time such an analysis was done on vascular bifurcations. In the research presented here, we made a detailed analysis of various second-order scale-space operators applied to vascular bifurcations and a detailed analysis of the bifurcations themselves. The result is that although conventional operators can detect various localized structures through the influence of their shape on Hessian eigenvalues, there is no way to distinguish between, for example, blobs and bifurcations. Their behavior in scale-space is different. This difference is the main contribution of this research, and is captured in the concept we call *codimension*.

Another major difference is that all the methods reviewed use the traditional track-and-detect approach. They are not only seeded, but also sequential. Thus, at best, only a few independent threads can run at the same time. By contrast, our approach consists only in steps which are massively parallelizable – Fourier transforms and calculating local values in the scale-space. Thus, although our approach might be seen as an oversimplification of the problem, it can be implemented easily on massively multicore hardware architectures such as graphics cards supporting CUDA or OpenCL.

Chapter 2

Introduction to Scale-Space

2.1 The Concept of Scale-Space

The concept of scale-space was first introduced in [23], and its definitions further mathematically refined and formalized in [12]. It comes from the intuitive concepts that each object in an image has limited extent (“outer scale”) and a limited resolution (“inner scale”), which define the relevant range of scales. These limits are set, for example, by the “format” of the image, e.g. by the size of the photographic plate and graininess of the emulsion, by the number and spacing of photosensitive elements in a CCD array, etc. In a number of situations, the inner scale is determined by the structure of radiation itself, e.g., in scintigraphy and PET scans, where the number of quanta is available in limited number (quanta availability limited by dosimetry). In a great many applications the inner and outer scales are set by the subject matter rather than the image format, e.g. a treetop does not exist on the scale of the leaves nor on that of the forest. (You typically define treetops as features in volumes with an outer scale of 10 m and an inner scale of 10 cm say.) The challenge is to understand the image at all the levels of resolution *simultaneously*, and not as a set of derived images at different levels of blurring. This presupposes the existence of *links* between the different levels of resolution. The way to proceed appears to be [23]:

1. Embed the original (also called “primal”) image into a one-parameter family of “derived” images. The parameter measures the resolution, or “inner” scale.
2. Study the family as a family, i.e., define deep structure, the relations between structural features of different derived images.

3. In a later phase, these mathematical structures may be incorporated in more detailed mechanistic models of the visual system composed of homogenous processing layers with a specific across-layers structure (postprocessing and interpretation).

By definition, a front-end vision system is assumed to be completely ignorant of any geometry of the input. This lack of geometry argues for symmetric sampling and preprocessing of its input. In [12], the following set of very reasonable symmetries is proposed:

- *linearity*: allowing superposition of stimuli;
- *spatial shift invariance*, implied by the absence of a preferred location;
- *isotropy*, implied by the absence of a preferred direction;
- *scale invariance*, implied by the absence of a preferred scale.

The requirement for scale invariance comes from the universal law of scale invariance: *physical laws must be independent of the choice of fundamental parameters*, which is equivalent to *a function relating physical observables must be independent of the choice of dimensional units*. This requirement comes from an analysis of the physics of continuous media [7]. There is, however, concern with discretization effects. Strictly speaking, when we are interested in image structure on the sampling device's inner scale, we are facing an apparent undersampling problem, from which there is only one escape: zooming into the scene or resorting to a higher resolution acquisition.

The linearity and the shift invariance require that the rescaled image must be a convolution of the original image $L_0(\mathbf{x})$ by some kernel

$$L(\mathbf{x}, \sigma) = (L_0 \star G(\cdot, \sigma))(\mathbf{x}, \sigma) \quad (2.1)$$

An advantage of this approach is that we can consider this property in the Fourier domain, where it becomes the algebraic relation

$$\mathcal{L}(\omega, \sigma) = (\mathcal{L}_0 \cdot \mathcal{G}(\cdot, \sigma))(\omega, \sigma) \quad (2.2)$$

In this context, **natural coordinates** are dimensionless numbers Ω associated with the spatial frequency ω at a scale σ through

$$\Omega = \sigma\omega \quad (2.3)$$

or, equivalently, in the spatial domain

$$\mathbf{X} = \mathbf{x}/\sigma \tag{2.4}$$

The isotropy requirement is fulfilled by using a rotationally symmetric convolution kernel (i.e., the value of the kernel depends only on the distance between the point and the origin. This applies to both G and \mathcal{G} (that is, in both spatial and the Fourier domain).

Even if not explicitly stated, all scale-space derivations use the *causality hypothesis* [23]: any feature at a coarse level of resolution is required to possess a (not necessarily unique) “cause” at a finer level of resolution, although the reverse need not be true. This asymmetry leads to a rather strong constraint. In effect, this forbids the generation of “spurious resolution”. As a consequence, the transform from fine scale to coarse scale can be regarded as a simplification, so that fine scale details disappear monotonically with increasing scale. If new artificial structures could be created at coarser scales, not corresponding to important regions in the finer scales representations of the signal, then it would be impossible to determine if a feature at a coarse scale corresponds to some coarse-scale feature of the original image or it is just an accidental phenomenon, say amplification of noise, created by the smoothing method. An analysis of this requirement in [23] leads to the *isotropic diffusion equation* (the *heat equation*) as a fundamental starting point for the unique and complete family of scale-space filters:

$$\frac{\partial L}{\partial s} = \frac{1}{2} \Delta L \tag{2.5}$$

where the Laplacian is with respect to the spatial coordinates. The two methods of obtaining the convolution kernel are equivalent and lead to the same result.

There are two obvious limit cases: in the hypothetical zero-scale limit ($\sigma \searrow 0$), the initial image is left unscaled, so $\mathcal{G} \rightarrow 1$. This is the identity as the zero-scale kernel. The opposite case is that of the infinite-scale limit, $\sigma \rightarrow \infty$, which gives a complete averaging of the image, washing out all details. Thus, the values for σ cover \mathbb{R}_0^+ .

The scale invariance requires that performing several rescalings in succession should be consistent with performing a single, effective rescaling. Thus, if two parameters σ_1 and σ_2 are the parameters for two rescalings $\mathcal{G}(\Omega_1)$ and $\mathcal{G}(\Omega_2)$ respectively, then the concatenation of these should be a rescaling $\mathcal{G}(\Omega_3)$ corresponding to an effective parameter $\sigma_3 = \sigma_1 \oplus \sigma_2$. All that is required by the consistency is that the set $(\mathbb{R}_0^+; \oplus)$ constitutes a commutative semigroup isomorphic to the commutative semigroup of image rescalings. Further group

theory considerations and the condition of separability of the kernel (arising from the requirement for a consistent interpretation as spatial rescaling) impose that

$$\sigma_1 \oplus \sigma_2 = \sqrt{\sigma_1^2 + \sigma_2^2} \quad (2.6)$$

so that $s \stackrel{\text{def}}{=} \sigma^2$, not σ itself is the additive parameter. Since the general solution to the group theory constraints is a normalized exponential function $\mathcal{G}(\Omega) = \exp(\alpha\Omega^p)$ with $p = 2$, it is convenient to choose $\alpha = -1/2$, so that the scale coincides with the Gaussian width in the spatial domain. Therefore, it is appropriate to express the scale in terms of widths of the structure being investigated.

Thus, the scale-space family of an image is found to be a series of convolutions of the original image with isotropic Gaussian functions of different widths

$$L(\mathbf{x}, \sigma) = L(\mathbf{x}) \star G(\mathbf{x}; \sigma) \quad (2.7)$$

where the D-dimensional isotropic Gaussian is defined as

$$G(\mathbf{x}; \sigma) = \frac{1}{\sqrt{2\pi\sigma^2}^D} e^{-\frac{\|\mathbf{x}\|^2}{2\sigma^2}} \quad (2.8)$$

We note that the process of deriving the scale-space described in [23] involves the same differential equations as the physical process of diffusion; for this reason the process of conversion to scale-space is sometimes called “diffusion”.

Due to the properties of Gaussians, derivatives of the image in scale-space are simply convolutions of the original image with the corresponding n -th order partial derivatives of the Gaussian kernel,

$$G_{x_1, \dots, x_n} \rightarrow \sigma^{\gamma n} \partial_{x_1, \dots, x_n} G_{x_1, \dots, x_n} \quad (2.9)$$

where the subscripts $x_1, x_2 \dots x_n$ are used to represent partial derivatives with respect to x_j -th spatial coordinate. The parameter γ was introduced by Lindeberg [27] to define a family of normalized derivatives. This is important for proper comparison of scale-space responses for various differential operators, corresponding to various features. For detection of quasi-linear features like blood vessels, this parameter should be set to 1.

2.2 Properties of Scale-Space

To gain insight, it is useful to illustrate the scale-space behavior of several simple structures. The simplest case is that of an image consisting in a one-dimensional Gaussian profile

$$L_0(x) = \exp\left(-\frac{x^2}{2w^2}\right) \quad (2.10)$$

which, in scale-space, becomes

$$L(x, \sigma) = \int_{-\infty}^{\infty} \left(\frac{1}{\sqrt{2\pi\sigma^2}} e^{-\frac{(x-\xi)^2}{2\sigma^2}}\right) e^{-\frac{\xi^2}{2w^2}} d\xi \quad (2.11)$$

This integral evaluates to

$$L(x, \sigma) = \frac{w}{\sqrt{\sigma^2 + w^2}} \exp\left(-\frac{x^2}{2(\sigma^2 + w^2)}\right) \quad (2.12)$$

Consider now the example of two Gaussian ridges, one with width $w = 1$ centered at $x = 5$ and one with width $w = 2$, centered at $x = 15$. Their behavior in scale-space can be easily calculated using Equation 2.12 for each of the ridges and using the superposition principle. However, a mathematical formula tells little about how the intensity profile evolves with scale. Figure 2.1 illustrates this evolution, starting with the initial profile (scale formally set to 0, topmost curve), while the other curves are obtained at scales σ progressively higher, from 1 to 10. At the larger scales, the two structures merged, as the scale of the image became larger than the “inner scale” corresponding to the separation of the two Gaussians, and at the largest scale the remaining profile is approximated by a single wide Gaussian.

A remarkable property is that the same behavior is seen regardless the initial profile. In figure 2.2, the initial profiles were rectangular, with the same as the Gaussians in Figure 2.1. While initially there is some difference in the profiles, this difference is insignificant after only a couple of ridge widths, and decreases quickly with increasing scale. There is a rigorous mathematical proof for this behavior, but there is a simpler, more intuitive (although less rigorous) one: The Gaussian profile is the smoothest profile, with the fewest higher spatial frequencies. Differences from this profile result in higher spatial frequencies, which in the Fourier domain lie farther from the origin. The scale-space transform results in a multiplicative kernel in the Fourier domain; larger scales result in a Fourier kernel with less extent, meaning that higher spatial frequencies are dampened faster than lower spatial frequencies. This is a very important property for this research, since it allows us to

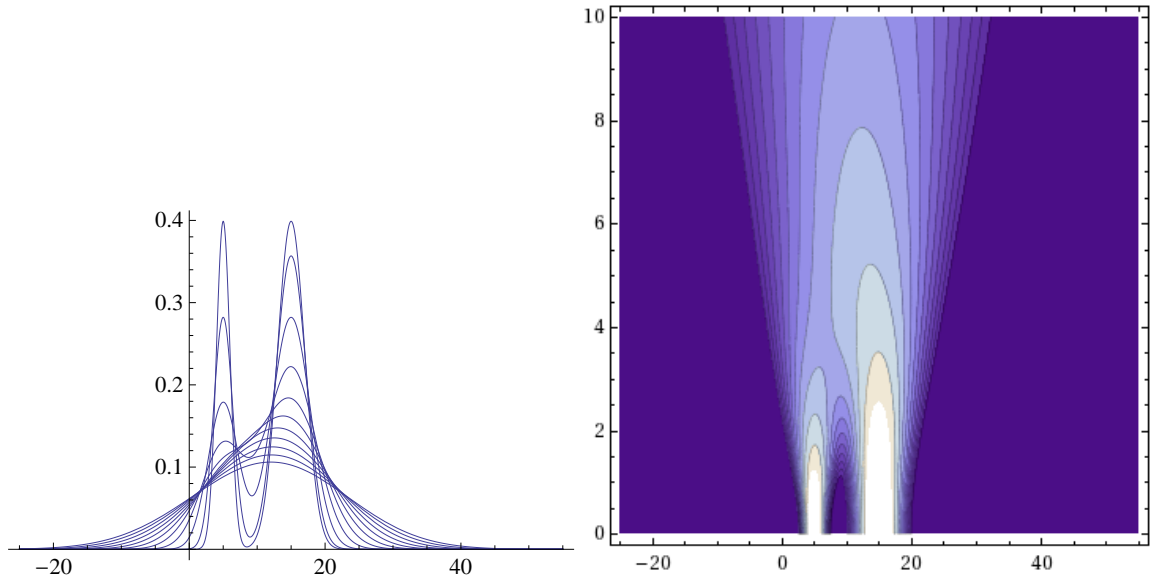


Figure 2.1: Evolution of two Gaussian structures in scale-space: selected profiles and the contour plots of the scale-space

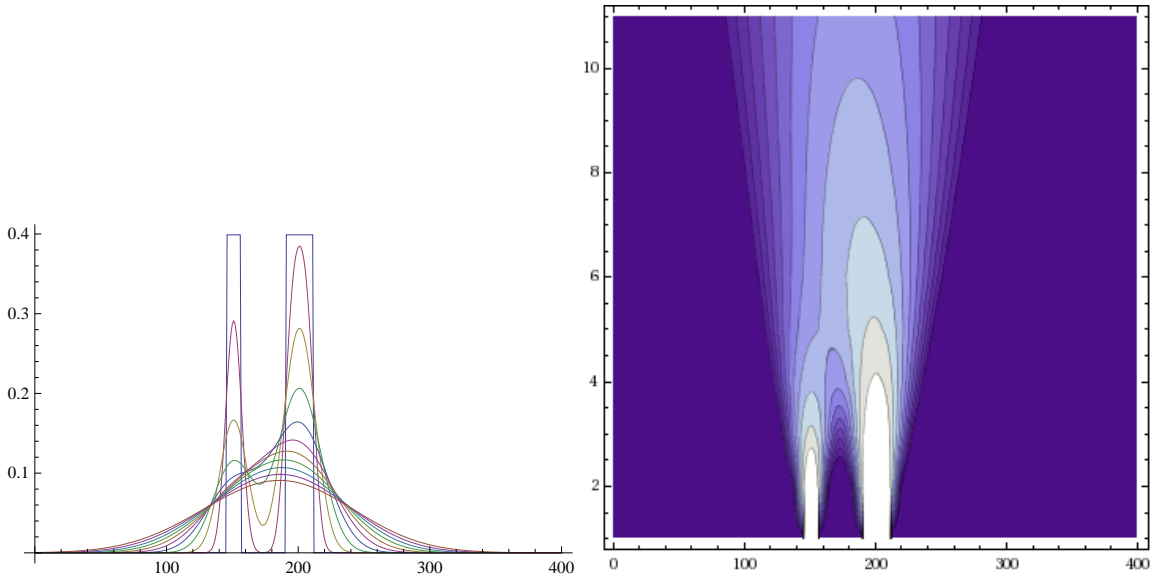


Figure 2.2: Evolution of two rectangular profiles in scale-space: selected profiles and the contour plots in scale-space

treat the blood vessel profile as Gaussian (or any other convenient profile) without worrying about the details of the difference in profile. This is also consistent with the concept that an object exists between an “inner scale” and an “outer scale”. In the context of this research, the structure is a vascular tree, which exists between the “inner scale” (below which the structure of the vessel itself becomes important) and the “outer scale”, where the vessels become so blurred that they merge with each other.

Chapter 3

Vessel and Bifurcation Response in Scale-Space

3.1 Tensorial Description of Vascular Structures

Depending on the imaging technique, blood vessels appear as either bright or dark lines on a gray background. The contrast varies greatly from one imaging technique to another, from one image to another or even within the same image. But the sign of the contrast does not change in the same image. Therefore, without any loss of generality, we will assume that vessels are bright structures on a dark background. The case of dark vessels can be easily converted to this one by a simple change of the criteria or by applying a contrast reversal.

Medical images, like other signals, are analytic signals [6, 15]. This mathematical aspect is extremely important, since it means that the function describing the intensity distribution in the image is locally given by a convergent power series. Such a function is infinitely derivable, and the power series is its Taylor series. Another consequence is that in the case of multiple derivatives along multiple directions, the order of derivation is irrelevant. Thus, the common approach in studying local variations in image intensity changes at the scale s is to express it as a Taylor series around the point studied:

$$L(\mathbf{x}_0 + \delta\mathbf{x}, s) = L(\mathbf{x}_0, s) + \delta\mathbf{x}^T \nabla L(\mathbf{x}_0, s) + \delta\mathbf{x}^T \mathcal{H}(L(\mathbf{x}_0, s)) \delta\mathbf{x} + \dots \quad (3.1)$$

The series is truncated at the lowest nonzero variation, since the sum of all other terms is usually much smaller. Edge detectors (and in consequence corner detectors) look at the boundaries between bright and dark areas, thus are areas of maximum gradient. Blood

vessels, however, typically have maximum intensity on their centerlines; thus, at the point of interest, the gradient $\nabla L(\mathbf{x}_0, s)$ is zero. For this reason, traditional corner detection algorithms, such as Harris or Shi-Tomasi are useless.

The first nonzero variation is the second order variation, described by the Hessian matrix $\mathcal{H}(L(\mathbf{x}_0, s))$. For simplicity, the operator characteristic of the Hessian will be ignored, so \mathcal{H} will be used to denote the Hessian matrix at all points, with or without explicit dependence on coordinates and scale. Due to the analyticity of the signal, the Hessian matrix is a second-order symmetric tensor, with the geometric interpretation as an ellipsoid oriented along the vessel. The information encoded in the Hessian matrix/tensor can be made explicit by using the eigenvalue/eigenvector decomposition. This description can be further enhanced with a different decomposition, into more intuitive components. Formally, this description comes from the property of tensors to be represented by their associated eigensystem, with three eigenvectors \hat{e}_1 , \hat{e}_2 , and \hat{e}_3 , and the three corresponding eigenvalues considered here as absolute values for the purpose of geometrical interpretation, $\lambda_3 \geq \lambda_2 \geq \lambda_1 \geq 0$. In 2D, a symmetric tensor T can be written as

$$T = \begin{pmatrix} a_{11} & a_{12} \\ a_{12} & a_{22} \end{pmatrix} = \begin{pmatrix} \hat{e}_1 & \hat{e}_2 \end{pmatrix} \begin{pmatrix} \lambda_1 & 0 \\ 0 & \lambda_2 \end{pmatrix} \begin{pmatrix} \hat{e}_1^T \\ \hat{e}_2^T \end{pmatrix} \quad (3.2)$$

This decomposition can be rearranged as

$$T = (\lambda_2 - \lambda_1)\hat{e}_2\hat{e}_2^T + \lambda_1(\hat{e}_1\hat{e}_1^T + \hat{e}_2\hat{e}_2^T) \quad (3.3)$$

where $\hat{e}_2\hat{e}_2^T$ is the unit stick tensor and $\hat{e}_1\hat{e}_1^T + \hat{e}_2\hat{e}_2^T$ is the unit ball tensor. The quantity $s = \lambda_2 - \lambda_1$ is called *stickness*, and $b = \lambda_1$ is called *ballness*.

In 3D, we have a similar decomposition:

$$T = \begin{pmatrix} a_{11} & a_{12} & a_{13} \\ a_{12} & a_{22} & a_{23} \\ a_{13} & a_{23} & a_{33} \end{pmatrix} = \begin{pmatrix} \hat{e}_1 & \hat{e}_2 & \hat{e}_3 \end{pmatrix} \begin{pmatrix} \lambda_1 & 0 & 0 \\ 0 & \lambda_2 & 0 \\ 0 & 0 & \lambda_3 \end{pmatrix} \begin{pmatrix} \hat{e}_1^T \\ \hat{e}_2^T \\ \hat{e}_3^T \end{pmatrix} \quad (3.4)$$

This decomposition can be rearranged as

$$T = (\lambda_3 - \lambda_2)\hat{e}_3\hat{e}_3^T + (\lambda_2 - \lambda_1)(\hat{e}_2\hat{e}_2^T + \hat{e}_3\hat{e}_3^T) + \lambda_1(\hat{e}_1\hat{e}_1^T + \hat{e}_2\hat{e}_2^T + \hat{e}_3\hat{e}_3^T) \quad (3.5)$$

where $\hat{e}_3\hat{e}_3^T$ is the unit stick tensor, $\hat{e}_2\hat{e}_2^T + \hat{e}_3\hat{e}_3^T$ is the unit plate tensor and $\hat{e}_1\hat{e}_1^T + \hat{e}_2\hat{e}_2^T + \hat{e}_3\hat{e}_3^T$ is the unit ball tensor. The quantity $s = \lambda_3 - \lambda_2$ is called *stickness*, $p = \lambda_2 - \lambda_1$ is called *plateness*, and $b = \lambda_1$ is called *ballness*.

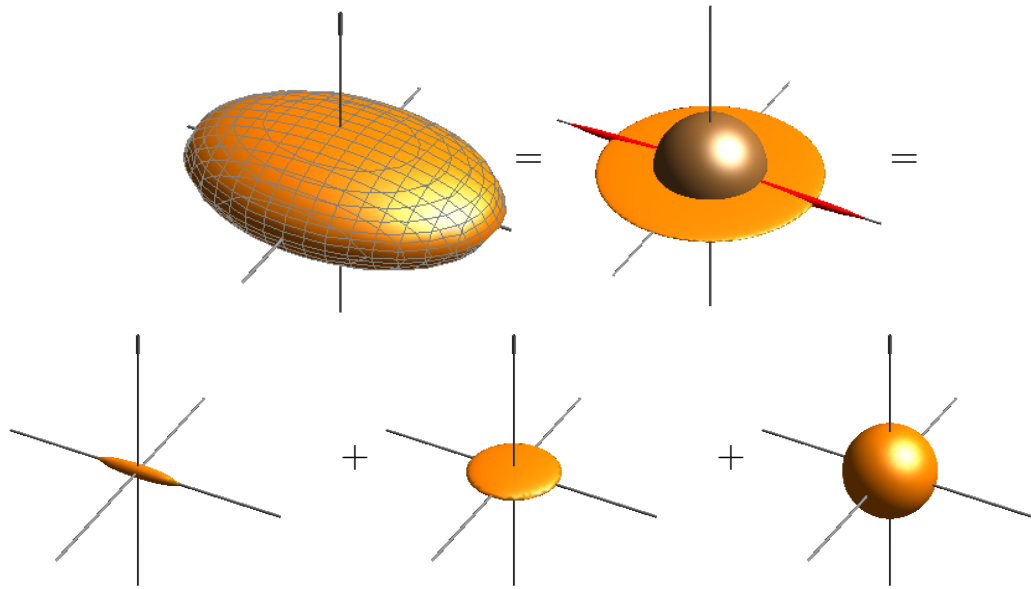


Figure 3.1: Decomposing a symmetric tensor (top) into its components: ball, plate, and stick (bottom)

This decomposition is useful in interpreting image structures, allowing easy classification based on the dominant component. We note that the large eigenvalues of the Hessian are in the direction of large variation, so for an image structure their corresponding eigenvectors will point in the direction of the smaller size. Thus, the dominant component of the Hessian tensor (ball/plate/stick) will correspond to the manifold *orthogonal* to the structure. A ridge-like structure like a blood vessel is elongated in one direction, while being of very limited extent (and of comparable size) in the other two directions. Thus, the Hessian tensor on its centerline will have a very low eigenvalue along the axis of the vessel, while having comparably large eigenvalues in the perpendicular direction. In terms of the above-presented decomposition, the Hessian has a very large plate component, oriented perpendicular to the direction of the vessel. A small, localized structure, of small extent in all directions, will have all eigenvalues of similar magnitude (and of the same sign), so it will have a rather large ball component with comparably small stick and plate components. Such a classification is not unlike the discussion on the Harris corner detector [17] summarized on page 52, except for the use of the Hessian matrix instead of the gradient-based structure tensor. This is the basis for the Frangi vessel enhancement filter, which looks for elongated structures by

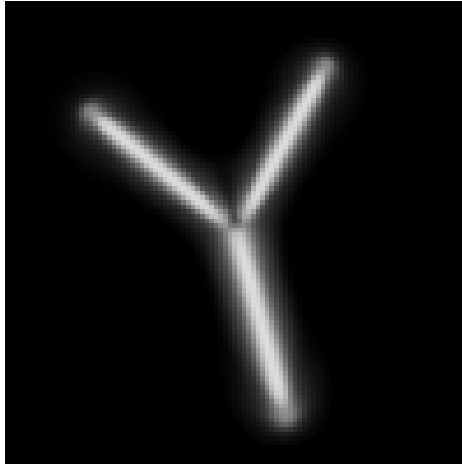


Figure 3.2: Frangi's vesselness applied to a synthetic bifurcation. The measure drops close to 0 at the actual location of the bifurcation.

defining a measure called *vesselness*, using Gaussian penalties for departures from the desired shape; for details, see [13] and a detailed presentation in Appendix C. The disadvantage of the method is that it does not handle bifurcations. In the worst case scenario, that of a symmetric bifurcation, the vesselness measure is close to 0. Such an example is presented in Figure 3.2, where the parent and the daughter vessels appear not to touch each other after applying the vesselness filter.

3.2 Vessel Response in Scale Space

The basis of the approach we propose is the scale-space response of a straight semi-infinite ideal vessel. The geometry is illustrated in Figure 3.3(a) for a 2D image and in Figure 3.3(b) for 3D. This figure describes what we call “ideal semi-infinite vessel”. The vessel has a finite transverse extension (in the y coordinate) of radius w ; in this direction, the profile can be rectangular or Gaussian, two profiles for which the results can be obtained in closed form. The vessel segment starts at x_0 and continues to infinity, with uniform profile. This idealization allows fully analytical calculations to be made using separation of variables. At first sight, it may appear that the analytical calculations are valid only for a particular orientation of the vessel. But we have to remind that in mathematics it is a common practice that when computations are difficult in a general coordinate system, a coordinate transform

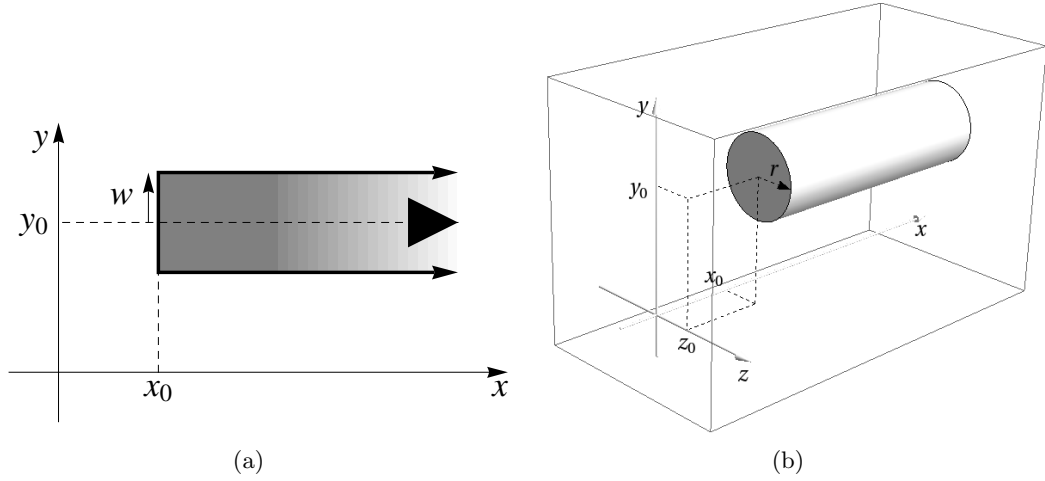


Figure 3.3: The geometry for calculating scale-space response of a semi-infinite vessel with a radius w , at distance y_0 from the axis of the vessel and offset x_0 from its end, in 2D (a) and 3D (b)

is applied so the calculations are easier to perform (e.g., variables separate). Coordinate systems are nothing magical — they are just a tool, and to perform a task, one must pick the right tool. The coordinates used in Figure 3.3 are the natural choice for calculating the scale-space response of a vessel: they express the position of any point in space in terms of distance from the point to the axis of the vessel and distance between the point and the end of the vessel, measured along the axis. Even in the 3D geometry (Figure 3.3(b)), we can set, without loss of generality, $z_0 = 0$, since it is equivalent to the more general case by applying a rotation about the x axis. As we will see later, the only relevant quantity (beside x_0) is $y_0^2 + z_0^2$, the distance between the point where we calculate the response (the origin of the coordinate system) and the axis of the vessel.

For a vessel with a Gaussian profile, the limits in y , as shown in Figure 3.3(a), simply represent the standard deviation of the profile. Such a vessel with Gaussian profile has the scale-space response

$$L(x_0, y_0; \sigma) = \int_{-\infty}^{\infty} \left(\int_{x_0}^{\infty} \frac{1}{2\pi\sigma^2} e^{-\frac{x^2+y^2}{2\sigma^2}} e^{-\frac{(y-y_0)^2}{2w^2}} dx \right) dy \quad (3.6)$$

where x_0 and y_0 are the coordinates of the point where we calculate the scale-space response with respect to the semi-vessel (or, equivalently, the coordinates of the semi-vessel with

respect to the point where we calculate the scale-space response). This integral evaluates to

$$L(x_0, y_0; \sigma) = \frac{w}{2\sqrt{\sigma^2 + w^2}} e^{-\frac{y_0^2}{2(\sigma^2 + w^2)}} \left[1 - \text{Erf} \left(\frac{x_0}{\sigma\sqrt{2}} \right) \right] \quad (3.7)$$

In a section at the end of the vessel and perpendicular to its axis ($x_0 = 0$), this becomes

$$L(0, y_0; \sigma) = \frac{w}{2\sqrt{\sigma^2 + w^2}} e^{-\frac{y_0^2}{2(\sigma^2 + w^2)}} \quad (3.8)$$

while for a full vessel ($x_0 \rightarrow \infty$), the scale-space response is

$$L(0, y_0; \sigma) = \frac{w}{\sqrt{\sigma^2 + w^2}} e^{-\frac{y_0^2}{2(\sigma^2 + w^2)}} \quad (3.9)$$

If the vessel profile is rectangular, the corresponding intensity is 1 inside the vessel and 0 outside; the vessel profile outlined in Figure 3.3(a) becomes the integration limits for the scale-space kernel:

$$L(x_0, y_0; \sigma) = \int_{y_0-w}^{y_0+w} \left(\int_{x_0}^{\infty} \frac{1}{2\pi\sigma^2} e^{-\frac{x^2+y^2}{2\sigma^2}} dx \right) dy \quad (3.10)$$

This integral evaluates to

$$L(x_0, y_0; \sigma) = \frac{1}{4} \left[\text{Erf} \left(\frac{y_0 + w}{\sqrt{2}\sigma} \right) - \text{Erf} \left(\frac{y_0 - w}{\sqrt{2}\sigma} \right) \right] \left[1 - \text{Erf} \left(\frac{x_0}{\sqrt{2}\sigma} \right) \right] \quad (3.11)$$

In a section at the end of the vessel and perpendicular to its axis ($x_0 = 0$), this becomes

$$L(0, y_0; \sigma) = \frac{1}{4} \left[\text{Erf} \left(\frac{y_0 + w}{\sqrt{2}\sigma} \right) - \text{Erf} \left(\frac{y_0 - w}{\sqrt{2}\sigma} \right) \right] \quad (3.12)$$

At first sight, the response of the rectangular profile does not look anything like the response of the Gaussian profile. However, for scale σ much larger than the width w of the vessel, we can expand Equation 3.12 in series around y_0 :

$$L(0, y_0; \sigma) = \frac{w}{\sqrt{2\pi}\sigma} e^{-\frac{y_0^2}{2\sigma^2}} + \frac{w^3}{\sigma^3} \frac{y_0^2 - \sigma^2}{6\sqrt{2\pi}\sigma^2} e^{-\frac{y_0^2}{2\sigma^2}} + \dots \quad (3.13)$$

We note that the first term in the expansion is the same as the scale-space response of a Gaussian vessel, as given in Eq. 3.8, with the same w/σ decay of the amplitude. The amplitude is different, since the section through a rectangular profile is different from the section through a Gaussian profile with the same characteristic width. The next term is essentially proportional to the derivative of the Gaussian profile, but with its amplitude

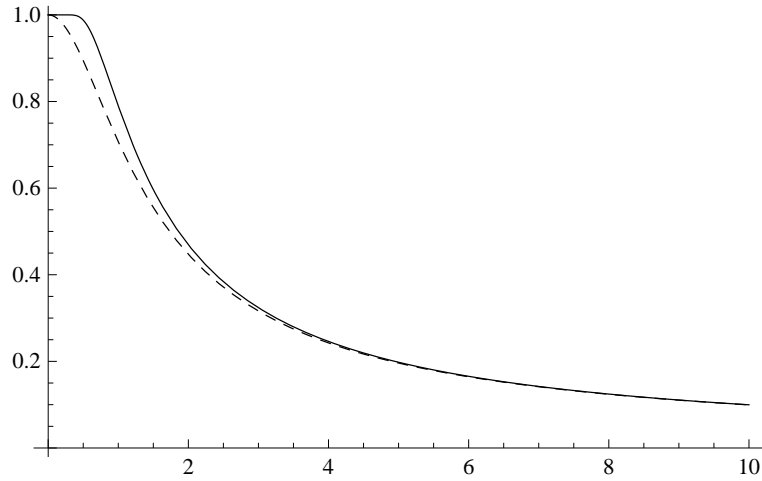


Figure 3.4: Decay of intensity at the center of vessel with scale (on horizontal scale), for rectangular profile (continuous line) and Gaussian profile (dashed line) with width $w = 1$.

decaying with scale as $(w/\sigma)^3$. The other terms are proportional to higher order derivatives of the base Gaussian profile, and with amplitude decaying even faster with scale. This is a mathematical proof that the rectangular profile and the Gaussian profile have the same behavior in scale space, for large enough scales. The decay of the amplitude on the axis of a vessel is illustrated in Figure 3.4 for a Gaussian profile and for a rectangular profile with the same initial amplitude and the same “effective width”, i.e., generating the same flow. As showed mathematically above, we can see that at scales σ above about two vessel radii w , the two decay curves practically coincide. Since the scale is larger than the “inner scale”, the influence of the internal structure of the vessel practically vanishes. Vessels with a different intensity profile will have an intensity decay governed by the same law, with a profile-dependent effective width. The same behavior would be seen for any initial vessel profile. On the axis of the vessel, $y_0 = 0$ and the dominant term of the intensity at large scale ($s \gg w$) is $\frac{w}{\sqrt{w^2 + \sigma^2}}$, with w being the effective width of the vessel.

For a semi-infinite vessel in 3D, as illustrated in Figure 3.3(b), if the transverse profile is Gaussian, the scale-space response is

$$L(x_0, y_0; \sigma) = \int_{-\infty}^{\infty} \left(\int_{-\infty}^{\infty} \left(\int_{x_0}^{\infty} e^{-\frac{(y-y_0)^2 + (z-z_0)^2}{2w^2}} \left(\frac{1}{(2\pi\sigma^2)^{\frac{3}{2}}} e^{-\frac{x^2 + y^2 + z^2}{2\sigma^2}} \right) dx \right) dy \right) dz \quad (3.14)$$

We note that we can combine the two Gaussians of the integrand, then factorize it as a product of three Gaussian functions, each in one of the coordinates. Thus, the variables separate and the 3D integral becomes a product of three one-dimensional integrals

$$\begin{aligned}
L(x_0, y_0; \sigma) &= \int_{x_0}^{\infty} \frac{1}{(2\pi\sigma^2)^{\frac{1}{2}}} e^{-\frac{x^2}{2\sigma^2}} dx \\
&\quad \times \int_{-\infty}^{\infty} \frac{1}{(2\pi\sigma^2)^{\frac{1}{2}}} e^{-\frac{y^2}{2\sigma^2} - \frac{(y-y_0)^2}{2w^2}} dy \\
&\quad \times \int_{-\infty}^{\infty} \frac{1}{(2\pi\sigma^2)^{\frac{1}{2}}} e^{-\frac{(z-z_0)^2}{2w^2} - \frac{z^2}{2\sigma^2}} dz \quad (3.15)
\end{aligned}$$

Each of these integrals can be evaluated separately

$$\begin{aligned}
L(x_0, y_0; \sigma) &= \frac{1}{2} \left[1 - \text{Erf} \left(\frac{x_0}{\sigma\sqrt{2}} \right) \right] \\
&\quad \times \left(\frac{w}{\sqrt{\sigma^2 + w^2}} \right) e^{-\frac{y_0^2}{2(\sigma^2 + w^2)}} \\
&\quad \times \left(\frac{w}{\sqrt{\sigma^2 + w^2}} \right) e^{-\frac{z_0^2}{2(\sigma^2 + w^2)}} \quad (3.16)
\end{aligned}$$

or

$$L(x_0, y_0; \sigma) = \frac{1}{2} \left(\frac{w}{\sqrt{\sigma^2 + w^2}} \right)^2 e^{-\frac{y_0^2 + z_0^2}{2(\sigma^2 + w^2)}} \left[1 - \text{Erf} \left(\frac{x_0}{\sigma\sqrt{2}} \right) \right] \quad (3.17)$$

These results are relevant for geometries with arbitrary number of dimensions, for structures localized (i.e. of finite extent) in at least some of them. The structures of interest for us are “generalized vessels”, with the same finite extent in some of the directions and infinite extent in the others. The local profile of any such structure naturally separates in variables along the eigenvectors of the Hessian. Along with the separation of variables of the scale space kernel in any coordinate system (a consequence of the isotropy principle), this leads to a scale-space response similar to that in Eq. 2.12 for each of these directions, as we can see in Eq. 3.16 for the variables y_0 and z_0 (we’ll call them “transverse coordinates”). We note that the 2D vessel (Eq. 3.7) has one such factor for its only transverse direction y_0 , while the 3D vessel has two such factors for each of its two transverse directions. In geometries with higher number of dimensions, the calculations are similar, resulting in a $\frac{w}{\sqrt{w^2 + \sigma^2}}$ term on the centerline for each transverse dimension. Thus, focusing on the circular section characteristic to blood vessels (same width w in the transverse directions) and the

scale-space intensity on the centerline ($y_0 = 0, z_0 = 0, x_0 = -\infty$) of a vessel with radius w , the dominant term of the decay rate is

$$\Lambda(w, \sigma) = A \left(\frac{w}{\sqrt{w^2 + \sigma^2}} \right)^\delta \quad (3.18)$$

where $\Lambda(w, \sigma)$ is the intensity on the centerline of the vessel, as a function of the vessel width w and the scale s . The constant A can be understood as the amplitude of the Gaussian component of the initial vascular profile, but its expression is irrelevant. In Equation 3.18, $\delta = 1$ for a vessel in a 2D image (a line), as well as a sheet in 3D, as these can diffuse in only one transverse dimension; $\delta = 2$ for a “dot” in 2D (a blob), as well as a vessel in 3D, and $\delta = 3$ for a blob in 3D. We call this δ , the number of transverse dimensions, *codimension*, and it means the number of dimensions in which diffusion can occur, excluding the diffusion internal to the diffused structure itself. For example, considering an ideal vessel, represented by an infinite cylinder, we can see that diffusion along the axis of the cylinder has no effect on intensity distribution, since the signal lost by diffusion from one point on the axis of the cylinder is compensated by the signal received by diffusion from all the other points on the cylinder axis. The only loss of signal is by diffusion in directions perpendicular to the axis of the cylinder.

We note that only the coordinate along the axis of the cylinder is relevant for the position of a point in a vessel (remember that we are in scale-space, at a scale where the internal profile of the vessel is irrelevant). For this reason, a vessel can be considered a one-dimensional structure. The signal can diffuse only in directions perpendicular to the axis of the cylinder, which span the subspace orthogonal to the cylinder axis. A similar argument can be made for structures with other dimensionalities, e.g. plate-like structures, which have two dimensions, or to more complex structures in spaces with higher number of dimensions. The subspace orthogonal to the structure of interest has a number of dimensions equal to the number of dimensions of the space minus the number of dimensions of the structure if interest. This difference is encoded by the parameter δ and the reason we call it codimension.

In equation 3.18 there are three parameters which determine the intensity decay with scale (initial intensity of the vessel, initial width, and codimension). These initial parameters as used in Equation 3.18 can not be determined from the initial image since they are effective parameters, and depend not only on initial intensity and width as measured in the initial image, but also on vessel profile.

Equation 3.18 can be used to obtain the codimension from the change in intensity with scale and thus to identify the local structure. We assume that the structure is at a scale where only the fundamental Gaussian component is present (the other components having decayed and thus having no influence), and perform a local fit of the intensity change with scale with a power decay as given by Equation 3.18 to evaluate the cosimension. If the computed codimension is an integer number (or "close enough"), then the structure is close to an ideal structure. In practice, for this to happen, it is sufficient to be at a scale slightly larger than the scale of the structure (the scale of maximum response) for this to happen. The words "slightly larger" and "close enough" are rather vague, but are explored in sufficient detail later in this chapter. Since there are three parameters, three values of intensity in scale-space are sufficient to calculate them. Explicit computation from intensity at three scales is cumbersome, but there is a shortcut. We can use discrete scale-space values to calculate the first and second derivatives of intensity with respect to scale σ (or the scale parameter s), then use these values to calculate the codimension. This method has the advantage that the derivatives can, in principle, be computed only from the intensity distribution at the current scale, using the diffusion equation 2.5. We note that it is easier to use for this purpose the scale parameter s rather than the scale σ itself, since

1. The scale parameter is the natural evolution coordinate in the heat equation 2.5
2. The expressions of the derivatives are simpler, since there is no need to add the factors from the derivative of σ^2

The first derivative of a Gaussian structure with respect to the scale parameter is

$$\frac{\partial \Lambda}{\partial s} = -\frac{\delta}{2} A w^\delta (w^2 + s)^{-\frac{\delta}{2}-1} \quad (3.19)$$

while the second derivative is

$$\frac{\partial^2 \Lambda}{\partial s^2} = -\frac{\delta(\delta+2)}{4} A w^\delta (w^2 + s)^{-\frac{\delta}{2}-2} \quad (3.20)$$

We can eliminate the amplitude by dividing these derivatives with the scale-space intensity

$$\Lambda_1 = \frac{1}{\Lambda} \frac{\partial \Lambda}{\partial s} = -\frac{\delta}{2(w^2 + s)} \quad (3.21)$$

$$\Lambda_2 = \frac{1}{\Lambda} \frac{\partial^2 \Lambda}{\partial s^2} = \frac{\delta(\delta+2)}{4(w^2 + s)^2} \quad (3.22)$$

Now it is straightforward to eliminate $w^2 + s$ from these equations to obtain

$$\Lambda_2 = \frac{\delta + 2}{\delta} \Lambda_1^2 \quad (3.23)$$

then solve it for δ to obtain

$$\delta = \frac{2\Lambda_1^2}{\Lambda_2 - \Lambda_1^2} \quad (3.24)$$

A drawback of this method of calculating the codimension is that it depends on the lack of a background for the blood vessels. If a background is present, Equation 3.18 has *four* parameters, and this method can not be used. If a background is present (there is an additional constant or very slowly varying term in equation 3.18), there are four parameters determining the value of the intensity in scale-space and three points are no longer sufficient for calculating the codimension. Therefore, the background must be extracted in a preprocessing step.

At sufficiently large scales (that is, $\sigma = \sqrt{s} \gg w$), vessel width w can be ignored in the denominator of Equation 3.18, and the intensity decay becomes

$$\Lambda = Aw^\delta s^{-\delta/2} \quad (3.25)$$

which, after similar calculations, gives

$$\delta = -2 \left(\frac{s\Lambda''}{\Lambda'} + 1 \right) \quad (3.26)$$

where the primes are derivatives of intensity with respect to scale. Although this form does not depend on background elimination or on higher-order derivatives, it gives reasonably accurate results for a single vessel or bifurcation only at large scales, where we usually get interference from nearby structures.

If instead of scale-space intensity we use the scale-space evolution of some spatial derivative, the background is naturally eliminated. Since we are interested in vessels, the first spatial derivatives are 0 or very small, and the local variation is given by the second derivatives, the Hessian matrix (see Eq. 3.1). A rotation-invariant description based on the second derivatives is the Laplacian, which is the trace of the Hessian matrix. In the coordinate system of the eigenvectors of the Hessian, the Laplacian is simply the sum of the eigenvalues of the Hessian.

As noted before, in the coordinate system of the Hessian eigenvectors, the local intensity function can be written using separation of variables

$$L(\mathbf{x}, s) = L_1(x_1, s) \cdot L_1(x_2, s) \cdot \dots \quad (3.27)$$

so that the derivatives of the function with respect to *one* of the variables are simply the derivatives of the corresponding function with respect to its variable, multiplied by all the other functions. For example, the derivative of order n with respect to x_1 is

$$\frac{\partial^n}{\partial x_1^n} L = \frac{\partial^n}{\partial x_1^n} L_1 \cdot L_1(x_2, s) \cdots = L \frac{1}{L_1} \frac{d^n}{dx_1^n} L_1 \quad (3.28)$$

so the Laplacian for a point on a localized structure can be written as

$$\Delta L = L \frac{1}{L_1} \frac{d^2}{dx_1^2} L_1 + L \frac{1}{L_2} \frac{d^2}{dx_1^2} L_2 + \cdots = L \sum_{i=1}^{\delta} \frac{1}{L_i} \frac{d^2}{dx_1^2} L_i \quad (3.29)$$

where the sum extends over all non-constant dimensions. For example, for a blood vessel in a 3D, there are two terms from the two transverse coordinates, while the contribution from the coordinate along the centerline is negligible. For a structure with a Gaussian profile in one of the transverse directions, the scale-space contribution of that (separable) dimension is given by Equation 3.9, and its contribution to the Laplacian is

$$\frac{1}{L_1} \frac{d^2}{dx^2} L_1 = \frac{x^2 - (w^2 + s)}{(w^2 + s)^2} \quad (3.30)$$

while the total Laplacian becomes

$$\Delta L = L \sum_{i=1}^{\delta} \frac{1}{L_i} \frac{d^2}{dx_1^2} L_i = L \frac{\sum_{i=1}^{\delta} x_i - \delta(w^2 + s)}{(w^2 + s)^2} \quad (3.31)$$

Similar to the previous discussion, we look at the behavior on the centerline, therefore $\sum_{i=1}^{\delta} x_i = 0$ and the Laplacian takes the simple form (reusing the symbol Λ for the quantity to be tracked in scale-space, here the Laplacian)

$$\Lambda = \Delta L = -L \frac{\delta}{w^2 + s} = -A \delta w^{\delta} (w^2 + s)^{-\frac{\delta}{2}-1} \quad (3.32)$$

The expression above must be multiplied with a factor s to obtain the correct scale-normalized Laplacian. However, it is much easier to obtain the codimension from the *non-normalized* scale-space Laplacian. Similar to the discussion above, we take the derivatives of the Laplacian with respect to the scale parameter. The first derivative is given by

$$\Lambda_1 = \frac{1}{\Lambda} \frac{d\Lambda}{ds} = -\frac{2 + \delta}{2(w^2 + s)} \quad (3.33)$$

while the second derivative is given by

$$\begin{aligned} \Lambda_2 &= \frac{1}{\Lambda} \frac{d^2\Lambda}{ds^2} = \frac{(2 + \delta)(4 + \delta)}{4(w^2 + s)^2} \\ &= \Lambda_1^2 \frac{4 + \delta}{2 + \delta} \end{aligned} \quad (3.34)$$

Λ	parameter	Λ_1	Λ_2	δ
Intensity	s	$\frac{1}{\Lambda} \frac{d\Lambda}{ds}$	$\frac{1}{\Lambda} \frac{d^2\Lambda}{ds^2}$	$\frac{2\Lambda_1^2}{\Lambda_2 - \Lambda_1^2}$
	σ	$\frac{1}{\Lambda} \frac{d\Lambda}{d\sigma}$	$\frac{1}{\Lambda} \frac{d^2\Lambda}{d\sigma^2}$	$\frac{2\sigma\Lambda_1^2}{(\Lambda_2 - \Lambda_1^2)\sigma - \Lambda_1}$
Laplacian	s	$\frac{1}{\Lambda} \frac{d\Lambda}{ds}$	$\frac{1}{\Lambda} \frac{d^2\Lambda}{ds^2}$	$\frac{2\Lambda_1^2}{\Lambda_2 - \Lambda_1^2} - 2$
	σ	$\frac{1}{\Lambda} \frac{d\Lambda}{d\sigma}$	$\frac{1}{\Lambda} \frac{d^2\Lambda}{d\sigma^2}$	$\frac{2\sigma\Lambda_1^2}{(\Lambda_2 - \Lambda_1^2)\sigma - \Lambda_1} - 2$
Intensity (asymptotic)	s	$\frac{d\Lambda}{ds}$	$\frac{d^2\Lambda}{ds^2}$	$-\frac{2s\Lambda_2}{\Lambda_1} - 2$
	σ	$\frac{d\Lambda}{d\sigma}$	$\frac{d^2\Lambda}{d\sigma^2}$	$\frac{\sigma\Lambda_2}{\Lambda_1} - 1$

Table 3.1: Summary of formulae for calculating codimension using scale-space variation in intensity and Laplacian, measured at the center of the structure

Here we eliminated $w^2 + s$ from the expression of the second derivative using the first derivative. It is now trivial to obtain the codimension using the change in Laplacian as

$$\delta = \frac{2\Lambda_1^2}{\Lambda_2 - \Lambda_1^2} - 2 \quad (3.35)$$

The equations for the scale-space evolution of intensity 3.18 and of the Laplacian 3.32 are very similar; in fact, the Laplacian has the same evolution as the intensity but with a codimension higher by 2. This difference is more obvious if we compare the final expressions for the codimension, Equations 3.24 and 3.35. Similar (but slightly more complicated) calculations can be made using the scale as variable instead of the scale parameter. All the resulting formulas are summarized in Table 3.1

Figure 3.5 shows plots of codimension calculated at different scales, for three representative transversal profiles: Gaussian ($\exp(-x^2/(2w^2))$), parabolic (1 in center, decreasing to 0 at $\pm w$) and rectangular (1 between $\pm w$), in the center of three types of 2D structures: infinite straight vessel, circular blob, and an elongated blob, with axis ratio of 5:1. Figure 3.6 has the same plots, but for a 3D geometry. The Gaussian infinite vessel and the Gaussian circular blob are the standards against which we rate all other estimates. The intensity-based estimate is virtually at the ideal value for the Gaussian vessel and circular blob, while the parabolic and rectangular profiles need some “adjustment period” to shed higher spatial

harmonics and to reach a stable codimension. Obviously, it takes longer for the rectangular profile to stabilize. It may be surprising that the parabolic profile takes almost as long, but we have to remember that it has a sharp cutoff at $\pm w$, and this generates significant noise in higher spatial harmonics. In all cases, the intensity gives a better estimate for codimension. This can be attributed to the following reasons:

1. Deviations from the model are expected due to discretization errors, both in spatial direction (controlling subsequent evolution) and scale direction (discretization used to obtain the scale derivatives for calculating codimension). The Laplacian has a sharper drop with scale, since it has a higher “effective codimension”.
2. The Laplacian, as a filter, is more sensitive to higher spatial frequencies, thus its response is skewed more towards a sharper decay manifested as a codimension slightly higher than the theoretical value.

The most interesting (but expected) behavior is observed for a moderately elongated structure, with axis ratio 5:1. For the Gaussian profile, the evolution of the estimated codimension clearly shows two regions and the transition between them. Initially, the structure has the codimension of a vessel; the scale is small enough so that there is very little influence from the endings of the vessel. This is followed by a region of transition towards the “blob state”, at scales comparable to the length of the vessel. The evolution of estimated codimension for the parabolic and rectangular profiles, in both 2D and 3D, shows the three characteristic regions of the scale-space: small scales, where the internal structure plays a very important role and codimension can not be reliably obtained; a “sweet spot” around scales comparable with the vessel half-width w (here, about 5–7), followed by the outer scales, where everything is averaged out and looks like a blob. It is interesting that at a scale approximately equal to vessel half-width both intensity and Laplacian estimates of codimension give reliable estimates for the codimension, although the Laplacian-based estimate changes rather quickly outside this scale, due to its sensitivity to higher frequencies. The Laplacian-based estimate works better in 3D images, due to the higher codimension which allows high frequencies to dissipate faster.

There are advantages and disadvantages to both methods of estimating codimension. The intensity-based estimate is more reliable and less sensitive to noise when the image has no background (either naturally or as result of a background extraction algorithm).

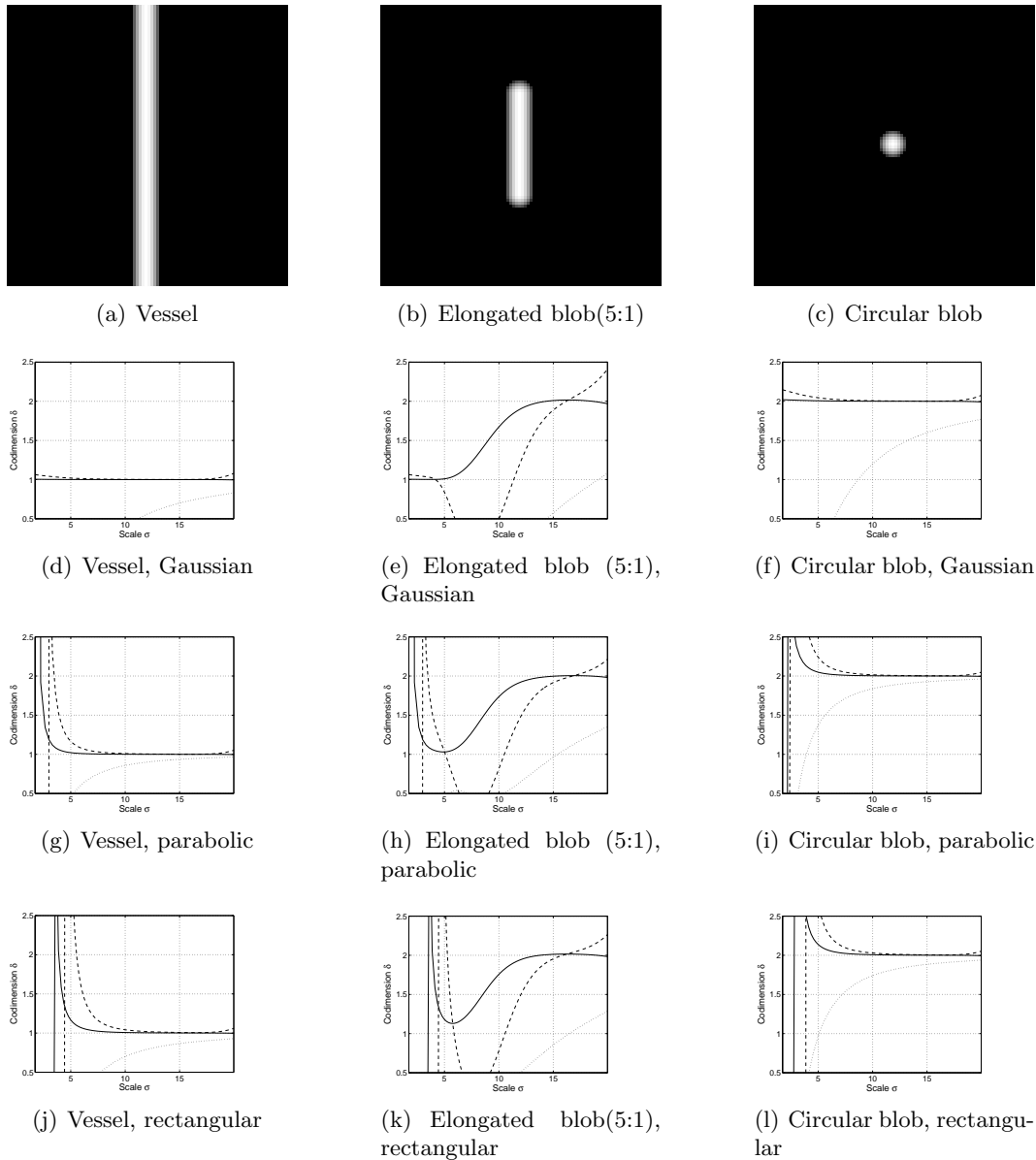


Figure 3.5: Plots of codimension δ versus scale, for different 2D structures (first column: infinite straight vessel; second column: elongated blob, axis ratio 5:1; third column: circular blob) and for different profiles (second row: Gaussian; third row: parabolic; fourth row: rectangular). Codimension is calculated from intensity (solid line) and from Laplacian (dashed line). Dotted line is the asymptotic formula for codimension. Structure half-width: $w = r$. First row is the initial image.

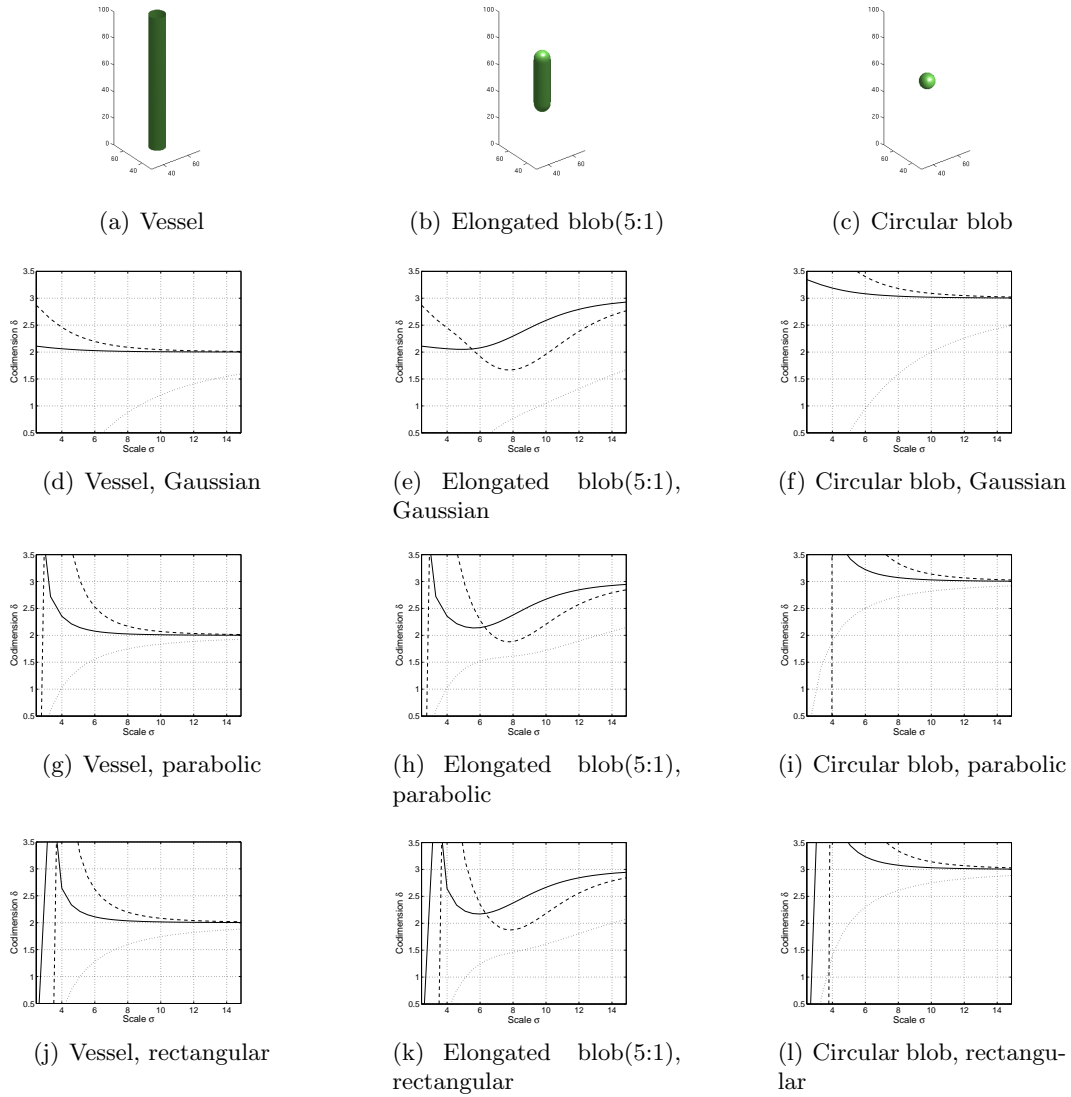


Figure 3.6: Plots of codimension δ versus scale, for different 3D structures (first column: infinite straight vessel; second column: elongated blob, axis ratio 5:1); third column: circular blob and for different profiles (first row: Gaussian; second row: parabolic; third row: rectangular). Codimension is calculated from intensity (solid line) and from Laplacian (dashed line). Dotted line is the asymptotic formula for codimension. Structure half-width: $w = 5$.

The Laplacian method is more sensitive to noise and higher spatial frequencies, but it is completely independent of background.

3.3 Bifurcation Response in Scale-Space

Vascular bifurcations are simply the joining of three blood vessels. The exact geometry was (and still is) a subject of active research, since fluid dynamics simulations at bifurcations lead to a better understanding of the blood dynamics and arterial pathology. However, the use of scale-space specifically eliminates the internal structure from the study of vascular trees. For the purpose of this research, we use a simple model, as illustrated in Figure 3.7 - a simple superposition of three straight semi-infinite vessels of appropriate diameters and at appropriate angles. The fundamental parameter of a vascular bifurcation is the splitting ratio $\alpha = r_2/r_1$, the ratio of the smaller daughter vessel and the larger daughter vessel. Using

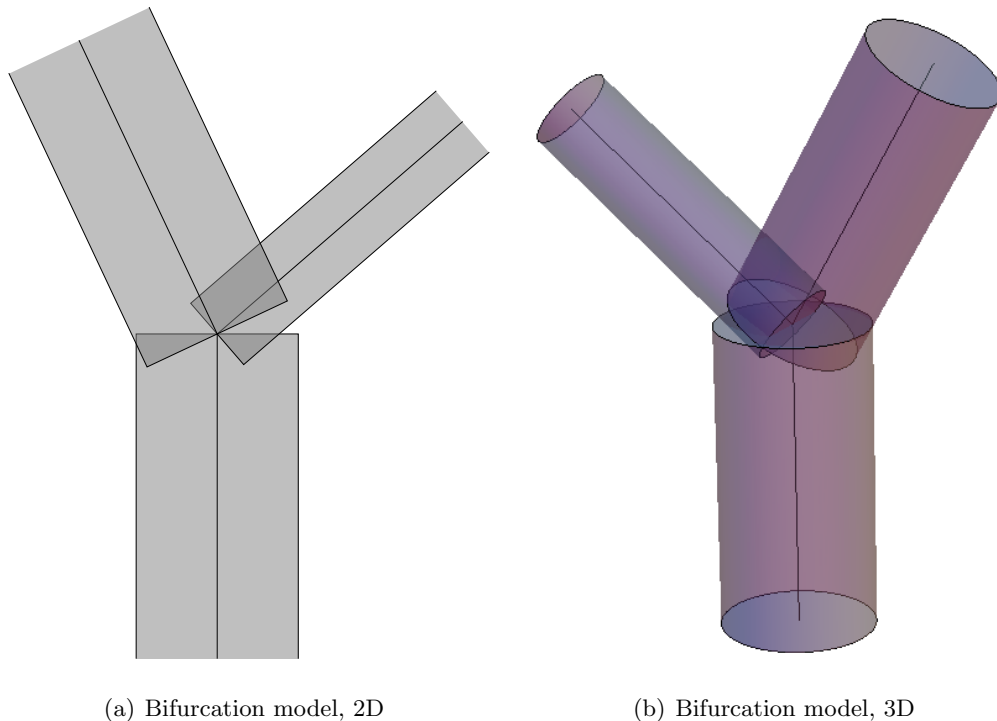


Figure 3.7: A simple model of a vascular bifurcation, represented as a set of three simple straight vessels, in both 2D and 3D

this model, we can calculate the scale-space intensity at the bifurcation using Equation 3.8 for each of the branches and the linear superposition property of the scale-space:

$$V(s) = \sum_{i=0}^2 A_i \left(\frac{w_i}{\sqrt{w_i^2 + s}} \right)^\delta \underset{s \gg w^2}{\approx} \frac{\sum_{i=0}^2 A_i w_i^\delta}{s^{\delta/2}} \quad (3.36)$$

The factor $A_i w_i^\delta$ is simply the cross-section of the vessel i . Equation 3.36 has two main consequences. First, due to Murray’s law, the sum of cross-sections of the daughter vessels is larger than the cross-section of the parent vessel (see Equation A.5. Since a single full vessel can be seen as the superposition of two semi-vessels (or, equivalently, as a limit case of a bifurcation with splitting ratio $\alpha = 0$), it follows that at “large enough” scales, the intensity at the center of a bifurcation is larger than on the centerline of any of the adjoining vessels, even if only slightly. The effect is much more pronounced in 2D (10 to 30 per cent) than in 3D (3 to 13 percent), with the larger increase for symmetric bifurcations. As a result, bifurcations will appear as intensity local maxima at virtually any scale. A typical behavior is illustrated in Figure 3.8 in a 2D geometry for an initial radius of the parent vessel $r_0 = 5$ pixels and symmetric splitting, at scales $\sigma = 5$ and 10.

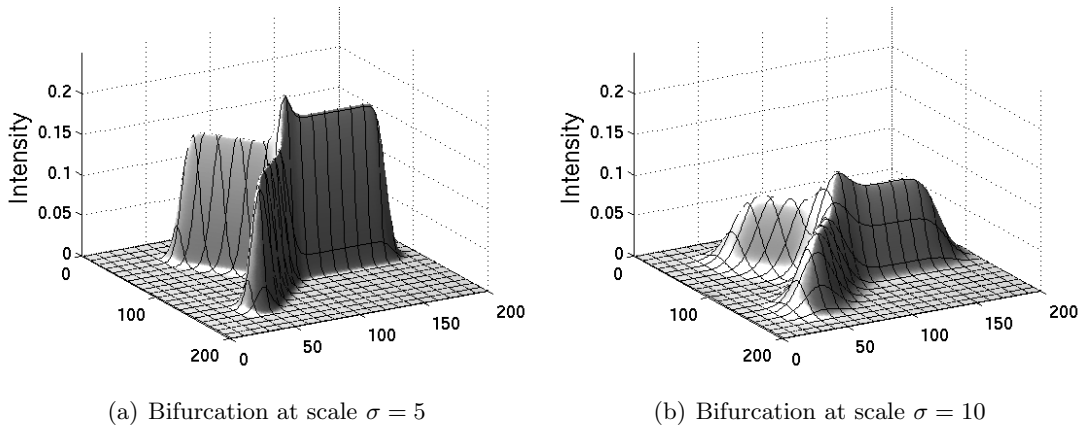


Figure 3.8: Scale space response of an ideal bifurcation, showing a local maximum at the position of the bifurcation.

The other consequence is that the codimension at the center of a bifurcation is the same as the codimension of a blob, a fact which can be used to distinguish between bifurcations

and blobs. Although the intensity variation in scale-space takes a simple form only for large scales, for practical reasons, we use the same formula as for a single localized structure in Equation 3.24. This allows us to obtain the codimension at the bifurcation at smaller scales, comparable with the radius of the parent vessel. The reason this works is that the larger daughter vessel has a radius larger than about 0.8 of that of the parent vessel, while the smaller daughter vessel has less weight due to its smaller diameter.

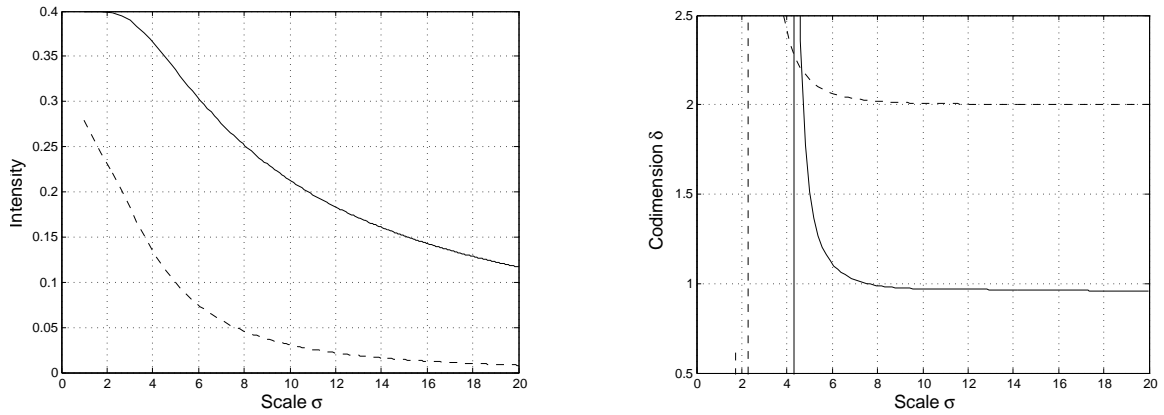
This simple mathematical model has several deficiencies, as can be seen in Figure 3.7. It does not round out the joints between the vessels, and the individual branches overlap. However, for practical vessel structures the largest spatial extent (“diameter”) of these imperfections is at most the largest of the vessel radii coming to the bifurcation, for the following reasons (for details on bifurcation angles, see A.2):

1. The angle between the daughter vessels is roughly 90° , thus their overlap can be contained in a rectangle approximately $r_1 \times r_2$ in size;
2. The angle formed by the daughter and the *extension* of the parent vessel is between 0 and 90 degrees, with larger angles corresponding to smaller radius of the daughter vessel. Therefore, the largest size of this overlap is the radius of the parent vessel.
3. The overlap has an irregular shape, rich in higher spatial harmonics, with a fast decay rate

Since they are strongly localized structures, their codimension is the largest possible, equal to the dimensionality of the space - one unit larger than the codimension of the vessel in the same space. All these factors contribute to a fast decay of the difference between the mathematical model and the true vessel, as illustrated in Figure 3.9(a).

While a more rigorous justification is possible, it is difficult to obtain and gives less insight than a simple numerical experiment. The result estimating the codimension at the bifurcation location is shown by the solid line in Figure 3.9(b). We also note that the perturbation itself, in spite of its more complicated shape, behaves as a localized blob at scales comparable with the parent vessel radius and above.

This property suggests the approach to be used for direct bifurcation detection: transform the image in the scale-space, then look for local maxima at a fixed scale. If the vessels are infinite, this local maximum at the bifurcation will be apparent at all scales; in practical cases, there is a “window of opportunity” (i.e., a range of scales) where this behavior can be



(a) Intensity at center of bifurcation for the full bifurcation (solid line) and for the perturbation alone (dashed line) in scale space

(b) Codimension at center of bifurcation for the full bifurcation (solid line) and for the perturbation alone (dashed line) evaluated at different scales

Figure 3.9: Influence of deviation from mathematical model on bifurcation response in scale-space: intensity and codimension evaluation, for vessels with rectangular profile, with parent radius $r_0 = 6$ and almost symmetric splitting ratio ($\alpha = 0.9$)

observed and used for bifurcation detection, between the “inner scale” and the “outer scale”. In this situation the “outer scale” is simply the scale at which the bifurcation starts to get influence due to diffusion from nearby structures. Since other localized (but unconnected) structures like blobs also present themselves as local maxima, the rate at which intensity decays with scale can be used to distinguish between them.

Chapter 4

Implementation of the Bifurcation Detector

There are two conclusions of the theoretical analysis presented in the previous chapters. First, vascular bifurcations appear as local maxima in images transformed into scale-space, regardless of their initial profile. Therefore, a bifurcation has the characteristics of a blob, even though the appearance of the original image does not suggest it; the local blob-like appearance occurs as soon as the scale is large enough for areas outside the vessel to be incorporated in the diffusion disk, and is most visible at scales where the internal structure of the vessels joining the bifurcation is erased by the diffusion process. This increase, however, is small for 3D (as low as 3% for strongly asymmetric bifurcations) and therefore even a small perturbation can affect the performance based solely on gradient-based detection of intensity local maxima in the scale-space. Since the increase in intensity at bifurcation location (relative to the intensity on vessel centerline) in 2D images is much more significant, it can be used as an additional criterion for localization.

The second conclusion is the loss of one-dimensionality in the components of the Hessian. This is intuitively obvious for symmetric (or almost symmetric) bifurcations. For strongly asymmetric bifurcations, this intuitive approach does not hold – the largest of the daughter vessels has almost the same diameter as the parent vessel and is almost in the same direction. The detailed discussion is presented in Appendix A.

4.1 First Implementation

Vascular bifurcations are not the only structures that can generate maxima in scale-space. Localized maxima in scale-space may correspond to other features in the original image – for example, blobs and fluctuations in vessel width. Fortunately, there are other parameters which can distinguish between these cases, most notably the Hessian of the image intensity at a given scale. As stated before, the Hessian defines an ellipsoid whose axes are along the eigenvectors and the corresponding axis semi-lengths are the magnitudes of the corresponding eigenvalues, λ_k . We use the same notation as in Frangi [13], with the eigenvalues ordered according to their absolute value, the lowest index corresponding to the eigenvalue with the lowest absolute value ($|\lambda_1| \leq |\lambda_2| \leq |\lambda_3|$):

- **Blobs:** these are seen as local maxima in scale-space, but their codimension is 2 in 2D images and 3 in volumetric images. In this case, all eigenvalues of the Hessian are comparable [13]
- **Vessel thickening (or bulging vessel):** the codimension of these features is 1 in 2D images and 2 in volumetric images, but the eigenvalues of the Hessian have a large ratio [13]. In 3D, the two largest eigenvalues are comparable in magnitude and have the same sign.
- **Bifurcations:** Since they are essentially the joining of three vessels, the codimension of these features is also 1 in 2D images and 2 in volumetric images, but their asymmetry leads to a low vesselness, due to comparable values of the Hessian eigenvalues.
- **Plate-like structures** in 3D, with only one of the Hessian eigenvalues with a significantly large value.

The criteria used to distinguish between the different cases are summarized in Table 4.1, which uses the same notation as in Frangi [13]. We can mimic the vesselness equation proposed by Frangi et al., we synthesized the results into a single unifying *bifurcationness* formula:

$$\mathcal{B} = \left(1 - \exp\left(-\frac{R_a^2}{2\alpha^2}\right)\right) \left(1 - \exp\left(-\frac{R_b^2}{2\beta^2}\right)\right) \left(1 - \exp\left(-\frac{S^2}{2c^2}\right)\right) \cdot \exp(-(\nabla I(x, s)/(\kappa g))^2) \quad (4.1)$$

Table 4.1: Possible patterns of bright structures in 2D and 3D, based on Hessian eigenvalues and codimension

δ	$ \lambda_2/\lambda_1 $ ($ \lambda_3/\lambda_1 $ for 3D)	Pattern
1	Small	2D bifurcation
1	Large	2D vessel
1	Large	3D plate (also $\lambda_2 \sim \lambda_3$)
2	Small	2D blob, 3D bifurcation
2	Large	3D vessel
3	Small	3D blob

This equation is the natural choice for localized structures. It incorporates all the required elements, using the common Gaussian function for penalizing deviations from the ideal value. Just as in Frangi et al., R_b encodes how close the local structure is to a blob, encoded in the second in Equation 4.1). R_b is defined from the geometrical parameters of the Hessian ellipsoid, from the volume and the largest cross-sectional area; in 3D, $R_b = \frac{|\lambda_1|}{\sqrt{|\lambda_2\lambda_3|}}$, while in 2D it takes the form $R_b = \frac{|\lambda_1|}{|\lambda_2|}$. Here we are interested in blob-like structures, with R_b as large as possible (the simple Gaussian function *decreases* with increasing R_b). The first factor, containing $R_a = |\lambda_2|/|\lambda_3|$, is used to eliminate plate-like structures. The parameters R_a and R_b are *relative* values, so noise or other perturbations can also generate significant signals based only on these parameters. For this reason, a saliency measure is needed to eliminate spurious signals (the third factor). The parameter S encodes the saliency of the structure, with S^2 being the sum of squares of all Hessian eigenvalues (the Frobenius norm of the Hessian matrix). For the constants used in these terms, we used the same values as in [13]: $\alpha = 0.5$, $\beta = 0.5$ and c is set to half of the maximum value of the Hessian norm. The final factor encodes the condition for a local maximum: we need the gradient to be as small as possible. In this term, g is the maximum value of the gradient, and the constant κ was set to 0.01. This factor eliminates the contribution of edges to our bifurcationness measure.

The bifurcationness measure takes into account all the required elements:

1. Transform the image to scale-space;
2. At a scale larger than the size of the largest vessel, look for local maxima (penalize large gradients);

3. Penalize points with large stickness (large R_b); these are more likely due to fluctuations in image intensity on the vessel rather than bifurcations
4. Penalize points with large plate component (large R_a ; in 3D images only)
5. Penalize points with large gradient

An alternative is to calculate the maximum measure at multiple scales and take as final measure the maximum across scales. Since this measure by itself does not distinguish between bifurcations and other localized structures, the additional codimension filter is used: keep only the maxima with codimension 1 (in 2D images) or 2 (in 3D images) at the scale of maximum bifurcationness. The scale-space properties are further used by selecting only those maxima with appropriate codimension (as calculated at a scale 25% larger than the scale of maximum response – large enough for the dimensional characteristics of the vessel to be seen, but not so large that other structures will influence it in a dense environment) and eliminating the features with low characteristic scale (pixels in the image have uncorrelated noise, so an isolated noise pixel has a characteristic scale of 1). This scale selection is in agreement with the common practice of ignoring any signal with scale below 1–2 as being too influenced by noise.

The tests done with this filter showed good results in 2D, but failed to reveal bifurcations in 3D images, even in ideal simulated images. This failure was tracked to the presence of the gradient penalty factor. As stated before, the relative local increase is too small to be useful. Simply eliminating the gradient-based term is sufficient to allow this filter to detect all test bifurcations in 3D, without affecting the detection of bifurcations in 2D images. It is also worth noting that the most widely used blob detectors (as well as Frangi’s vesselness) use only the Hessian, without any gradient information, even though the analysis is based on having a zero gradient.

The bifurcationness filter has a strongly nonlinear response with respect to Hessian eigenvalues, especially in 3D images. An analysis of of this nonlinear response and comparisons with simpler alternatives is presented in Appendix C in the context of vessel enhancement. A comparison of this bifurcationness (without the gradient factor) with other bifurcation detector versions is done in the next Section.

4.2 Eigenvalue Analysis of Vascular Bifurcations

The failure of the initial bifurcationness filter, especially in 3D, shows that we can not build a filter based only on the fact that bifurcations are localized structures and on the intuitive Gaussian penalties for deviation from desired values, and that a more detailed investigation of the Hessian eigenvalues at bifurcations is needed.

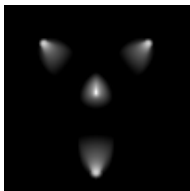
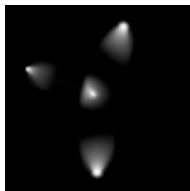
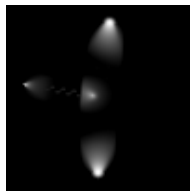


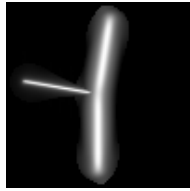
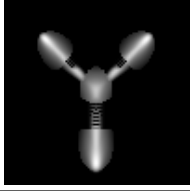
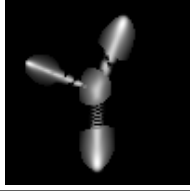
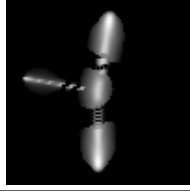
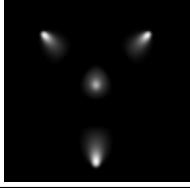
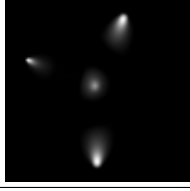
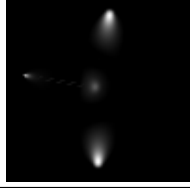
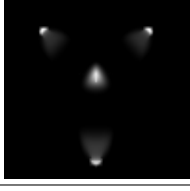
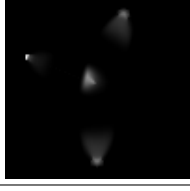
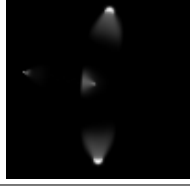
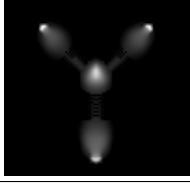
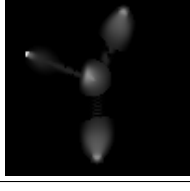
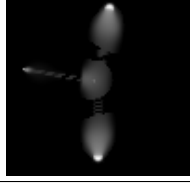
For practical purposes, bifurcations present themselves as areas with high intensity (the same as for the vessels), but with a break in their symmetry. It seems intuitively obvious that while vessels present themselves as elongated structures (with two normal directions, therefore the Hessian matrix has two large and comparable eigenvalues - a strong plate tensor component), this condition breaks at the end of vessels and at bifurcations. These structures will present themselves with a strong ball tensor component. This can be explained by the fact that blood vessel have strong variation perpendicular to the vessel centerline and only weak variation along it (thus the strong plate tensor component), while the discontinuity at the end manifests itself in a strong intensity variation along the centerline, resulting in a relatively large eigenvalue and therefore a strong ball tensor component. While this intuition is valid for almost symmetric vascular bifurcations, it is not valid for strongly asymmetric bifurcations, where the largest daughter vessels has almost the same diameter and direction as the parent vessel. In situations like this, however, it is the end of the smaller daughter vessel that gives the strong signal identifying the bifurcation.

In this Section we investigate the structure of eigenvalues and of various eigenvalue combinations (including the standard blob detectors, Laplacian and Determinant of Hessian) at bifurcations, in both 2D and 3D.

4.2.1 Eigenvalue Analysis in 2D

In 2D images, the analysis is straightforward. There are only two eigenvalues of the Hessian, and the number of combinations is very limited. The results are illustrated in Table 4.2. The splitting ratios illustrated are representative for the range of bifurcation ratios found in practical situations, from completely symmetric ($\alpha = 1$) through intermediate ($\alpha = 0.5$) and extremely asymmetric ($\alpha = 0.25$). As stated in Section 3.1, there are only two possible image structures: blobs and ridges/edges, with other structures being a combination of these. In Table 4.2 we show the possible structures for bifurcations in 2D images. Note that for visualization purposes, each image was scaled so that the maximum for each is 1.

Table 4.2: Eigenvalue functions for 2D bifurcations, filtered for areas with all eigenvalues negative

	$\alpha = 1$	$\alpha = 0.5$	$\alpha = 0.25$
λ_1			
λ_2			
ΔL			
$\text{Det}(\mathcal{H})$			
$1 - \exp\left(-2\left(\frac{\lambda_1}{\lambda_2}\right)^2\right)$			
$\exp\left(-2\left(1 - \frac{ \lambda_1 }{ \lambda_2 }\right)^2\right)$			

Therefore, a direct comparison of images is not possible. In all cases, the values were calculated at each scale, then the maximum of the absolute value was taken across all scales at each spatial point.

The smallest eigenvalue, λ_1 , has significant values only in areas where the one-dimensionality of the vessels breaks - the end of vascular branches and at the bifurcation. Since we are interested only in bright structures on dark background, a localized structure will have both eigenvalues negative; this condition is used to filter out local structures corresponding to minima or saddle points. We can see that the bifurcation location is well defined, even in the most asymmetric bifurcation (bifurcation ratio $\alpha = 0.25$, corresponding to an area ratio of about 0.06, smaller than the smallest area ratio of 0.1 reported in the literature.

The largest eigenvalue, λ_2 , follows closely the full vascular structure. This is expected, since λ_2 is the sum of the two possible components of image structures. The difference $|\lambda_2| - |\lambda_1|$ is not showed, since it characterizes only the vessels and not the bifurcations.

The classical blob detectors, the Laplacian ΔL and the Determinant of Hessian $\text{Det}(\mathcal{H})$ are invariant to rotations (due to the tensor properties of the Hessian). They have the advantage that they can be expressed without explicitly calculating the eigenvalues. In the principal coordinate system (where the Hessian becomes diagonal), they become simply $\Delta L = \lambda_1 + \lambda_2$ and $\text{Det}(\mathcal{H}) = \lambda_1 \lambda_2$. The Laplacian is the worst choice, since it gives strong response along the vessels and gives only very poor localization. The reason the images for the Laplacian show irregular response along the vessels is the condition $\lambda_1 < 0$. Along the vessel, λ_1 has very small values and fluctuates around 0, resulting in on-and-off values. The Determinant of Hessian has λ_1 as one of the factors, so it can not have a significant value unless λ_1 is large. Therefore, it has the same localization properties as λ_1 , but is sharper around the maxima, since it is quadratic, while λ_1 is linear. For the same reason, the bifurcation signal is stronger with the simple ballness filter λ_1 .

The last two operators are inspired by the Frangi vesselness filter, They seek to enhance areas with large relative ball component $|\lambda_1|/|\lambda_2|$ using Gaussian penalty. The first of these operators works the same as the Frangi vesselness filter, using Gaussians centered at 0. Since the ideal value of $|\lambda_1|/|\lambda_2|$ for localized structures is 1, one could simply use a Gaussian centered at 1, the way the second operator does. Both of these filters need the additional saliency enhancing factor $1 - \exp(-2(S/S_{max})^2)$, which is not shown in the table for compactness. The Gaussian centered at 1, while it seems to be a more natural choice, is actually a worse choice, due to its flat maximum at the desired value. At high asymmetry,

however, the first Frangi-style filter has a secondary maximum with an amplitude comparable with the signal from the real bifurcation located at about 8 pixels away from the true bifurcation, even with the total absence of noise.

Thus, the only viable choices for the base of the bifurcation locator are λ_1 , $\text{Det}(\mathcal{H})$ and the variation of the Frangi filter. They all show strong signals only at the end of vascular branches and the bifurcation, even for extreme asymmetry of the bifurcation. The images in Table 4.2 were obtained for a radius of the parent branch of 5 pixels, so the small daughter vessel has a theoretical radius of 1.2 pixels. At this radius, pixelation effects can be seen on the small daughter vessel.

4.2.2 Eigenvalue Analysis in 3D

For 3D images, there are three eigenvalues and considerably more possibilities to combine them, even if we only use meaningful combinations. The results were split in Tables 4.3 – 4.6. The first two tables contain the eigenvalues (section in the plane of the bifurcation and a 3D representation of the isosurface), as well as their first order combinations; λ_1 is the ball component (localized structures), $|\lambda_2| - |\lambda_1|$ is the plate component (linear structures) and $|\lambda_3| - |\lambda_2|$ is the stick component (plate-like structures). In all cases, the value investigated was taken as the maximum over scales. For visualization purposes, the cross-sections were amplified and higher intensities were saturated. The level of the isosurfaces, set as a fraction of the highest amplitude, was set at different levels for each bifurcation ratio, to emphasize characteristic behavior, but was kept constant for a given bifurcation ratio. The bifurcations in these figures were embedded in a $100 \times 100 \times 100$ pixel volume, with a radius of the parent vessel of 5 pixels. The bifurcation angles and the radii of the daughter vessels were calculated from the formulas presented in Appendix A. The vessel profile used for illustration was parabolic, since it is finite in extent and looks more like the profile of actual vessels. The Gaussian and rectangular profiles are too idealized and do not bring additional insight, so they were omitted.

We can see in Tables 4.3 and 4.4 that just as in the 2D case, the smallest eigenvalue λ_1 has values localized in areas where the one-dimensionality of the vessel breaks: at the end of vessels and at the bifurcation, with significant values even for the most extreme bifurcation ratios ($\alpha = 0.25$). The other eigenvalues, λ_2 and λ_3 , follow closely the whole structure. More insight can be obtained by looking at structure-specific eigenvalue combinations. It is no surprise that $|\lambda_2| - |\lambda_1|$, representing the plate component of the Hessian tensor (and

Table 4.3: Eigenvalue functions for 3D bifurcations (sections), filtered for areas with all eigenvalues negative. λ_1 is the ball component (localized structures), $|\lambda_2| - |\lambda_1|$ is the plate component (linear structures) and $|\lambda_3| - |\lambda_2|$ is the stick component (plate-like structures)

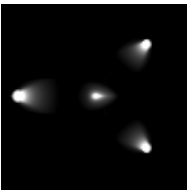
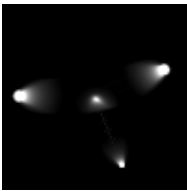
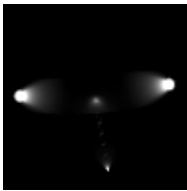












	$\alpha = 1$	$\alpha = 0.5$	$\alpha = 0.25$
λ_1			
λ_2			
λ_3			
$ \lambda_2 - \lambda_1 $			
$ \lambda_3 - \lambda_2 $			

Table 4.4: Eigenvalue functions for 3D bifurcations (isosurfaces), filtered for areas with all eigenvalues negative. λ_1 is the ball component (localized structures), $|\lambda_2| - |\lambda_1|$ is the plate component (linear structures) and $|\lambda_3| - |\lambda_2|$ is the stick component (plate-like structures)

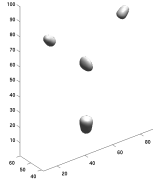
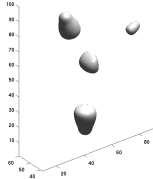
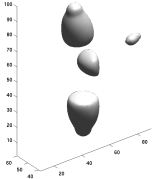
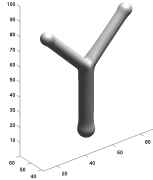
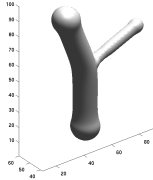
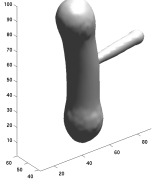
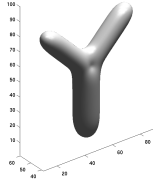
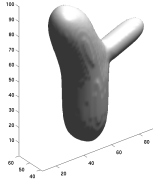
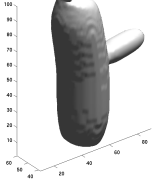
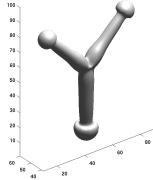
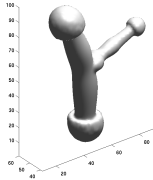
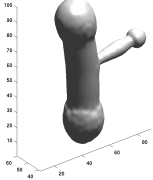
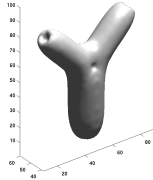
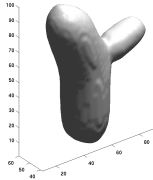
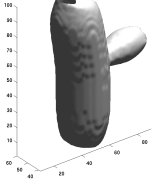
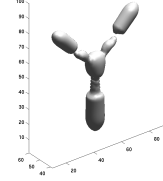
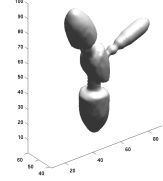
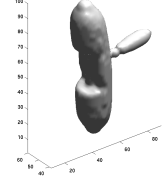
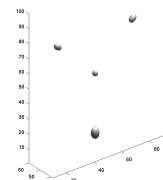
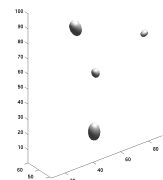
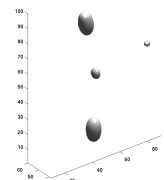
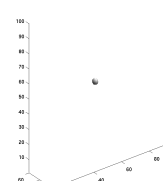
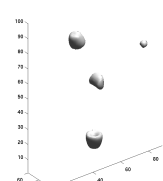
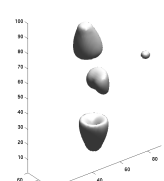
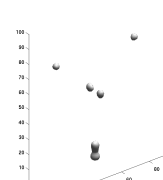
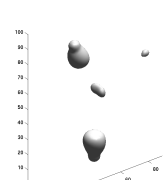
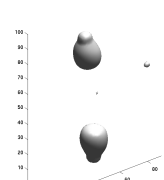
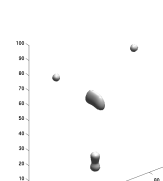
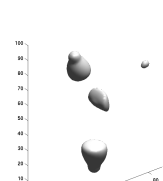
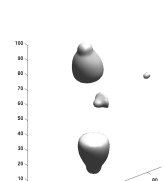
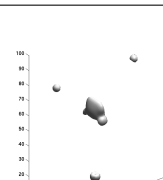
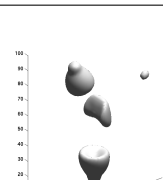
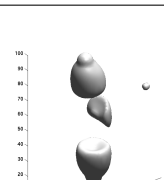
	$\alpha = 1$	$\alpha = 0.5$	$\alpha = 0.25$
λ_1			
λ_2			
λ_3			
$ \lambda_2 - \lambda_1 $			
$ \lambda_3 - \lambda_2 $			

Table 4.5: Detectors for 3D bifurcations (sections), filtered for areas with all eigenvalues negative. The last three operators also have a saliency-based factor $(1 - \exp(-2S_r^2))$, not shown in the table.

	$\alpha = 1$	$\alpha = 0.5$	$\alpha = 0.25$
$\Delta L = \lambda_1 + \lambda_2 + \lambda_3$			
$\text{Det}(\mathcal{H}) = \lambda_1 \lambda_2 \lambda_3$			
$ \lambda_1 (\lambda_3 - \lambda_2)$			
$\left(1 - e^{-\frac{R_A^2}{2a^2}}\right) \left(1 - e^{-\frac{R_B^2}{2b^2}}\right)$			
$\left(1 - e^{-\frac{R_B^2}{2b^2}}\right)$			
$e^{-\frac{R_A^2}{2a^2}} \left(1 - e^{-\frac{R_B^2}{2b^2}}\right)$			

Table 4.6: Detectors for 3D bifurcations (isosurfaces)

	$\alpha = 1$	$\alpha = 0.5$	$\alpha = 0.25$
$\Delta L = \lambda_1 + \lambda_2 + \lambda_3$			
$\text{Det}(\mathcal{H}) = \lambda_1 \lambda_2 \lambda_3$			
$ \lambda_1 (\lambda_3 - \lambda_2)$			
$\left(1 - e^{-\frac{R_A^2}{2a^2}}\right) \left(1 - e^{-\frac{R_B^2}{2b^2}}\right)$			
$\left(1 - e^{-\frac{R_B^2}{2b^2}}\right)$			
$e^{-\frac{R_A^2}{2a^2}} \left(1 - e^{-\frac{R_B^2}{2b^2}}\right)$			

thus representative to linear structures like vessels), follows the whole tree and has a dip at the actual bifurcation location. The value of $|\lambda_3| - |\lambda_2|$ is the stick component of the Hessian tensor, and identifies surface-type structures, so it is expected to be 0 or a low value. However, remember that the eigenvalue analysis is done at the center of structures, where the gradient is 0. Since there is no enforcement of the zero gradient, this component also outlines surfaces between bright and dark areas. Therefore it outlines the wall of the vessel. The tubular structure is not visible in the isosurface plots, but it is obvious in the cross-sections. What is surprising is that this component is nonzero at the location of the actual bifurcation. This is easier seen in the cross-sections for $\alpha = 1$ and $\alpha = 0.5$. While surprising, this has a simple explanation. From the bifurcation point, the participating branches spread in different directions in a plane, so at least for a small volume around the bifurcation it will have the behavior of a flat structure. An exact mathematical model is impractical, so we rely on intuitive models and experimental observations.

The next two tables (4.5 and 4.6) show other eigenvalue combinations, the candidates for bifurcation detection. All of the candidates were filtered with the condition for a local maximum, that all of the Hessian eigenvalues must be negative. No other enforcement (e.g., low magnitude for the gradient) was applied. The first candidate is the Laplacian (mathematically, the trace of the Hessian; due to invariance to coordinate change, it is also the sum of all eigenvalues), one of the standard blob detectors. Just as in the 2D images, the Laplacian has strong response not only at the bifurcation and at the vessel ends, but at all positions along the vessel branches. Again, the irregular response of this filter along the vessel branches is due to fluctuations in the sign of λ_1 , which has very low values around the middle of the branches. The next operator is another classical blob detector, the Determinant of Hessian. Since $\text{Det}(\mathcal{H}) = \lambda_1\lambda_2\lambda_3$, it is a nonlinear operator dominated by λ_1 , thus emphasizing the ball component more than other operators (it is an operator of the third degree). The other components of the Hessian add some emphasis to the ball component only in plate and stick areas, although not to the same degree.

The analysis of Hessian tensor components shows that at bifurcations both the ball and the stick tensor components have significant values at the location of the bifurcation. This suggests a new operator, $|\lambda_1|(|\lambda_3| - |\lambda_2|)$, illustrated in the third row of Tables 4.5 and 4.6. We can see that this operator emphasizes very well the bifurcation, while the signal from the end of vessels is significantly diminished. In fact, the signal from the bifurcation is the strongest in all cases, unlike any of the other operators investigated (which have the

strongest signal at the end of the parent vessel). The tubular structure of the stick tensor component is seen in the split image at the end of vessels in the cross-sections. The signal at the bifurcation is a solid blob, with a maximum indicating the location of the bifurcation, even if at lower bifurcation ratios it appears as a curved shell. Again, remember that the intensity cross-sections in Table 4.5 are normalized to the maximum intensity in the corresponding image, and that the isosurfaces in Table 4.6 are chosen to emphasize the differences between the operators at a given bifurcation ratio, not for the same operator at changing the bifurcation ratio. Thus, the larger volume at $\alpha = 0.25$ is not an indication of a stronger response than at $\alpha = 1$.

For completeness, we present operators using other nonlinear combinations of eigenvalues. They are based on one of the first scale-space operators used specifically for processing vascular images, the Frangi vesselness. In short, this operator uses eigenvalue combinations with geometrical interpretation as Hessian ellipsoid axes and sections. This operator is discussed in detail in Appendix C. There we also discuss a reinterpretation of the operator in terms of Hessian tensor components. The eigenvalues of the Hessian are processed in three dimensionless parameters: $\mathcal{R}_A = |\lambda_2|/|\lambda_3|$, $\mathcal{R}_B = |\lambda_1|/\sqrt{|\lambda_2\lambda_3|}$ (which can be simplified to $\mathcal{R}_B = |\lambda_1|/|\lambda_3|$, the relative ballness) and $\mathcal{S} = \sqrt{\lambda_1^2 + \lambda_2^2 + \lambda_3^2}$ (which can be simplified to $\mathcal{S} = |\lambda_3|$), the saliency of the local signal. The parameters \mathcal{R}_A and \mathcal{R}_B have values only between 0 and 1; the value of \mathcal{S} is unbounded. It is better if this value is transformed into a dimensionless value as well, by normalizing it to the maximum value, so it also takes values between 0 and 1. The normalization is done *at each scale separately*. The Frangi operator emphasizes a small \mathcal{R}_B (therefore small λ_1 , characteristic for structures extended in at least one direction), while at the same time emphasizing large values for λ_2 (large \mathcal{R}_A , characteristic for structures confined in two directions). Using a similar technique, we can write a similar blob/bifurcation detector as

$$\mathcal{B} = \left(1 - e^{-\frac{R_A^2}{2a^2}}\right) \left(1 - e^{-\frac{R_B^2}{2b^2}}\right) \left(1 - e^{-\frac{S^2}{2c^2}}\right) \quad (4.2)$$

where a , b and c are tunable parameters; a good value for all these parameters is 0.5 (see discussion of the transfer function in Appendix C). The cross-sections in Table 4.5 show that this operator gives a weak signal at the actual bifurcation, especially when compared with the signals at the end of vessels. The isosurface of the signals complete the analysis of this operator: for equal splitting ratio ($\alpha = 1$), this operator presents two clearly distinct maxima, on each side of the bifurcation plane. When the bifurcation ratio is changed to

$\alpha = 0.5$, the local maximum at the bifurcation looks like a thin line perpendicular to the plane of the bifurcation. At the most extreme bifurcation ratio investigated, $\alpha = 0.25$, there is a single maximum at the location of the bifurcation, but its amplitude is very small and likely to be drowned in noise. The small response of this filter at the actual bifurcation can be explained if we remember that the stick tensor component, penalized by the first factor in 4.2, has a significant value at the bifurcation. Thus, the value of the second factor is significantly reduced at the actual bifurcation; depending on the shape of the response, this may lead to secondary maxima outside the bifurcation. Further tests were performed with variants of this operator, one without the plate penalty

$$\mathcal{B}_1 = \left(1 - e^{-\frac{R_B^2}{2b^2}}\right) \left(1 - e^{-\frac{S^2}{2c^2}}\right) \quad (4.3)$$

and one *encouraging* the plate component, similar to $|\lambda_1|(|\lambda_3| - |\lambda_2|)$

$$\mathcal{B}_2 = e^{-\frac{R_A^2}{2a^2}} \left(1 - e^{-\frac{R_B^2}{2b^2}}\right) \left(1 - e^{-\frac{S^2}{2c^2}}\right) \quad (4.4)$$

The response of these two operators at the bifurcations is significantly improved. However, the strongly nonlinear transfer functions play a significant role in the rather irregular shape of the isosurfaces and may generate, under certain circumstances, secondary maxima, depending not only on bifurcation ratio, but also on orientation (due to differences in discretization error). This effect can be seen, for example, in the multiple lobes of \mathcal{B}_1 at $\alpha = 0.25$ and \mathcal{B}_2 at $\alpha = 1$ isosurfaces. These secondary maxima are in proximity of the actual bifurcation, so they are usable, but need to be filtered out or refined to the actual location by an additional processing step (e.g., based on machine learning). Typically, this additional step is computationally expensive, and it is better to use operators which do not generate additional work.

In conclusion, many operators can be built to detect bifurcations in 3D. Unlike the 2D case, where the various operators were equivalent to each other, in 3D there are more parameters and more significant combinations. These are not equivalent to each other. In fact, the operators that intuitively enhance better the characteristic of bifurcations are not particularly good, generating spurious local maxima which complicate postprocessing. The recommended approach is based on the “simpler-is-better” approach, satisfied by $|\lambda_1|$, $\text{Det}(\mathcal{H})$ and $|\lambda_1|(|\lambda_3| - |\lambda_2|)$.

4.3 Comparison with corner detectors

We have previously mentioned that corner detectors are not appropriate for bifurcation detection because they are designed to follow the boundary between bright and dark areas in the image, while bifurcations are the intersection of ridges. In this Section, we provide some examples of using corner detection for bifurcation detection in 2D images. There are three candidates: the Harris corner detector, the Shi-Tomasi detector, and the curvature of level curves operator. The first two use the structure tensor, and may be of some use in the case of bifurcations, since the original definition tracks large intensity variations in all directions. The latter is a special combination of derivatives of first and second degree; since the level curves follow the contour of the vascular branches, this detector would generate multiple strong responses outside the vessels at each bifurcation. All of these can be used in the scale-space framework. The Harris and the Shi-Tomasi detectors can be easily generalized to 3D images; the curvature of level curves operator has to be reworked completely and reinterpreted in terms of the principal curvatures of the isosurfaces.

The structure tensor is based on the gradient vector (I_x, I_y) , taking into account some smoothing (with weight w):

$$A = \sum_{u,v} w(u,v) \begin{pmatrix} I_x^2 & I_x I_y \\ I_y I_x & I_y^2 \end{pmatrix} = \begin{pmatrix} \langle I_x^2 \rangle & \langle I_x I_y \rangle \\ \langle I_y I_x \rangle & \langle I_y^2 \rangle \end{pmatrix} \quad (4.5)$$

The single-point structure tensor is a stick tensor (for the stick/ball classification, see Section 3.1). The smoothing (the term was used in the early papers) or averaging (term used in more recent papers) is applied *to the tensor itself*. Adding stick tensors with different directions results in a tensor with *both* ball and stick components. Strong gradients give more weight to their neighborhood, while gradients of different directions combine to give a less directional tensor (a ball tensor, or at least a tensor with a strong ball component). In a multiscale approach, the spatial derivatives are calculated at a given scale, then the averaging is done with a weight proportional with the scale (equal or slightly larger). The summary of calculating the structure tensor is:

1. Calculate the image at scale t
2. Calculate the first order derivatives of the image at scale t , L_x and L_y . These two steps can be combined by calculating directly the derivatives at scale t .

3. Calculate the components L_x^2 , $L_x L_y$, and L_y^2
4. Average each of these components using an additional scale-space transform with scale w ; we used $w = t$, to reuse the transformation kernel.
5. Do eigenvalue analysis of the resulting averaged tensor.

The well-known Harris corner detector [17] is defined based on the sum of squared differences between two patches, one over the area and one slightly displaced (they call it “autocorrelation detector”). The interpretation reduces to analyzing the eigenvalues λ_1 and λ_2 of A in the following way: A should have two “large” eigenvalues for an interest point. Based on the magnitudes of the eigenvalues, the following inferences can be made based on this argument:

1. If both eigenvalues are small, then this pixel has no features of interest (the region is of approximately constant intensity).
2. If one eigenvalue is small and the other one is large, then the local autocorrelation function is ridge-shaped and an edge is found.
3. If both eigenvalues have large positive values, then a corner is found.

Harris and Stephens note that the corner measure must be a function of the eigenvalues alone, on grounds of rotational invariance. Also, they state that it is attractive use the trace and determinant of the structure matrix, since this avoids explicit eigenvalue decomposition, as the trace and determinant of a structure tensor are also rotation invariant. Instead, they suggest the corner response R , where κ is a tunable sensitivity parameter:

$$R = \lambda_1 \lambda_2 - \kappa (\lambda_1 + \lambda_2)^2 = \text{Det}(A) - \kappa (\text{Tr}(A))^2 \quad (4.6)$$

This measure is positive in corner regions, negative in edge regions and small in flat regions. The constant κ has typical values between 0.05 and 0.15; in our tests, we used the middle value of 0.1. The particular value of the constant influences the performance of the detector, but not the general behavior, which is the purpose of this Section.

In [42], Shi and Tomasi follow a similar method, using a small window around the point, but conclude that in practice it is sufficient to use the smaller eigenvalue, λ_1 , as long as it is greater than a predefined threshold λ :

$$\min(\lambda_1, \lambda_2) > \lambda \quad (4.7)$$

and that this measure is more reliable than the Harris detector.

Using the ball/stick decomposition interpretation in Section 3.1, the Shi-Tomasi corner detector simply looks for regions with strong ball component, regardless of the stick component, while the Harris detector tries to find a balance between the two. In a scale-space approach, these measures are calculated at all scales then at each spatial point the maximum measure over scales is taken.

The curvature of level curves is a differential operator built from the first and second order derivatives of image intensity in scale-space. Its use is extensively described in [28] and [26]. The expression of this operator is (using normalized derivatives, to be able to compare values across scales)

$$\kappa(x, y; t) = L_x^2 L_{yy} - 2L_x L_y L_{xy} + L_y^2 L_{xx} \quad (4.8)$$

then the negative minima and positive maxima (in other words, all maxima of the absolute value) are taken across the scales.

To check how well suited are these detectors for bifurcation detectors, we used the images shown in Figure 4.1. The first images are synthetic bifurcations; without noise and with straight branches, they are as close to ideal as possible. The profile of the vessels is parabolic, mimicking the decrease in intensity of vessels from centerline to edges, without the infinite decay of the Gaussian. The original images are 100×100 pixels.

The first image is a symmetric bifurcation ($\alpha = 1$); the response of the filters are shown in Figure 4.2. The responses were scaled so that in each image the maximum response is 1. For the corner The Harris and the Shi-Tomasi detectors give similar results. Somewhat surprising, they give strong response only in one of the corners, along the bisector of the angle between the daughter vessels. More surprising is the strong response of the filters at the location of the actual bifurcation. There is, however, a simple explanation for this. Around the bifurcation, the intensity decreases in all directions with the exception of the centerline of the vessels. Therefore, when doing the tensorial averaging required to obtain the structure tensor, all these different directions are added as tensors, resulting in a strong ball component of the structure tensor. Weak responses are seen in the other angles for the Shi-Tomasi detector; all three corners are seen at a single, low scale, where the response at the actual bifurcation is not seen. In their native, unmodified form, both detectors show two pronounced local maxima around the bifurcation – one only a few pixels from the bifurcation and one farther away between the daughter branches. If the condition for local maxima (all

Figure 4.1: Initial images for testing detectors. First row: 2D synthetic symmetric bifurcation, parabolic profile, bifurcation ratio $\alpha = 1$ and $\alpha = 0.4$; second row: noisy angiogram and retinal image from the DRIVE database

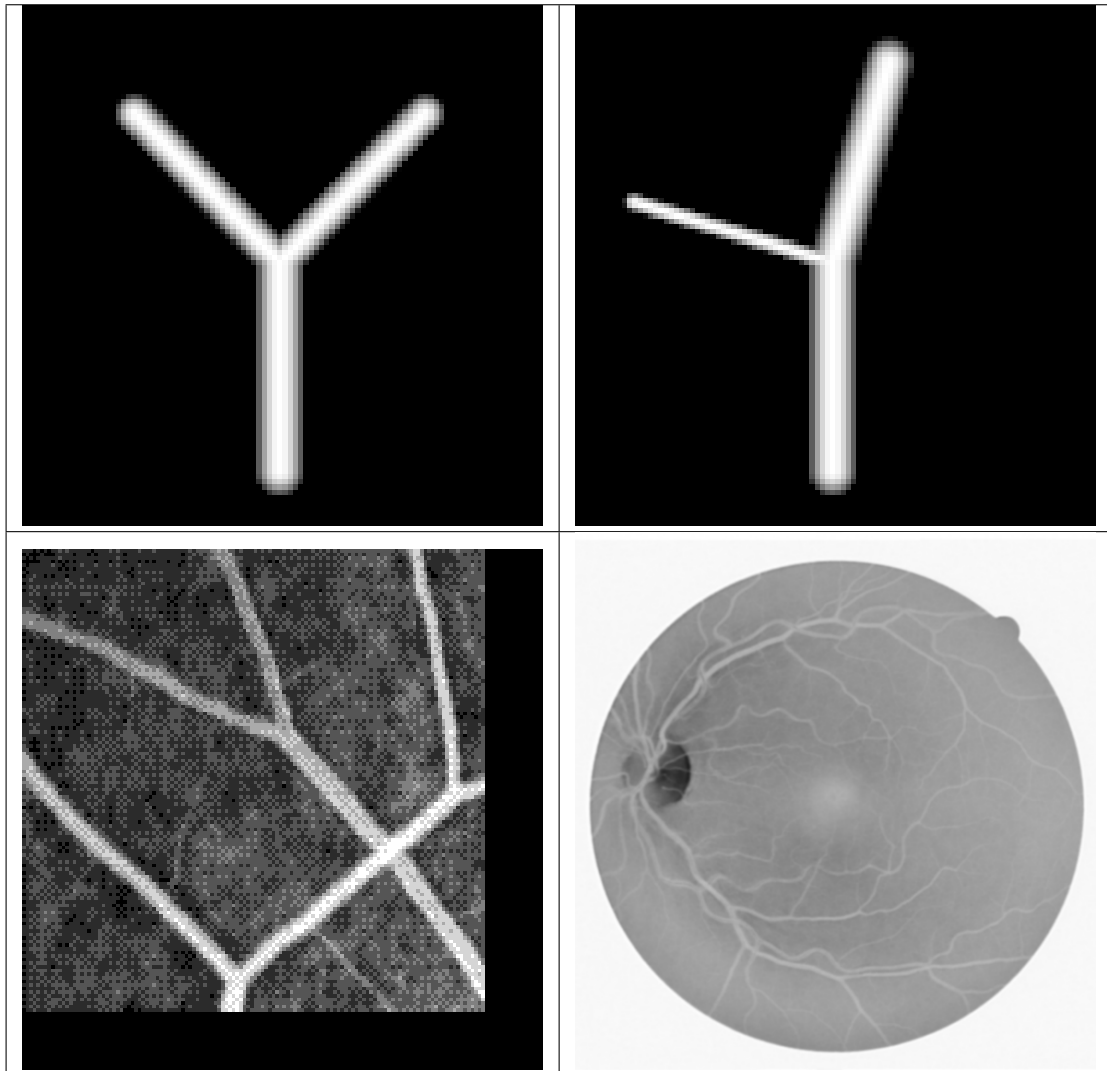


Figure 4.2: Response of corner detectors (from left to right, Harris, Shi-Tomasi, curvature of level curves in the first row), the same corner detectors restricted to areas with all Hessian eigenvalues negative (second row), and Hessian-based bifurcation detectors (from left to right, λ_1 , Determinant of Hessian, Frangi-style). Initial image is a 2D synthetic symmetric bifurcation, parabolic profile

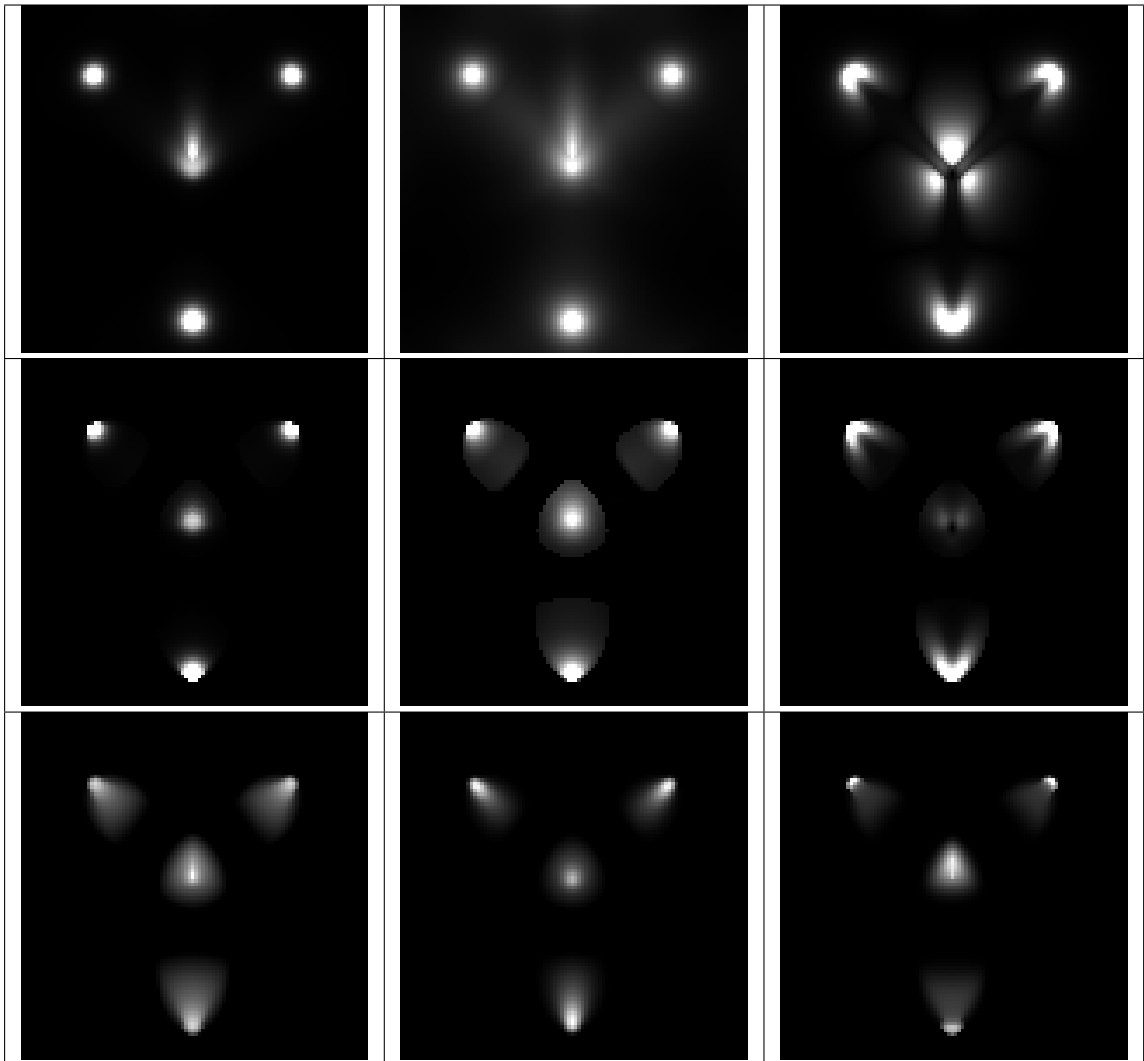
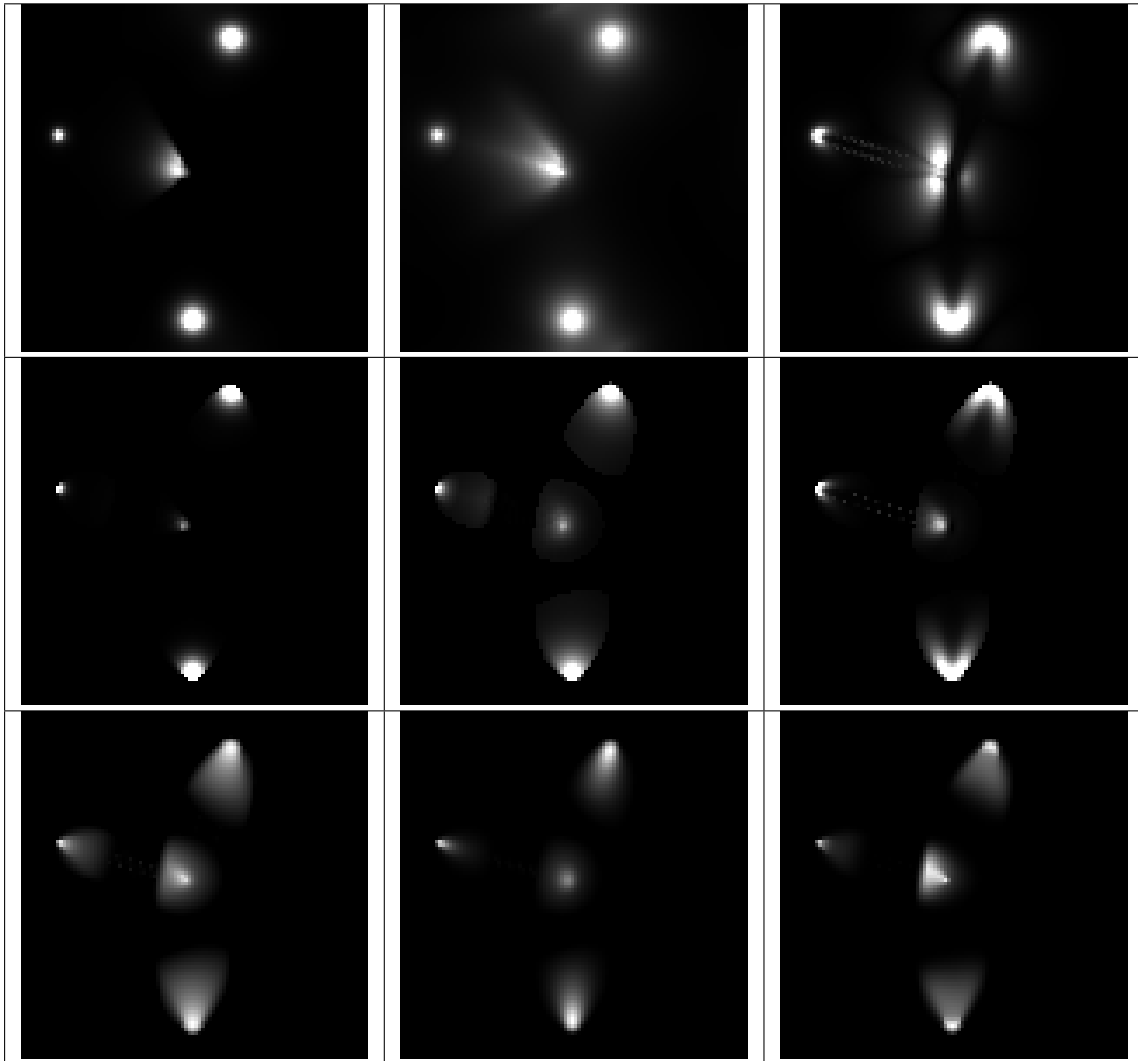


Figure 4.3: Response of corner detectors (from left to right, Harris, Shi-Tomasi, curvature of level curves in the first row), the same corner detectors restricted to areas with all Hessian eigenvalues negative (second row), and Hessian-based bifurcation detectors (from left to right, λ_1 , Determinant of Hessian, Frangi-style). Initial image is a 2D synthetic strongly asymmetric bifurcation ($\alpha = 0.4$), parabolic profile



Hessian eigenvalues negative) is applied, only the maximum associated with the bifurcation is left (second row in Figure 4.2).

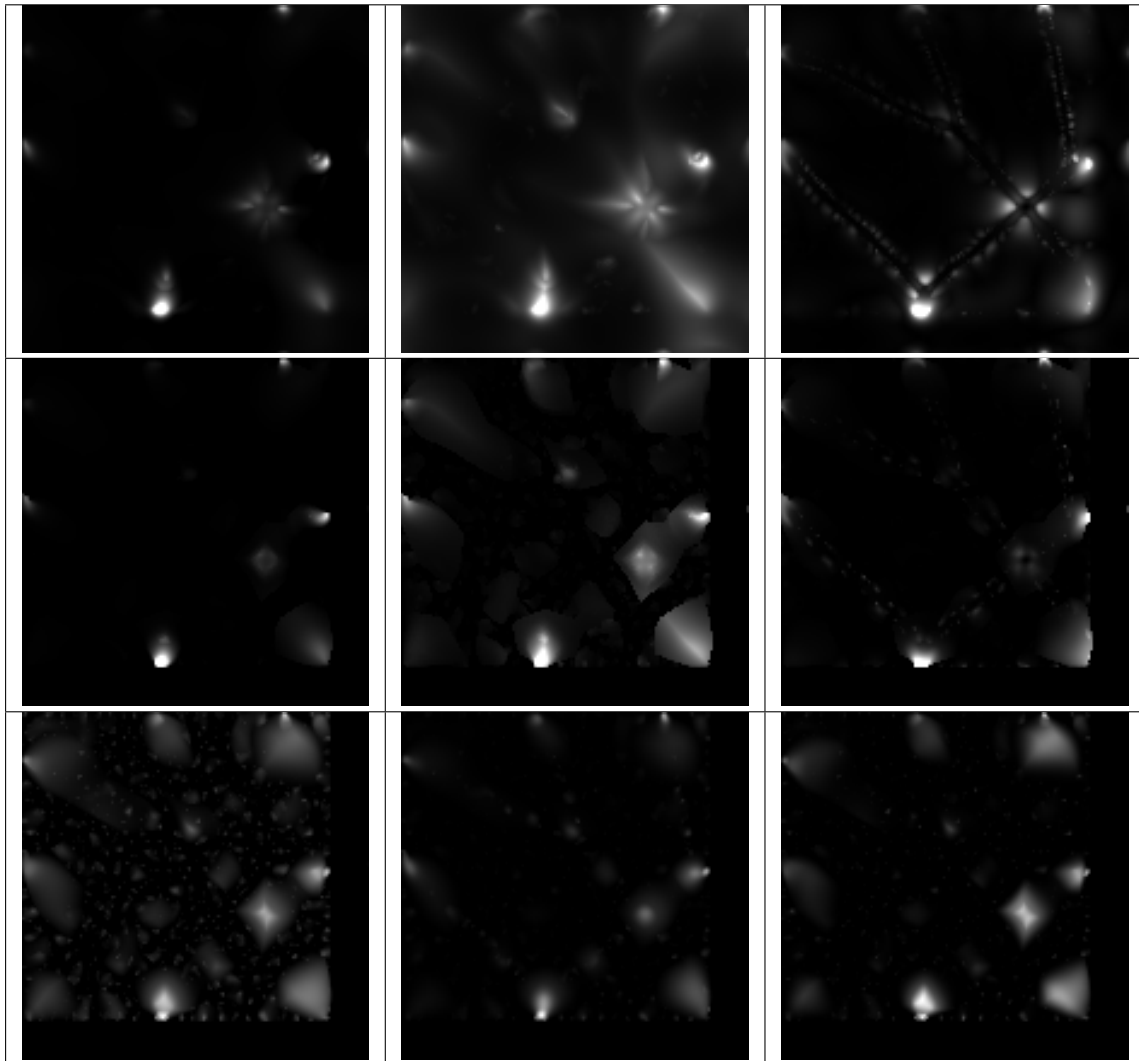
The curvature of level curves operator has a radically different behavior. One might expect that, since the location of bifurcations is marked by a local maximum, this operator would give a measurable response there (as well as at blob locations). The original operator is defined to have large response in the regions where the gradient is also large, ensuring that responses are localized on edges. We can see in Figure 4.2 that in its original form, this operator outlines *all* the corners of the bifurcation, much better than the Harris or the Shi-Tomasi operators. The responses are located outside the vessels, and when the Hessian eigenvalue condition is applied, the response of the operator is strongly diminished and there is no “central blob”

The situation is improved in the more extreme splitting ratio $\alpha = 0.4$ (corresponding to area ratio of 0.16 – Figure 4.3). With the “negative eigenvalue” filter in place, all three corner detectors give a reasonable, localized response at the bifurcation. Without the filter, the Shi-Tomasi operator gives strong responses in the angles generated by the smaller daughter vessel with the larger daughter and with the parent vessel; the Harris operator gives a similar response, but more localized around the bifurcation. The curvature of level curves outlines all three angles, but also generates a smaller local maximum on the smaller daughter vessel close to its junction with the parent vessel. This smaller local maximum is the only one remaining after the “negative eigenvalues” filter is applied.

For comparison, the last row in Figures 4.2 and 4.3 shows the responses of the Hessian-based detectors: λ_1 , Determinant of Hessian, and Frangi-style. All of these operators show a consistent, well-defined and well-localized response at the bifurcation for all bifurcation ratios of the ideal synthetic bifurcation. Among the corner detectors, only the classic detectors Harris and Shi-Tomasi have this property.

The other tests were done on clinical images. The first of these, a fragment of angiogram, is very noisy (bottom left in Figure 4.1), with only 8 levels of grey. Even along the main vascular branches there are significant intensity fluctuations. To limit the boundary effects, a border (black) was added to the image. The result of applying these operators is shown in Figure 4.4. The Harris and the Shi-Tomasi detectors highlight the major bifurcations, but are unable to distinguish the bifurcations close to the bottom and right edges from the end-of-vessel signals, with or without the negative eigenvalue filter. The crossing, however, has a very diffuse signal, with multiple local maxima (with or without the negative eigenvalue

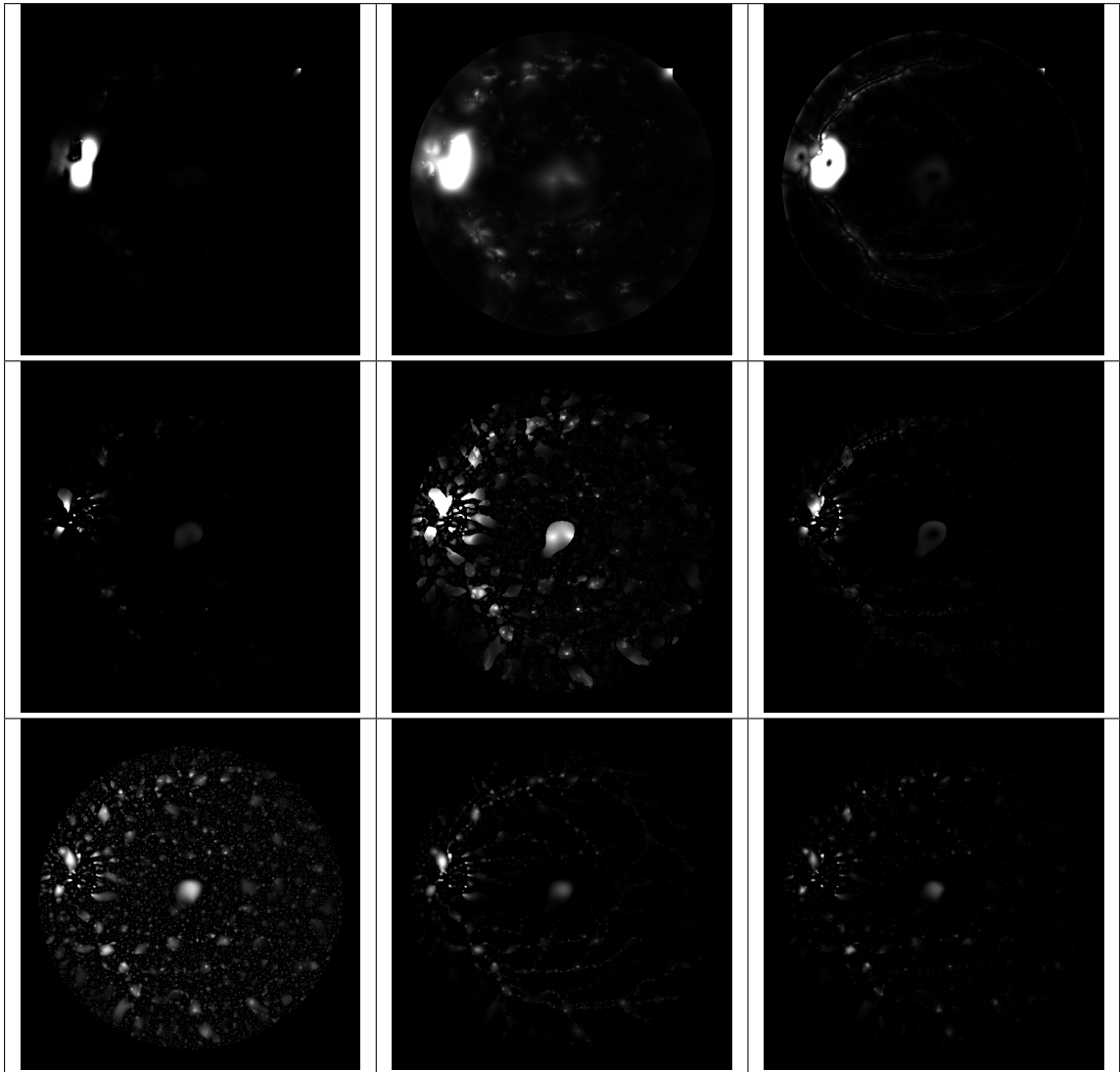
Figure 4.4: Response of corner detectors (from left to right, Harris, Shi-Tomasi, curvature of level curves in the first row), the same corner detectors restricted to areas with all Hessian eigenvalues negative (second row), and Hessian-based bifurcation detectors (from left to right, λ_1 , Determinant of Hessian, Frangi-style). Initial image is a 2D noisy angiogram



filter). The minor bifurcation (between the crossing and the bifurcation at the bottom) is detected only by the Shi-Tomasi filter. Due to the noisy edges of the vessels, the curvature of level curves operator outlines the vessels, while the scale-space approach prevents the noisy interior structure from generating spurious signals. Just as with the other corner detectors, the bifurcations close to edges are not resolved, while the crossing has a diffuse response with multiple local maxima. Even the bifurcation just above the center of the image is difficult to resolve. By contrast, all of the Hessian-based detectors correctly resolve the bifurcations from the end-of-vessel signal, and even the minor bifurcation is clearly detected. The background has a noise accumulation just below and to the left of the center (blob-like), seen in the λ_1 response, but much less in the Frangi-style response and is virtually invisible in the DoH response. The λ_1 response shows a large amount of noise compared to the other two, but this can be easily explained. For the Frangi-style response, the explanation is quite simple: the nonlinear response dampens the small amplitude responses quite efficiently, so those with amplitude below about 10% of the maximum are virtually invisible. For details, see Appendix C. The Determinant of Hessian acts in a similar manner. Since $|\lambda_2|$ is the sum of ball and stick components of the tensor, the Hessian is dominated by the square of the ball component, or $|\lambda_1|^2$, resulting in a significant reduction of the small amplitude responses of the noise. The other term of the DoH is the product of the ball and stick components, resulting in an almost *linear* transfer of the point-like response along the vessels. For this reason, the DoH response appears confined along the blood vessels. The nonlinear mapping has little influence on the presence of local maxima, although it is important for visualization; if thresholds are to be applied or the relative saliency is to be considered, the criteria can be easily adjusted to compensate the nonlinearity. Only the DoH is different, since the ball component is mapped differently on and off the vessels.

The last set of tests was done on an image from the DRIVE database (01_test), shown in Figure 4.5. The original image is color, with the blood vessels appearing darker. We used only the green channel of the image, since the red channel is saturated over most of the image and the blue channel presents a significant amount of noise. One might expect that a PCA transform would improve the contrast of the image, but in this case the results are not significantly different from simply stretching the contrast of the green channel. The contrast was reversed, so that the vessels appear brighter than the background. The changes of the algorithm to work with dark vessels are trivial, requiring only the change of localization condition from negative Hessian eigenvalues to positive. The Harris detector only shows

Figure 4.5: Response of corner detectors (from left to right, Harris, Shi-Tomasi, curvature of level curves in the first row), the same corner detectors restricted to areas with all Hessian eigenvalues negative (second row), and Hessian-based bifurcation detectors (from left to right, λ_1 , Determinant of Hessian, Frangi-style). Initial image is a retinal image from the DRIVE database. For the corner detectors, only the bottom 10% of the dynamic range is represented.



significant response in the area of the optical disk (saturated in the negative eigenvalue filter is omitted), and only a few responses along the largest vessels. The Shi-Tomasi detector is slightly better; more responses along the vessels are seen, and the negative eigenvalue filter is required to reduce the spurious responses. Even so, most of the bifurcations on the smaller vessels give no signal. The curvature of level curves operator gives only a few outlines of the main vessels (due to discretization effects and to the natural curvature of the blood vessels), and only a few responses correspond to bright local features. Thus, none of the corner detectors is useful for detection of bifurcations in retinal images. By contrast, all of the Hessian-based detectors show detectable signals at virtually all bifurcations.

This investigation showed that the corner detectors are not useful for bifurcation detection in 2D images. Even in the limited cases where they give relevant signals, they are not as well-defined as the signals from the Hessian-based detectors. Only the Harris and the Shi-Tomasi detectors can be easily generalized for processing 3D images, but their general characteristics remain the same. For these reasons, as well as their higher computation cost, the corner detectors will not be used any further.

4.4 Computation Cost

Most of the computations were made on an Intel Core i7 CPU 860 at 2.80GHz computer with 8G RAM. The code was written in MATLAB, and most of the data was obtained using the 2010a and 2010b editions; the 2010b edition is about 10–15% faster than the 2010a edition. Optimizations were made to avoid unnecessary calculations: convolutions to obtain the scale space image were done using Fourier transforms; the original image is Fourier transformed only once and stored, and the convolution kernel is calculated directly in the Fourier domain. For processing 2D images, for each scale used, the Hessian-only approach used requires computing three convolution kernels, plus three inverse Fourier transforms for the 2D case, and the eigenvalue analysis (done analytically, which involves simply solving a second-order equation). For a detailed scale analysis of a 100×100 image using 100 scales, computing time was about 0.47 sec, while computing only 20 scales took just above 0.1 sec. Larger images took longer, with 1.20 sec for a 400×360 pixel image, and 4.45 sec for a 565×584 pixel image from the DRIVE database.

Computing the structure tensor, required for the classical corner detectors, is more expensive. It requires computing two kernels and two inverse Fourier transforms (for the two

gradient components in scale-space), then three element-by-element matrix multiplications, plus three Fourier transforms, three multiplications and three inverse Fourier transforms for averaging the structure tensor. The total is 8 element-by-element matrix multiplications and 8 Fourier transforms for each scale computed, compared to 3 each for the Hessian-only method.

The curvature-of-level-curves approach requires computing all five first and second order derivatives, for a total of 5 element-by-element matrix multiplications and 5 Fourier transforms for each scale computed.

Similarly, for processing 3D images, the Hessian-only approach requires 6 multiplications and 6 FFTs, while the structure tensor approach requires a total of 15 multiplications and 15 FFTs (3 multiplications and 3 FFTs for the gradient components, 6 multiplications for computing tensor components, followed by 6 FFTs, 6 multiplications and 6 inverse FFTs for the final averaging). Typical running times (for the Hessian-only approach) are about 15.6 sec for an $100 \times 100 \times 100$ image computed at 25 scales and about 75.5 sec for an $170 \times 170 \times 170$ image computed at 25 scales.

Clearly, the Hessian-only approach is not only better than corner detector approaches (as we have shown in this Chapter), but is also faster, requiring less than half the computing time required by the structure tensor based approach.

4.5 Conclusion

The detection method presented at the beginning of this Section remains valid, but it depends critically on the choice of "local feature detector". Clearly, corner detectors are not suitable for use. Although each of them can generate usable responses in certain situations, none of them can be used in *all* the situations, or even in all simple situations. In 2D, all the Hessian-based detectors are usable, and their responses are equivalent. Even the Frangi-style detector, with its complicated nonlinear response, is dominated by a nonlinear monotonic rescaling of λ_1 . In 3D, however, the nonlinear response of the Frangi-style detectors is even more complicated, resulting in the possibility of multiple local maxima around the bifurcation. Even though multiple local maxima do not appear in all situations, the fact that they occur even in ideal situations and their presence and/or position depend on the orientation of the structure under investigation makes them too unreliable for practical use. The other Hessian-based detectors ($|\lambda_1|$, Determinant of Hessian, $|\lambda_1|(|\lambda_3| - |\lambda_2|)$)

give similar results, although the new combination $|\lambda_1|(|\lambda_3| - |\lambda_2|)$ (a combination of ball and stick tensor components, corresponding to ball and plate image structures) has the advantage of reduced response at blobs due to the additional factor. This new operator has clear advantages for bifurcation detection in 3D images; unfortunately, it has no equivalent for 2D images, where only ball and stick (of linear) structures can occur.

Chapter 5

Results

To quantitatively evaluate the performance of the algorithm, we used a set of synthetic images. These can be generated in large quantities, and the location of the actual bifurcation is known precisely without the need for segmentation by human subjects.

The first set of tests was done with fractal trees. Fractal trees are among the simplest recursive shapes; the drawing algorithm simply draws the current branch, then calls itself to draw two new branches at the end until the recursion level is reached. The fractal recursion level of the synthetic trees was 5, so each tree had 31 bifurcations; in addition, several of the trees had crossings of the branches, which were identified manually. In total, the 20 tests had 623 points of crossing and bifurcation. Only 5 of those were not properly identified, due to their proximity to other structures (branches and other bifurcations). In these cases, the local “inner scale” and “outer scale” were too close to each other or even overlapping. At lower scales, there were spurious local maxima due to pixelation; however, these vanished when the scale for locating maxima was automatically picked at the scale of maximum response.

A typical result is shown in Figure 5.1. Here we show the results of applying a bifurcation filter (λ_1 , in this case; the results are quite similar using the other 2D bifurcation detectors – Determinant of Hessian and a Frangi-style operator). Superimposed on these is the contour of the tree, obtained by applying the Canny edge detector to the original image. These results are similar to responses presented earlier, when we analyzed the responses of the various 2D detectors. In addition, we can easily see the localization of the maxima, very close to the center of each bifurcation, as well as at the end of the vessels. All of these points have codimension 1, the same as for linear structures, in spite of being localized structures.

Using only the presented criteria, there is no way to distinguish between bifurcations and end-of-vessels. However, in practical images, there are no end-of-vessels; they only occur at the edge of the imaging area. Signals occurring at the edges of the image must be eliminated anyway, since these areas are subject to boundary effects when converting to scale-space.

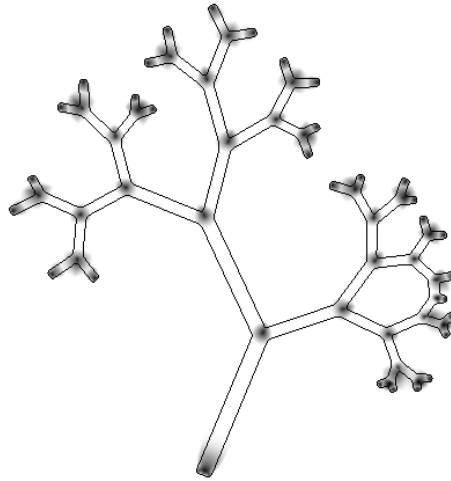


Figure 5.1: Bifurcation detection results on a fractal tree. Bifurcation signal is superimposed on the contour of the tree obtained with the Canny edge detector applied to the original image.

Adding a moderate amount of noise increases significantly the number of local maxima, as each bright noise pixel generates its own response. At low noise levels, however, it is unlikely that noisy pixels will be close enough to each other to influence each other and are easily eliminated by the scale limit and the codimension criterion. The result is that bifurcation locations are still reliably detected, as illustrated in Figure 5.2. Here, the synthetic tree images were modified by adding noise: half of the pixels (randomly selected) had noise added, uniformly distributed in the range 0-255. This is only one of the possible noise distributions; changing noise type does not have a significant influence on detection. However, noise type will influence the level at which bifurcation detection is affected.

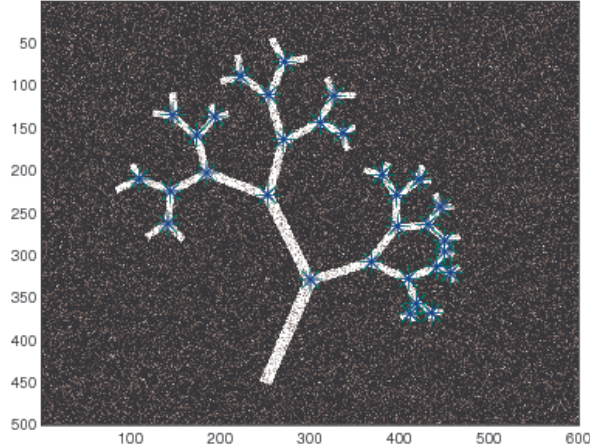


Figure 5.2: Bifurcation detection on a fractal tree, with half of the points having noise uniformly distributed from 0 to 255.

5.1 Statistics of 2D Bifurcation Detection

For a more precise characterization of the noise sensitivity, we generated synthetic 2D bifurcations, with main branch radii r_0 from 1 to 7 pixels (in steps of 0.5) and bifurcation ratios α_R (ratios of the daughter vessels) from 0.1 to 1 (in steps of 0.05). These ranges are rather extreme; low values for r_0 and α_R lead to heavy pixelation and even interruptions of the daughter vessel(s). Where global statistics were required, we used $r_0 \geq 2$ (since real vessels do not present interruptions due to pixelation) and $\alpha_0 \geq 0.3$, (corresponding to the smallest bifurcation area ratio of 0.1 reported experimentally in [49]). For example, the retinal images from the DRIVE database present a wide range of vessel diameters, but none of the identifiable vessels is smaller than 2–3 pixels. To test noise robustness, we added Gaussian noise (with standard deviation between 0 and 1) and salt-and-pepper noise with various densities. The images were generated with different orientations of the main branch, each with a different instance of noise, with a total of 180 runs for each set of noise type and level, r_0 , α_R . Bifurcation angles and branch radii were designed to mimic those of real bifurcations as described in [14, 49], so each of the bifurcation angles was allowed a random variation (Gaussian) around the theoretical value (about 90°) with a standard deviation

Figure 5.3: Initial images used for 2D quantitative testing, in the absence of noise. Bifurcation angles have Gaussian variability, to mimic real bifurcations.

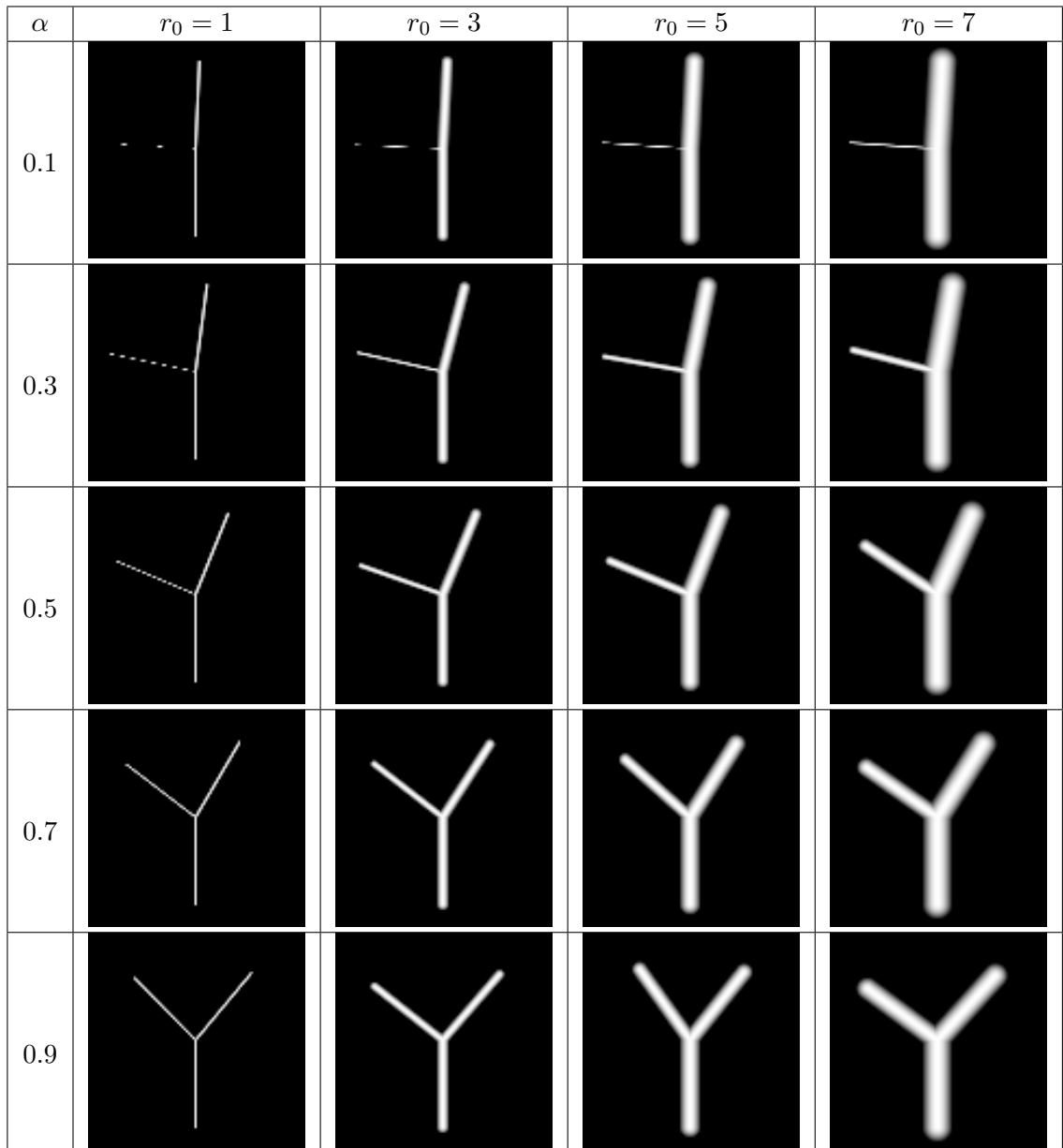


Figure 5.4: Initial images used for 2D quantitative testing, with low Gaussian noise (mean 0, standard deviation 0.1). Bifurcation angles have Gaussian variability, to mimic real bifurcations.

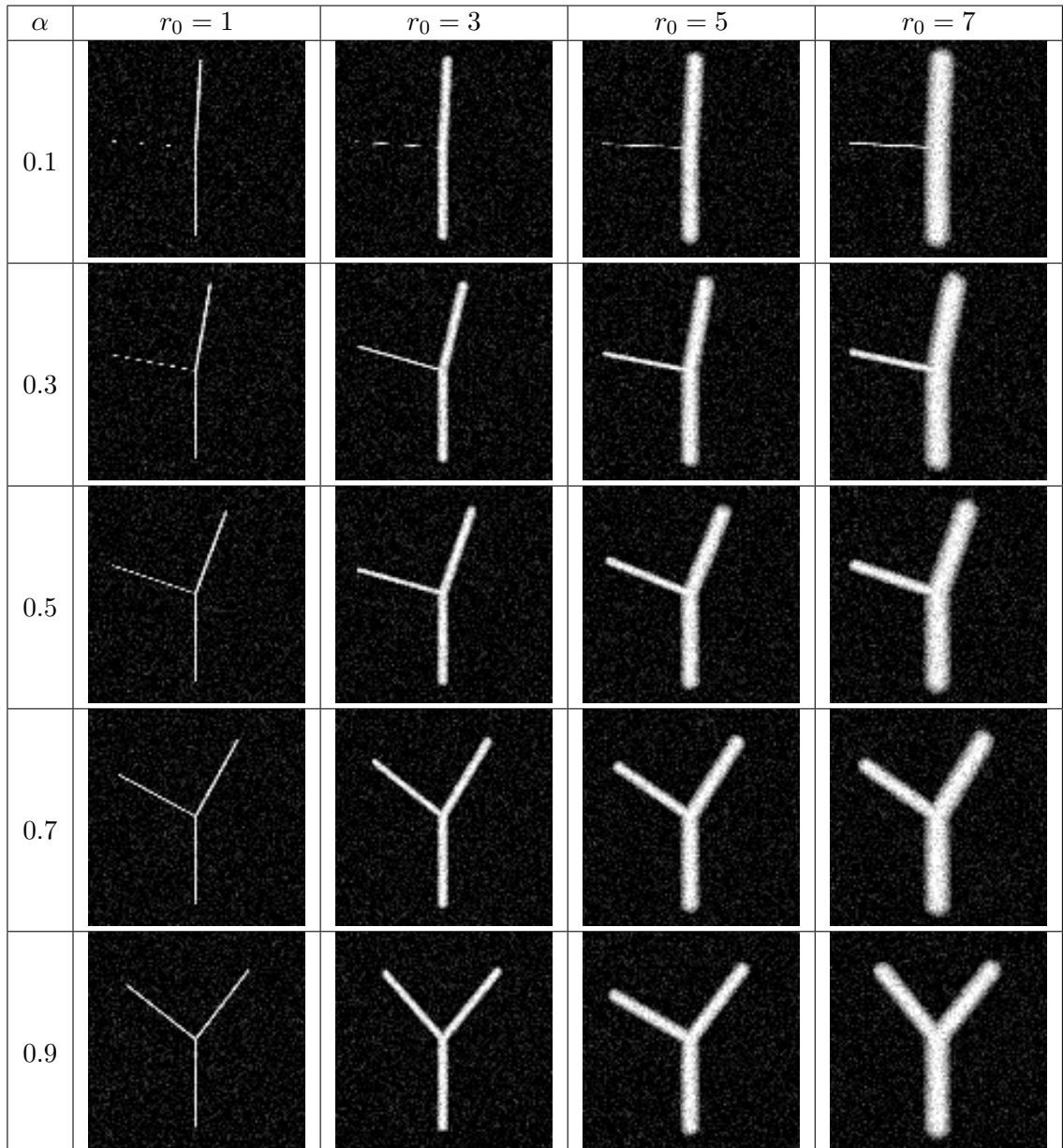


Figure 5.5: Initial images used for 2D quantitative testing, with high Gaussian noise (mean 0, standard deviation 0.4). Bifurcation angles have Gaussian variability, to mimic real bifurcations.

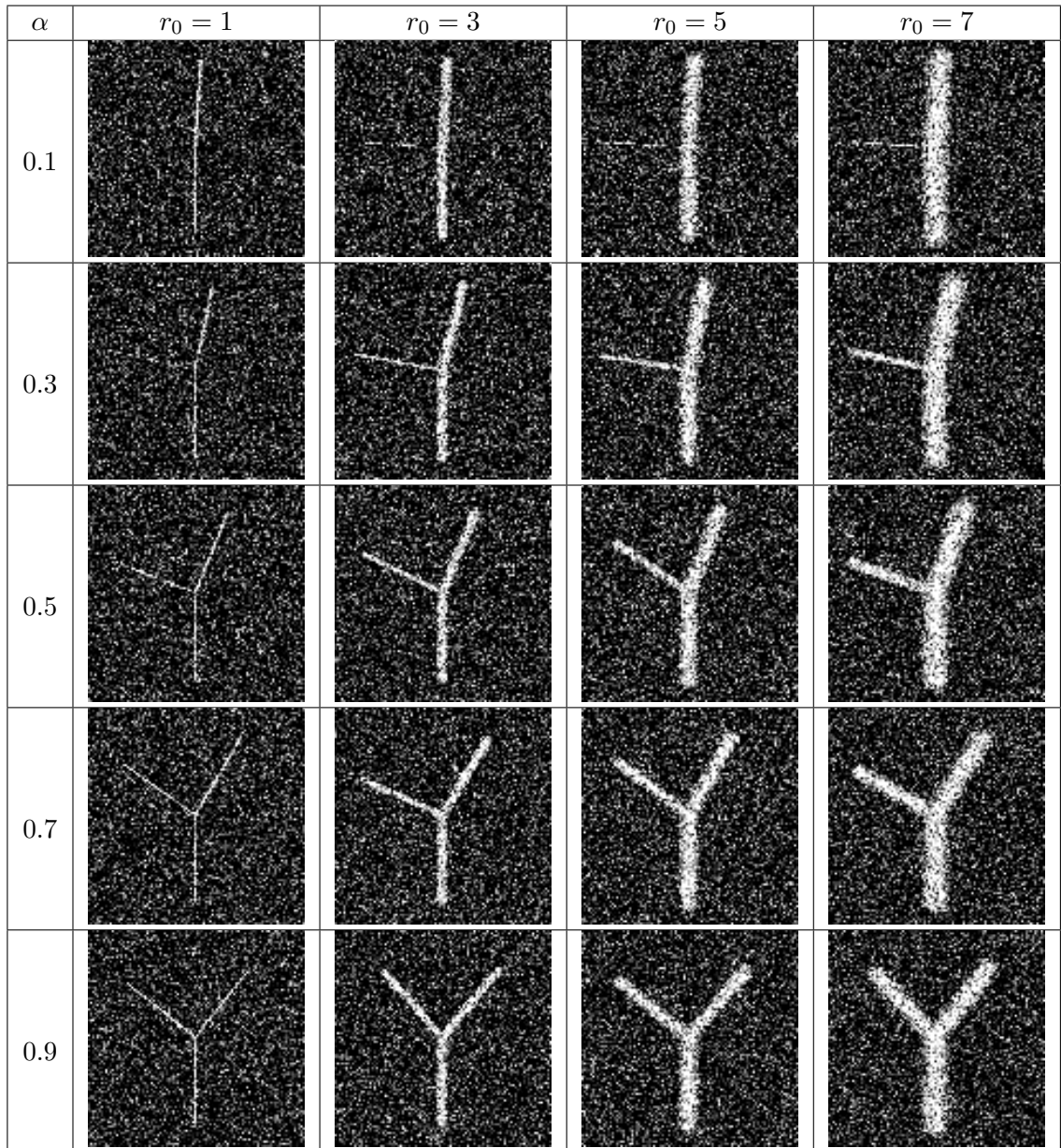


Figure 5.6: Initial images used for 2D quantitative testing, with low Salt&Pepper noise (10%). Bifurcation angles have Gaussian variability, to mimic real bifurcations.

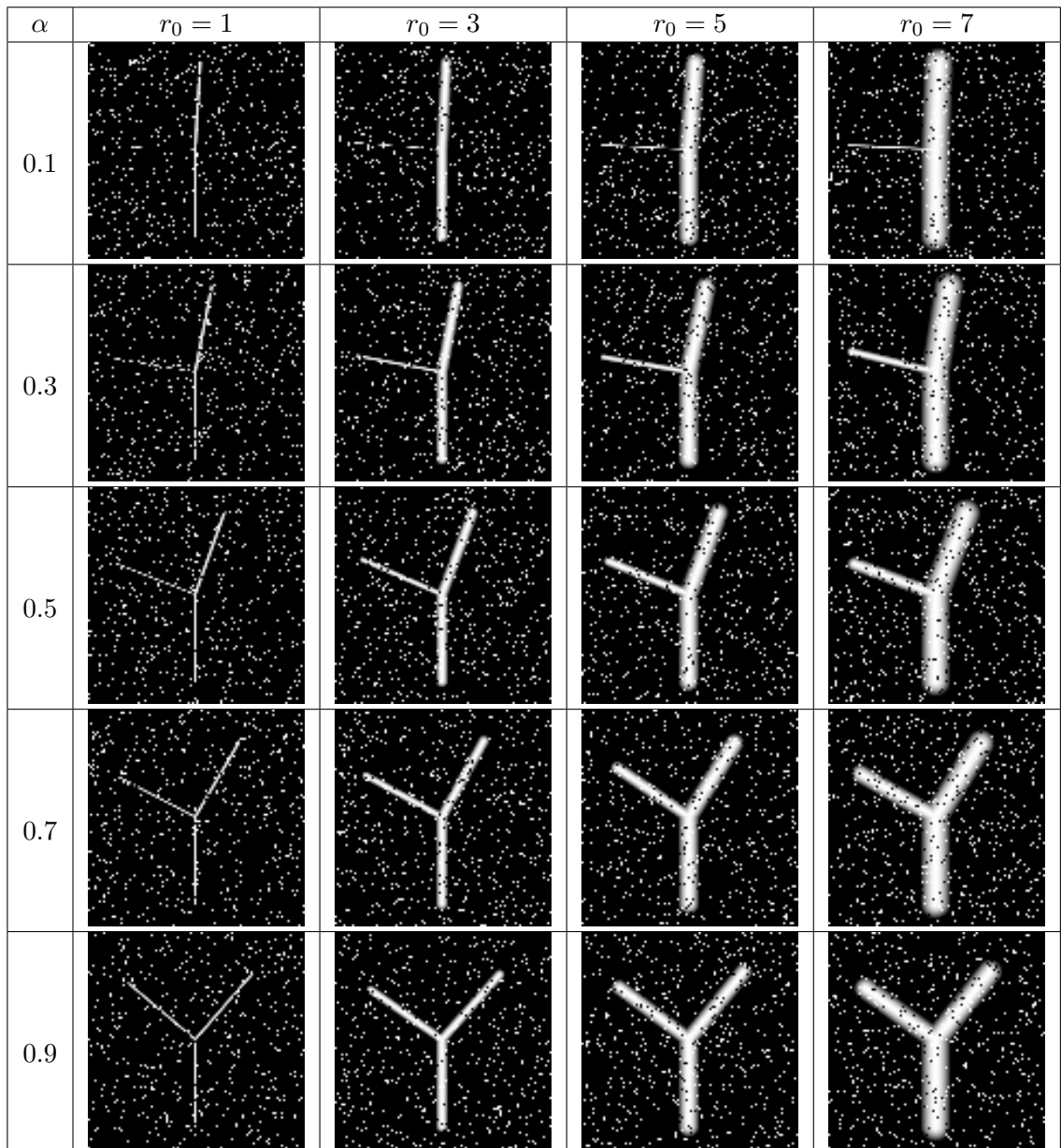
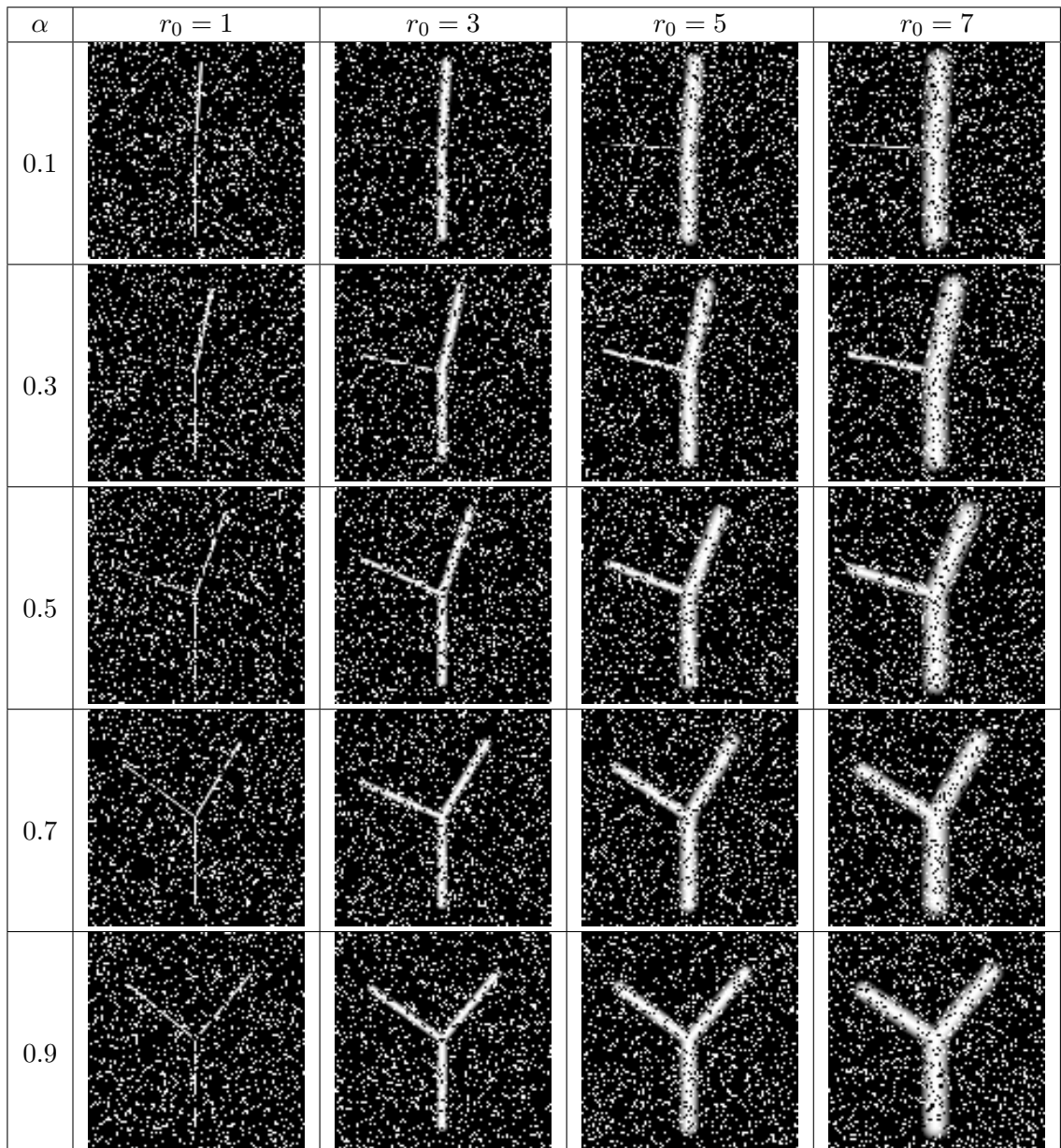


Figure 5.7: Initial images used for 2D quantitative testing, with low Salt&Pepper noise (25%). Bifurcation angles have Gaussian variability, to mimic real bifurcations.



tuned to generate the maximum range 60° – 120° reported in clinical data. A mask with radius of 40 pixels was placed around the bifurcation, to isolate it and to avoid boundary artifacts. To limit spurious data, we imposed a limit on the saliency for the bifurcationness response of 10^{-4} of the maximum bifurcation response, although a limit of 10^{-2} might be sufficient. Note that the images used in this test are 100×100 pixels. Also, we considered a bifurcation “detected” if a local maximum with sufficient saliency is detected within $r_0 + 1$ pixels from the true bifurcation location.

The results of the simulations are presented in Figures 5.8 and 5.9. In the absence of noise (a subset of the initial images is presented in Figure 5.3, virtually all bifurcations were detected (with the exception of the extreme cases mentioned earlier). Figure 5.3 clearly shows that the cases with low detection rate ($r_0 \simeq 1$ and/or $\alpha_R \simeq 0.1$) are extreme, with heavy pixelation and even interruptions on the smaller daughter vessel. The effect of these pixelations/interruptions also strongly depends on the orientation of the parent vessel. For more reasonable parameters ($r_0 \geq 2$ and $\alpha_R \geq 0.3$), the bifurcation is almost always reliably detected. In the presence of noise, however, the probability of detection decreased. Low levels of Gaussian noise (with mean 0 and standard deviation 0.1, for example, sample inputs shown in Figure 5.4) do not influence much the detectability of bifurcations. The 95% detectability limit for this noise level (the dash-dot curve in Figure 5.8) is almost identical to the solid curve, corresponding to the lack of any noise. The highest noise level for which we achieved 95% detection of true positives in the presence of Gaussian noise was standard deviation of 0.40; sample input images for this case are shown in Figure 5.5.

The salt-and-pepper is much more difficult to counteract, and its effects are much more deleterious. A level of 10% displaces significantly the 95% detectability threshold (see Figure 5.9), and has roughly the same effect as the Gaussian noise with a standard deviation of 0.25. The overall detectability drops to just above 95% even in the most favorable circumstances (large r_0 , symmetric bifurcation) at a salt-and-pepper noise level of 25% and to 90% for 35% noise density. We have to remember that a 25% level for salt-and-pepper noise means that only about 3/4 of the pixels give useful information, and one pixel in four gives spurious information. There are several possible explanations for this decrease. It is possible that the signal for the bifurcation itself might still be present, but with a value much lower than the threshold used. Another possibility is the “maximum stealing”. At high noise levels, it is possible that there is a noisy pixel in the immediate vicinity of the bifurcation, so detection of scale space maxima gives the noise pixel instead; in the maxima

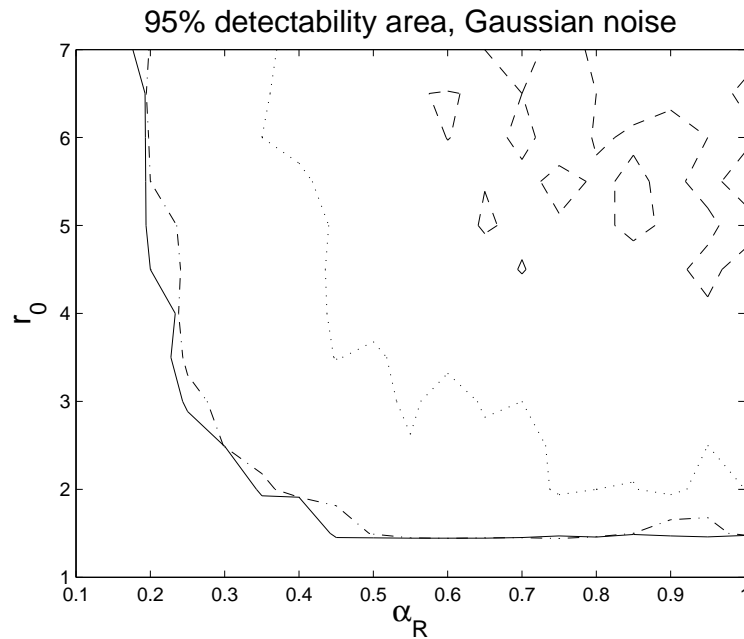


Figure 5.8: Bifurcations were detected with a probability exceeding 95% in the area above the curves. Gaussian noise with standard deviation 0, 0.1, 0.25, 0.40

filtering steps (scale threshold and codimension) this local maximum is eliminated. Future research will center on using more neighbourhood information to mitigate noise influence.

An important feature is the codimension selection filter. After applying any of the bifurcation filters, there are up to 200 local maxima in the resulting map; most of these are eliminated by the codimension filter and the scale selection. For example, in the case of salt-and-pepper noise (with a level of 25%), there maximum number of false positives is 3.31 per image (or true bifurcation, since there is exactly one true bifurcation per image) if the scale threshold is set to 1, and decreases to 0.71 if the scale threshold is increased to 1.5 and to 0.2 for scale threshold of 2. For Gaussian noise, the maximum values are 1.8, 0.33, and 0.1, for all noise levels (standard deviation up to 1). The reason for such a high number of false positives is that noise pixels may be located on the vascular branches, and the codimension of these pixels is not estimated correctly. Bright noise pixels situated on vessels are seen as local features by the detector, but may “borrow” from the codimension of the vessel, thus generating false positives. The assumption in estimating the codimension is that there is no background, a false assumption in the case of a bright pixel on a vascular

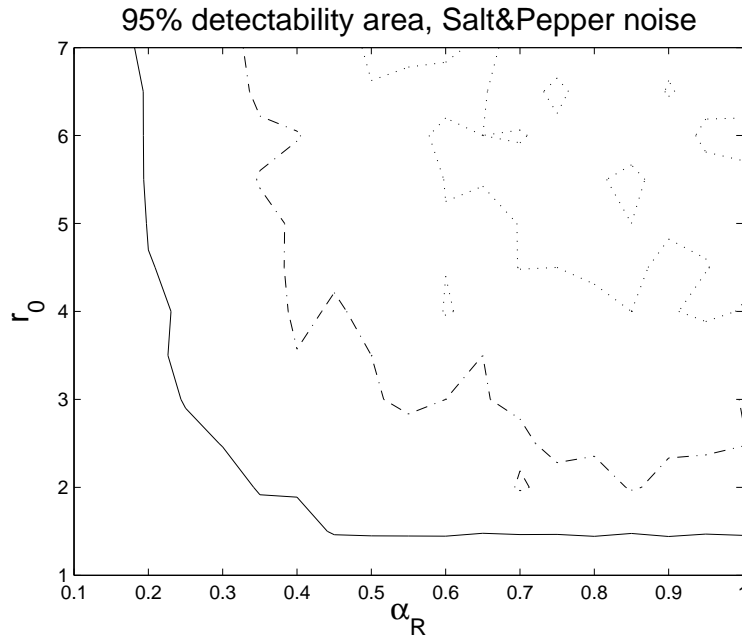


Figure 5.9: Bifurcations were detected with a probability exceeding 95% in the area above the curves. Salt and Pepper noise with density 0, 0.1, 0.25.

branch. In this case it would be more reliable to estimate the codimension using the scale-space derivatives of the Laplacean, but this method is less reliable for other purposes. The concept of codimension was introduced mainly to distinguish bifurcations and crossings from blobs, all being local features detected by the local maxima of scale-space operators; in all cases where blobs were deliberately introduced in the images, they were correctly identified.

Similar statistics for 3D images are more difficult to obtain; the extra dimension increases significantly the computing time (the convolutions for scale-space transform are made on 100^3 volumes instead of 100^2 images). For example, an isolated 2D bifurcation takes in the range of 0.25 – 0.5 sec to process using Matlab 2010b on an i7 computer with 8G of RAM, while a 3D image takes about 20 sec to process in the same setup. However, for the cases we checked, we found no significant differences compared in the detectability rate when compared with the 2D case.

5.2 Localization Errors

A key aspect of detection is the accuracy of localization. We already mentioned that we used proximity to the true bifurcation as a detection criterion. Here we look in detail at the localization of bifurcations as detected by our filter.

First, we note that there is no significant difference between the position of the detected bifurcation in the absence of noise and in the presence of noise, regardless the noise level, as long as the bifurcation is detected. For the purpose of this investigation, the restriction that the detected bifurcation is detected within a certain distance from the true location was relaxed.

The localization errors are summarized in Figure 5.10. The graph shows the absolute distance (in pixels) between the detected location and the true location (set by the program generating the initial image). We can see that all detected locations are within a few pixels from the true location. It is expected that if the initial image is scaled up or down by a certain factor, all the spatial values will be scaled by the same factor. This includes the response map of the detectors, therefore the bifurcation localization error. If we represent the localization error normalized to the radius of the parent vessel, it will depend only on the bifurcation angles. A more detailed analysis of the localization error is difficult to make and does not bring any new useful information. The distribution of normalized errors is presented in Figure 5.11. One can see that this error distribution is very different from the graph of unnormalized errors. Virtually all errors are localized within one parent vessel radius from the true bifurcation location. The distribution shows a very sharp drop for localization errors above one radius. It is likely that the cases where the relative error is above 1 come from bifurcations where the radius of the parent vessel was at the low end of the range.

A classic result of the probability theory is the transformation from one random variable to another. This result is presented in many books on statistics and random numbers, for example Section 7.2 in *Numerical Recipes in C* [40]. In short, if x_1, x_2, \dots , are random variables with a *joint* probability distribution $p(x_1, x_2, \dots)dx_1dx_2 \dots$, and y_1, y_2, \dots are all functions of all the x 's (same number of y 's as the x 's), then the joint probability distribution of the y 's is

$$p(y_1, y_2, \dots)dy_1dy_2 \dots = p(x_1, x_2, \dots) \left| \frac{\partial(x_1, x_2, \dots)}{\partial(y_1, y_2, \dots)} \right| dy_1dy_2 \dots \quad (5.1)$$

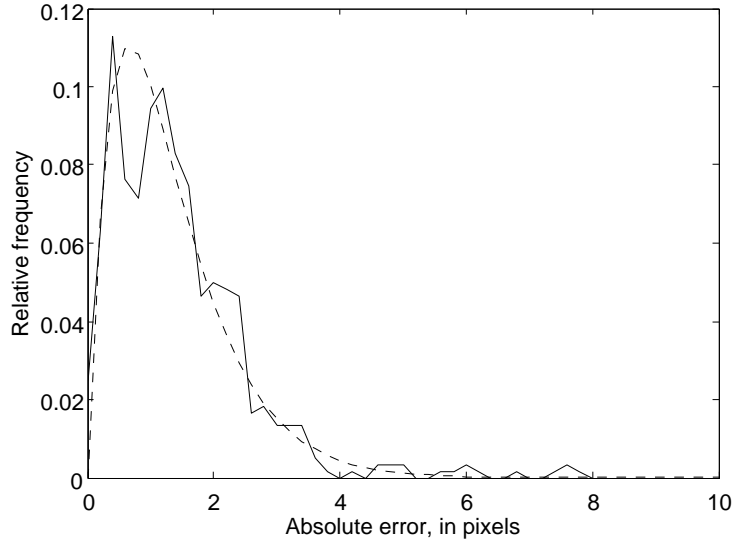
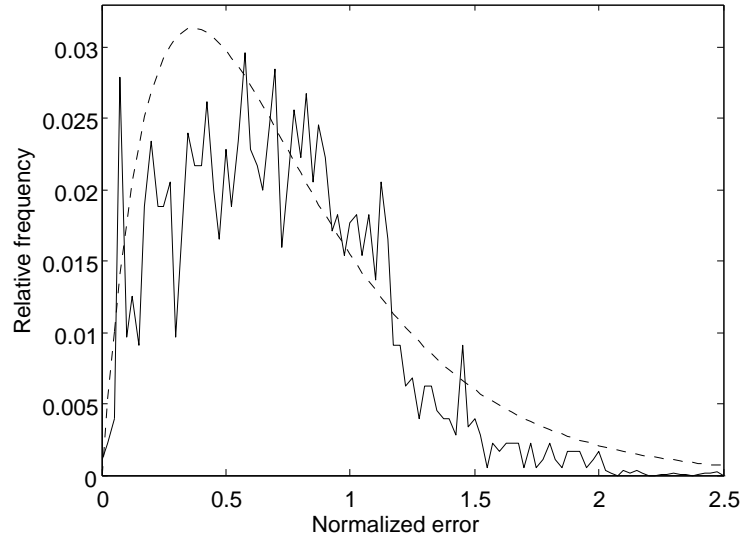


Figure 5.10: Distribution of absolute location errors (continuous line). Dashed line curves are the best fit with $re^{-r^2/a}$.

where $|\partial(x, y)/\partial(r, \theta)|$ is the Jacobian determinant of the x 's with respect to the y 's (or the reciprocal Jacobian determinant of the y 's with respect to the x 's). For a transform between rectangular and polar coordinates ($x = r \cos \theta$, $y = r \sin \theta$), we immediately get

$$\left| \frac{\partial(x, y)}{\partial(r, \theta)} \right| = \begin{vmatrix} \cos \theta & -r \cos \theta \\ \sin \theta & r \cos \theta \end{vmatrix} = r \cos^2 \theta + r \sin^2 \theta = r$$

If the detected bifurcation is randomly distributed around the true location, with a Gaussian probability distribution function $Ae^{-(x^2+y^2)/(2v^2)}$, then the distance between the two locations has a probability distribution function $Are^{-(r^2)/(2v^2)}$. For this reason, we fitted the error distribution graphs with this function (the dotted line in Figures 5.10 and 5.11). While the absolute location error seems to be reasonably approximated by this function, the graph of normalized errors appears skewed towards larger errors. In fact, the error appears to have a uniform distribution until it reaches just above 1, with a significant drop for normalized errors larger than 1. This distribution is a reasonably explained if we look at the sample responses in Table 4.2.1 on page 40. The bifurcation is detected closest to the true location in the case of a symmetric bifurcation, with the bifurcation angles as large as possible. Once the bifurcation becomes asymmetric, the detected point moves away from



(a)

Figure 5.11: Distribution of location errors (continuous line), normalized to the radius of the parent vessel. Dashed line curves are the best fit with $re^{-r^2/a}$.

the true location, towards the smaller daughter vessel. In the most extreme case, with a very low bifurcation ratio, the larger daughter vessel has almost the same diameter as the parent vessel and is almost in the same direction. In this case, the bifurcation is detected on the edge of the parent vessel, at the point of contact with the smaller vessel.

The detected location, however, appears *always* displaced in a direction approximately along the bisector of the angle formed by the two daughter vessels. This appears to be a consequence of the merging of maxima with increasing scale, as illustrated in Figure 2.1 (page 14). An illustration of this displacement is shown in Figure 5.12. This figure shows the curve levels of filter response intensity (λ_1 , in this case) on the symmetry axis of the bifurcation for a perfectly symmetric bifurcation ($\alpha_R = 1$). Obviously, this is the same as the axis of the parent vessel. The true center of bifurcation is placed at pixel value 50, with the parent vessel being at pixel values less than 50. The location of the spatial maximum moves away from the true location approximately linear with scale. Therefore, by evaluating the local bifurcation maximum at two different scales it is possible to improve the localization of the bifurcation. In the particular geometry used for Figure 5.12 — symmetric bifurcation

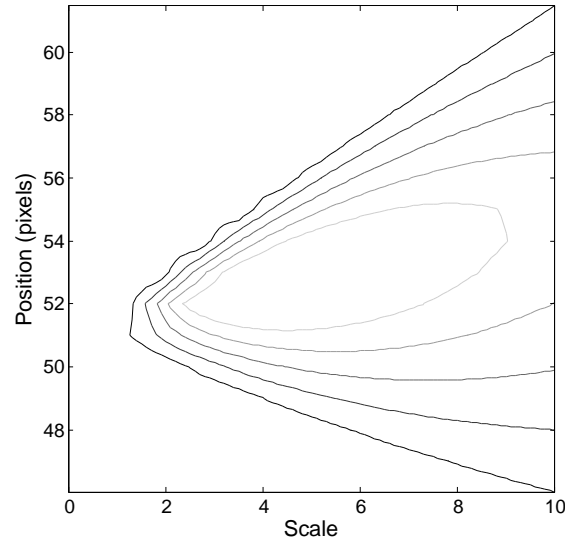


Figure 5.12: Displacement of the detected position of a symmetric bifurcation with scale with $r_0 = 5$, the maximum response occurs at pixel 53 (instead of 50), and at scale 5. Linear extrapolation of position indicates a “scale 0” location on pixel 51 — significantly closer to the true location, but still not exact. The improvement in position is in this case only two pixels. For more asymmetric bifurcations, where the bifurcation is detected on the wall of the parent vessel, the displacement with scale is smaller. For this reason, this extrapolation was not implemented.

5.3 Results on Clinical Data

The algorithm was tested on clinical data as well. Only basic preprocessing was applied to the images – background removal (by subtracting a version of the image blurred by a wide Gaussian) and contrast stretching. Some tests on 2D angiograms were presented earlier, when we investigated the reliability of various local feature detectors. Here we present some more quantitative results on 2D images – retinal images, which are typically difficult to segment automatically. We used 5 images, cropped from retinal angiograms, enhanced with fluorescein. The original images had nonuniform background (approximated by a very large scale version of the image and subtracted). Such an example is presented in Figure 5.13.

All the detected maxima were inside the vessels. Out of the 421 bifurcations present in the images, 403 were detected. A visual inspection of the bifurcations which were not detected showed that they are difficult cases, with one of the vessels coming out of the bifurcation having intensity close to the remaining background noise. 205 false positive were detected as well in these images, due to variations in vessel thickness and noise clusters. The images also contained two blobs, correctly identified by the codimensionality criterion.

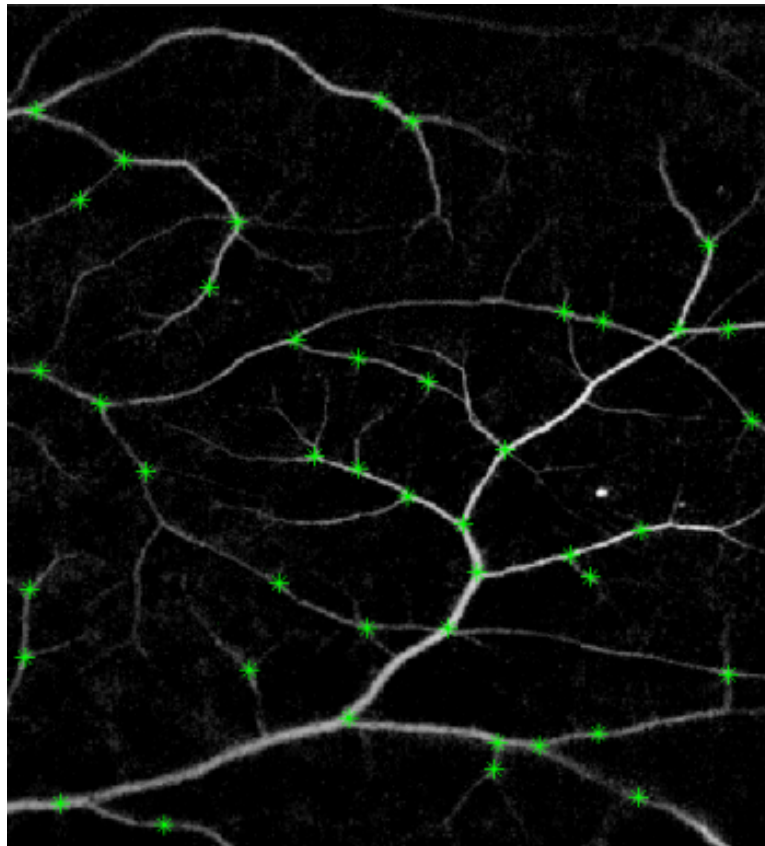


Figure 5.13: Results of applying the bifurcation detection to a retinal image. Green stars mark the position of detected maxima, corresponding to potential bifurcations.

Even more difficult to process are the non-enhanced retinal images such as those from the DRIVE database. These images have a low contrast, and the highest intensity of the vessels in some areas is lower than the background intensity in other areas. An added complication is reflection of light on vascular walls. This results in a “double humped”

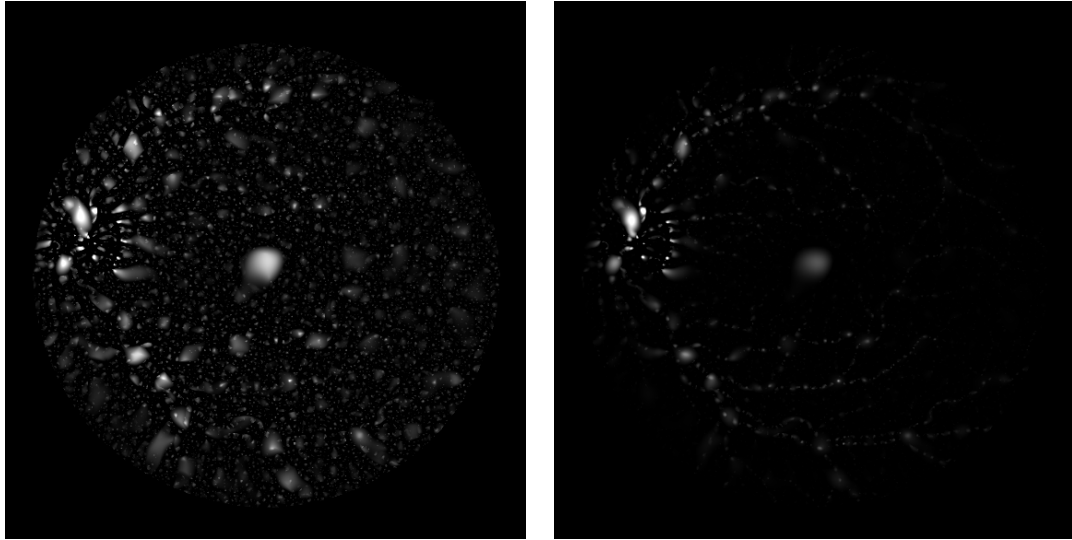


Figure 5.14: DRIVE retinal image processed for bifurcation detection with the λ_1 operator (left) and with DoH (right)

intensity profile across the vessel in some areas, while in other areas the vessels have the regular single-humped profile. Most vessel detection algorithms are unable to identify this situation, and will instead detect two vessels. While the algorithm still needs tuning for use with unenhanced retinal images, the preliminary results are encouraging, with virtually all bifurcations marked by a local sharp maximum in the detector response. Many issues are still unsolved at this moment. For example, the noise points generated by the detector appear to be in much larger number than the actual bifurcations. The DoH detector appears better for reducing noise pixels outside the vessels, but there are still many remaining on the vessels. An additional problem (but a localized one) is the strong bifurcation-type signal generated at the points where blood vessels (large, since they just entered the eye) are crossing the optical disk (a relatively high contrast feature, thus generating a strong signal).

5.4 Results in 3D

The first test on “real life” 3D data was done on a vascular phantom from Victor Luboz. This phantom, shown in Figure 5.15, consists in several fibers embedded in a block. In the

original volumetric data, the embedding block is very distinct; the fibers, however, have a stronger signal, so they can be resolved. The original image also has several elements outside the block, as well as weaker signals from the supports. These parts do not present any interest and were clipped off. The elements we are searching in this image are eight bifurcations and three crossings. The algorithm detected all bifurcations, as well as two of the crossings; the fibers in the third crossing were too far apart to give a significant signal in the detector. Figure 5.16 shows the results of the detection. The fibers are shown in green (generated using the `isosurface()` function of Matlab applied directly to the original data), while the detected points are represented by red balls; the size of these balls is an indicator of the saliency of the signal at each location. Beside the true positives, only one additional point was detected. This false positive is located at the entry point of one of the fibers in the embedding block. It is quite obvious that the saliency of this point is significantly smaller than that of the true positives. Several other local maxima of the local feature detector were eliminated outright due to their low saliency. Other signals were due to discretization errors, and were eliminated directly because the scale of the largest signal was too small (1 or below). The local feature detector also generated expected signals at the corners of the block, but these were eliminated by the codimension criterion.

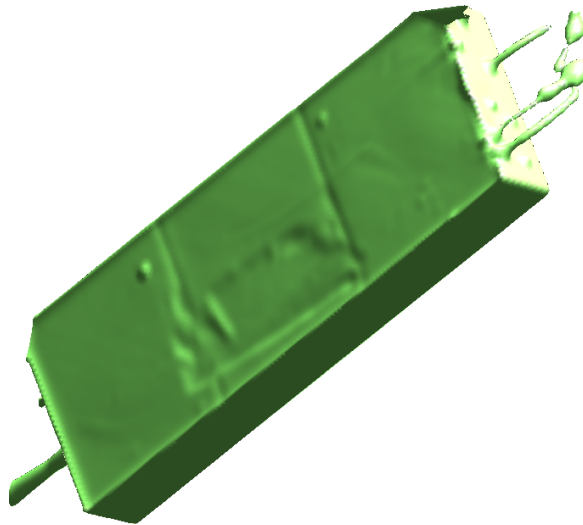


Figure 5.15: The original Luboz phantom, embedded in a block

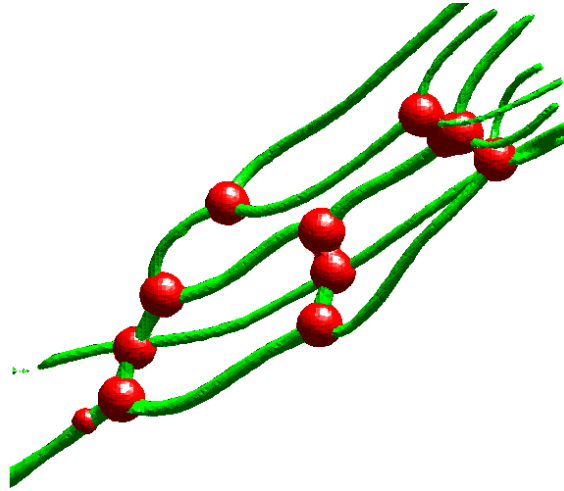


Figure 5.16: Bifurcations and crossings detected (red balls) on the Luboz vascular phantom. Vessels/fibers are represented in green.

For the local 3D feature detector, we used all three candidates: λ_1 , DoH, and $|\lambda_1|(|\lambda_3| - |\lambda_2|)$. All of them identified the features of interest. They have minor differences in localization (around at most 1-2 pixels). More significant is the difference in saliency — for example, $|\lambda_1|(|\lambda_3| - |\lambda_2|)$ reduces the response of blobs compared to bifurcations and crossings, while the other detectors do not. The first attempt to implement a bifurcationness filter (Eq. 4.1), while intuitively sound, did not perform well. We already mentioned its possible failure due to the presence of the gradient penalty, while in 3D images, even in the most favorable circumstances, the local “increase” in intensity (actually, a slower initial decrease) is only 3 to 10 percent compared to the intensity on the parent vessel. When applied to synthetically generated vascular trees (from Vascusynth) less than half of the bifurcations present were detected. With the much simpler local feature detectors, the results improved considerably; almost all bifurcations were detected. Some of the bifurcations were too close to each other to be correctly detected, or the asymmetry of the bifurcation was too large (larger than the strongest asymmetry reported in clinical data). A full Vascusynth generated tree is very complex, with a large number of vessels and bifurcations, even in a typical volume of 200^3 pixels. A sample of such a tree is presented in Figure 5.17.

5.5 Limitations

We have already mentioned that the algorithm can not distinguish between crossings and bifurcations, and between structures too close to each other, especially when one of the structure is much stronger than the other. In this case, the signal from the strong structure might simply drown the signal from the weak structure. If the structures have comparable strength, then their signals might merge before the scale-space maximum is reached. It is possible that a more detailed eigenvalue analysis, taking into account groups of pixels, might alleviate this problem. Another problem is the case of weak vessels, with intensity close to the background. In these situations, the bifurcation might not be detected at all. Two such situations are presented in Figure 5.18.

In Figure 5.18(a), a vessel with weak signal is in the presence of three strong vessels. Its intensity is very close to that of the background noise, especially from the bifurcation where it originates to the crossing with the horizontal vessel. This crossing is detected, but its originating bifurcation is not. Figure 5.18(b) is another difficult case. Although the diameters of the vessels are rather large, the larger daughter vessel has a very low intensity close to the bifurcation, barely above the noise level, bifurcation is not detected,

Due to the clutter of blood vessels, retinal images can be very challenging. Figure 5.19 shows one difficult area (extracted from file 01_test in the DRIVE database), with an overlap of a bifurcation and a crossing. Our algorithm generates a single signal for this structure. At a short distance above it, there is another structure on which even experts do not quite agree: one expert considers it a trifurcation, while the second expert considers it as a quick succession of two bifurcations. Due to its close proximity to the other structure and the relative weakness of the small vessels, the scale-space operators are unable to resolve it. Full segmentation algorithms must take into account significantly more information to be able to properly classify these structures.

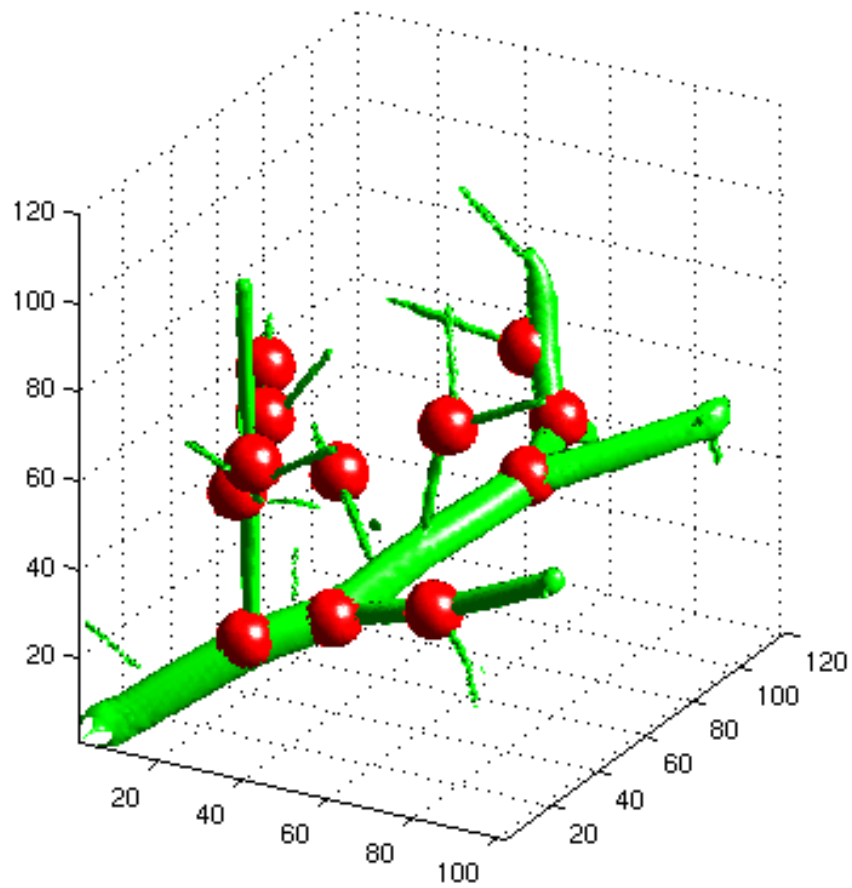


Figure 5.17: An illustration of detected bifurcations in 3D; the vessels were enhanced with the Frangi vesselness filter, while the bifurcations (marked with blobs) were detected with the bifurcationness filter.

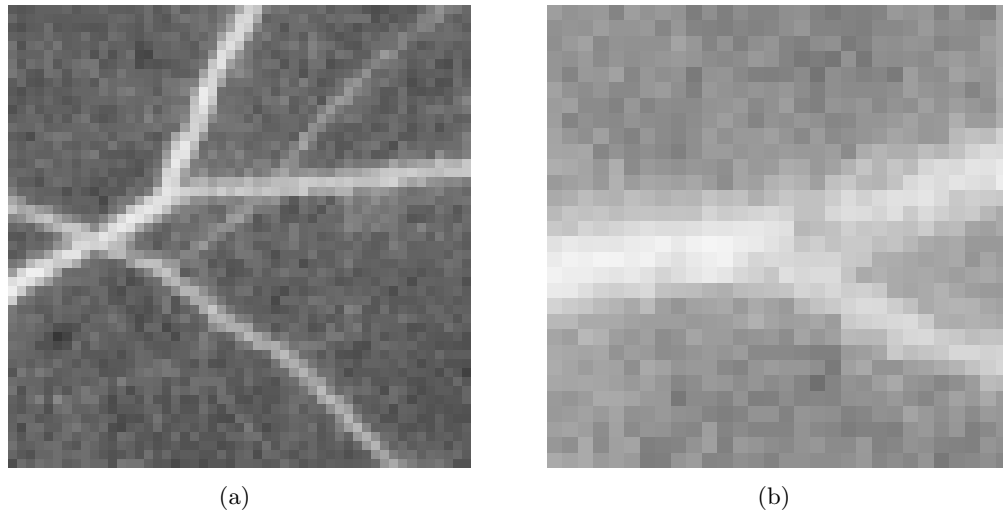


Figure 5.18: Difficult situations in retinal images



Figure 5.19: Overlap of bifurcation and crossing in retinal images: original image (contrast enhanced) and two expert segmentations

Chapter 6

Conclusion and Future Directions

The research presented here can be summarized in the following points:

1. Good overall detectors for bifurcations, for both 2D and 3D images, are λ_1 (the smallest eigenvalue of the Hessian) and the classic blob detector Determinant of Hessian, in spite of the fact that the vessels connected to a bifurcation extend indefinitely and can not be considered localized.
2. For 3D images, the new operator $|\lambda_1|(|\lambda_3| - |\lambda_2|)$ is a better choice, with enhanced response at bifurcations while reducing the signal at the end-of-vessels and at blobs.
3. To distinguish between blobs and bifurcations/crossings, we introduced the concept of *codimension*. While designed to eliminate blobs, this concept can be used to reduce noise signal (since noise pixels can be seen as “extremely small blobs” – although codimension can not be reliably estimated if the noise pixels are on the vessel)

In conclusion, we showed that it is possible to build a simple bifurcationness filter with good sensitivity, based on a simple scale-space conversion of the original image. The accuracy of the detected bifurcation was good as long as no other features were in close proximity of the bifurcations, with most of the detected bifurcations within one vessel radius of the real position. In some cases, bifurcations were correctly resolved even when they *were* in close proximity to other structures such as end-of-vessels. Adding moderate noise did not affect significantly the accuracy of the algorithm, as scale-space is inherently immune to small amounts of noise. Even the salt-and-pepper noise has little influence if present in moderate amounts.

The algorithm proposed can be improved, with further research. For example, noise robustness could be improved by using neighborhood information to reduce the influence of noise. Noise pixels are not normally correlated to each other, but pixels with signals from scale-space operators are.

This algorithm, in the current implementation, does not distinguish between crossings and bifurcations. This distinction is impossible based only on detection of local features and codimension. For some applications this is not a significant drawback. When such a distinction is required, one can build an additional filter. For example, there are three centerlines adjoining a bifurcation, but four at a crossing. In addition, the centerlines corresponding to each of the two crossing vessels are on the same direction, with similar intensity profiles in a section perpendicular to the centerline.

The derivatives with respect to scale are obtained by discrete approximation, therefore subject to errors. Better approximations require smaller steps with respect to scale, but this increases considerably the computing time. However, all the information required to obtain evolution with scale of any quantity is already encoded in the original image, and the derivatives with respect to scale of any quantity at any given scale are encoded in the image at that particular scale. In the case of intensity, the first derivative with respect to the scale parameter can be obtained using the heat equation 2.5. The second derivative can be obtained by applying this equation again, thus allowing us to calculate the codimension from the image at a single scale. However, this method requires computing the Laplacian-of-Laplacian, involving higher order spatial derivatives and thus even more sensitive to noise and the proximity of other structures.

A main weakness of the algorithm is the insensitivity to vessels with weak signals, close to noise level. Some of these can be identified by human observers, even though they are little more than a subtle change in noise statistics. The images which were at the threshold of 95% detectability (Figures 5.5 and 5.7) do not appear particularly noisy to the human eye, yet they are problematic for automatic algorithms. The reason is that the positions of the noisy pixels are not correlated to each other, thus forming a more-or-less uniform background, the positions of the signal pixels *are* correlated, and the human brain is able to extract this correlation. The clinical images where the bifurcation were not detected had portions close to the noise level, and sometimes appear to be interrupted close to the bifurcation. For such situations, we plan to develop a perceptually-oriented approach, which will be more appropriate for detection and removal of background clutter. Future refinements could

include selection of regions of interest around the detected bifurcation candidates for more detailed investigations using computationally intensive algorithms. The simplicity of the algorithm – one-step, without requiring training data – makes it a good addition to the arsenal of medical diagnosis.

Appendix A

Geometry of Vascular Bifurcations

Based on computer models of arterial trees, hemodynamic simulation studies have been used to better understand both diagnostic and therapeutic aspects of blood flow. Vascular models have been developed to cover all levels of vascular tree detail. Full vascular trees are used as a realistic geometrical substrate for hemodynamic simulation studies. These synthetic trees can be realistically grown based on a spatially-varying oxygenation map while enforcing the physical constraints [16, 20]. Such models can be used to simulate processes such as the adaptation of arterial diameters to changes in blood flow rate or the formation different patterns of angiogenesis induced by changing needs of blood supply. These synthetic trees, with realistic bifurcation statistics, are also necessary for quantitative investigations of segmenting methods, since the location and size of blood vessels and their bifurcations is exactly known, without a need for human experts.

At the opposite end are detailed mesh models such as those developed in [37], with great attention paid to accurate representation of surfaces and smooth blending of branching. Such detailed models can be used for numerical simulation of blood flow at bifurcations [19], showing the location of areas with turbulent flow and low shear stress. Clinical in-vitro studies show the correlation of high turbulence with cell proliferation, which, in turn, may cause atherosclerosis [2].

For the purpose of this work, we are interested only in a modestly realistic model of vascular bifurcations (bifurcation angles and ratio), without concern about the internal structure. The theoretical work on bifurcations of blood vessels and airways has its roots in the papers published by Murray in 1926 [35, 34]. While the mathematical model and the objective function function have been refined over the years, the basic principles remain the

same [14]. The supporting experimental data, however, are much more difficult to obtain. This appendix presents the results from one of the most comprehensive studies to date [49]

A.1 Bifurcation Ratio

The model for a blood vessel is simply a cylinder, while the blood is considered a Newtonian fluid. Thus, Poiseuille's law can be directly applied to obtain the power dissipation in the blood vessel. Minimizing this power requires large diameters. On the other hand, maintaining the volume of blood requires a power consumption proportional to the volume of the vessel. These two contributions are combined to give the total power dissipation P_t for an unbranched vessel of length l and radius r :

$$P_t = f^2 \frac{8\eta}{\pi} \frac{l}{r^4} + w_v r^2 l \quad (\text{A.1})$$

where η is the viscosity coefficient of the blood, f and w_v are weight factors; the weight factor f describes the quantity of fluid per unit time [44, 35, 34, 14, 47]. Without going into details, the fundamental result is that the radii of the parent vessel and the daughter vessels obey a power law. If we use subscript 0 for the parent and subscripts 1 and 2 for the daughters (with the convention that $r_1 > r_2$), this is known as Murray's law:

$$r_0^\gamma = r_1^\gamma + r_2^\gamma \quad (\text{A.2})$$

In Murray's law, theoretical considerations set γ to 3. A recent extension of Murray's law [41] to non-Newtonian fluids showed theoretically that $\gamma = 3$ if the volume constraint (i.e., the metabolic cost of maintaining blood volume) is used, regardless of viscosity type of blood (Newtonian or non-Newtonian). If the volume constraint is replaced by a surface constraint (related to the internal surface of vessel and the total shear force), the theoretical value for the exponent was found to be $\gamma = 2.5$ for Newtonian fluid and 2.42-2.46 for non-Newtonian fluids, depending on viscosity parameters. The experimental measurements [31, 49] support the value $\gamma = 3$ to within a few fractions of a percent, well within experimental errors. In particular, [31] presents measurements made *in vivo* for blood flow versus arteriole diameter for diameters between 6 and 108 microns diameter, presented in Figure A.1.

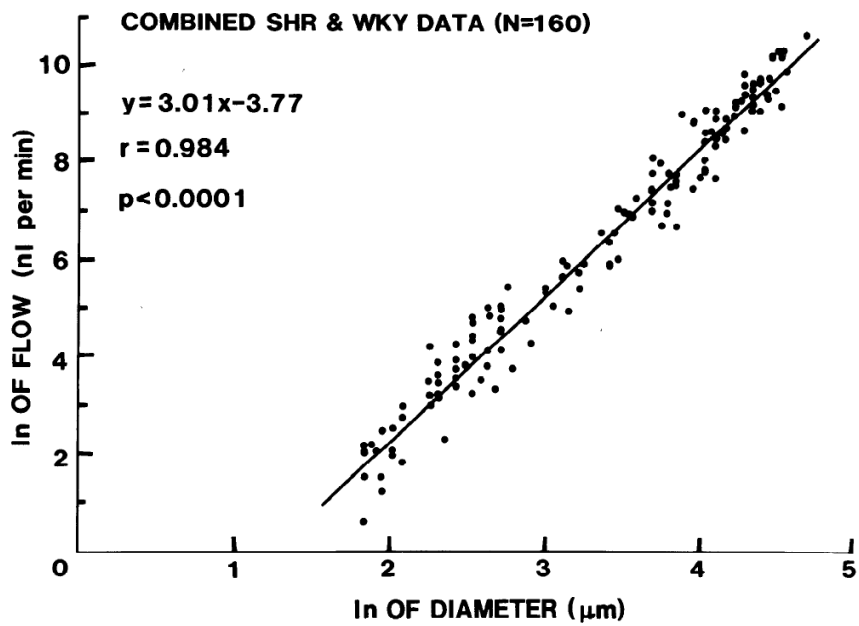


Figure A.1: Data and regression line obtained for 160 paired flow-diameter measurements in [31], used to determine the exponent of the power law

If we use $\alpha = r_2/r_1$ as the splitting ratio (note that many works use α for *area* ratio, not for radius/diameter ratio), we obtain the radii of the daughter vessels as

$$\frac{r_1}{r_0} = \frac{1}{[1 + \alpha^3]^{1/3}} \quad (\text{A.3})$$

$$\frac{r_2}{r_0} = \frac{\alpha}{[1 + \alpha^3]^{1/3}} \quad (\text{A.4})$$

which, after simple calculations, gives the dimensionless area ratio

$$\beta = \frac{r_1^2 + r_2^2}{r_0^2} = \frac{1 + \alpha^2}{(1 + \alpha^3)^{2/3}} > 1 \quad (\text{A.5})$$

If we have a 2D image, the cross-section area is simply the diameter ratio

$$\beta = \frac{r_1 + r_2}{r_0} = \frac{1 + \alpha}{(1 + \alpha^3)^{1/3}} > 1 \quad (\text{A.6})$$

The main difference is that the area ratio varies from about 1.07 (for splitting ratio $\alpha = 0.3$, corresponding to the smallest area ratio of about 0.1 observed in the experimental works) to 1.26 (for equal splitting ratio), while the diameter ratio varies from about 1.28 to about 1.58.

In [49], the exponent γ of the bifurcations is not determined, but the diameter measurements at bifurcations are plotted against theoretical curves obtained from the cubic law (equations A.3 and A.4). These graphs are presented in Figure A.2

A.2 Bifurcation angles

The optimality principle can be applied to calculate the bifurcation angles. For this, consider a source point S (parent vessel) and two destination points A and B, with a destination point C somewhere in the middle. The optimality principle dictates that the vessel segments between C and each of the points S, A, B are straight lines and that these lines lie in the same plane. Now, if the bifurcation is optimal, the point C is at the minimum of the objective function. The conditions for the point C can be obtained by applying to it small displacements in all directions (see Fig. A.3)

Using this method, analytical results can be obtained for four different optimality principles [47, 46], which can be grouped in pairs:

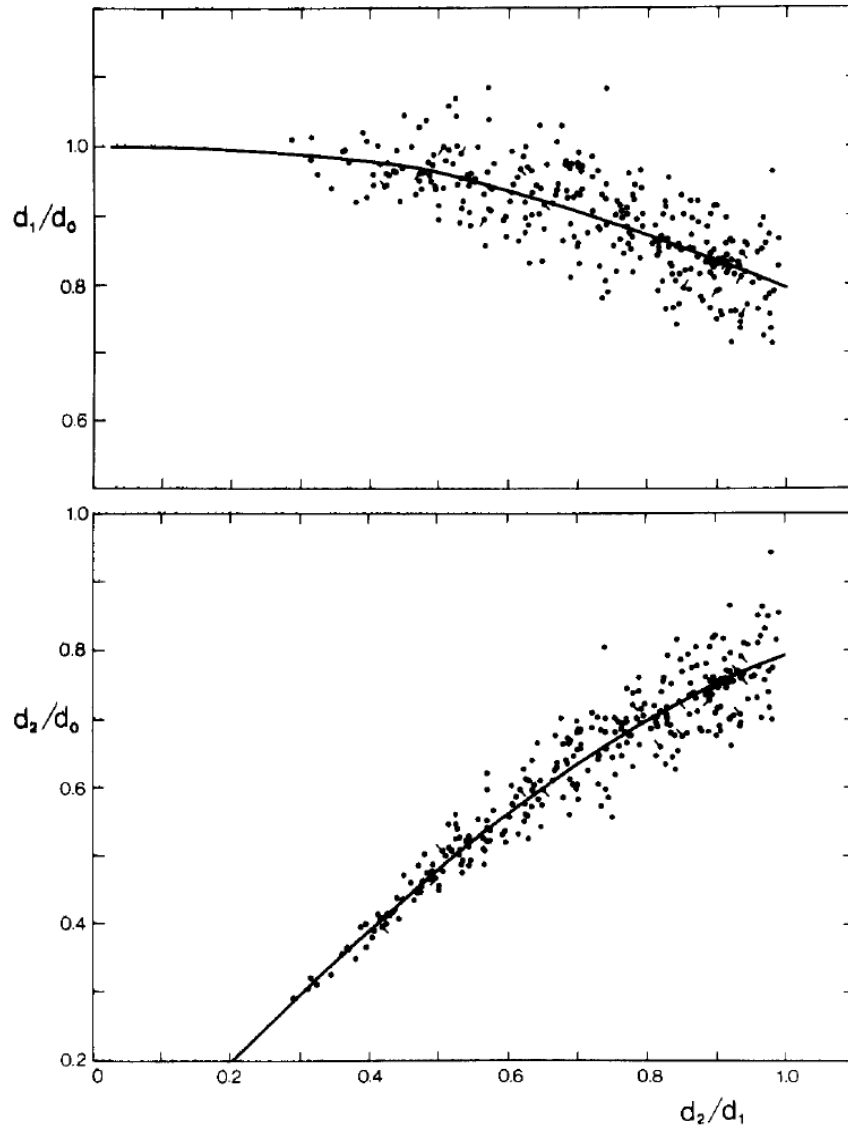


Figure A.2: Measurements of branch diameters in different parts of the arterial tree by Zamir [49], plotting normalized daughter diameters versus diameter splitting ratio. Solid lines are theoretical values from Eqns.A.3 and A.4

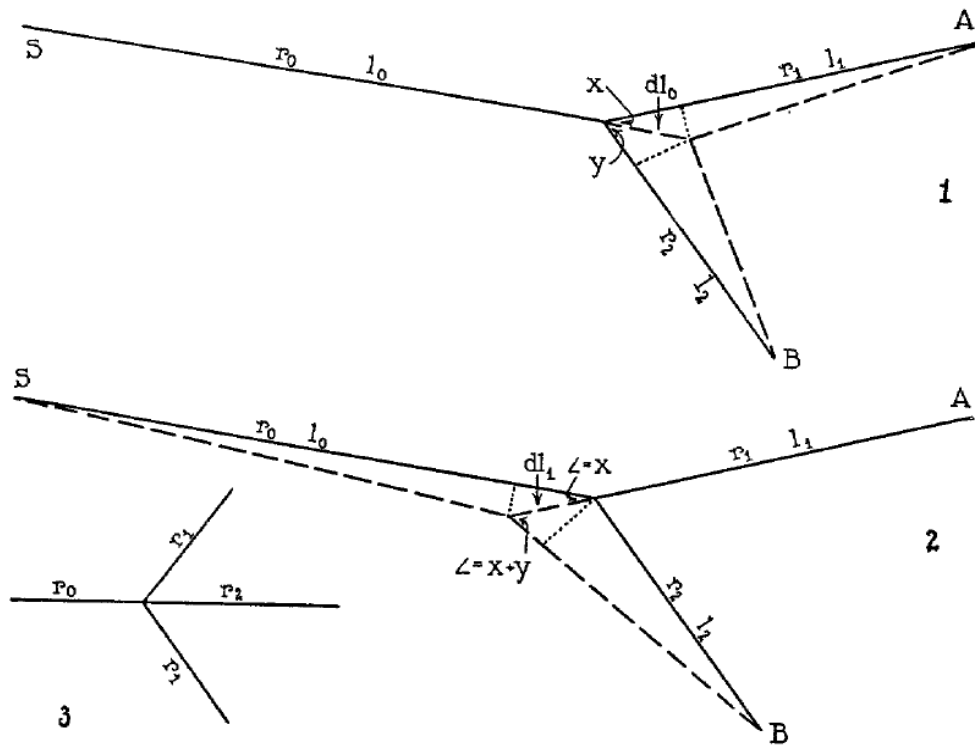


Figure A.3: Small displacements are applied to the bifurcation point to obtain the optimality condition. From [34].

- For minimum pumping power and minimum lumen volume:

$$\begin{aligned}\cos \theta_1 &= \frac{(1 + \alpha^3)^{4/3} + 1 - \alpha^4}{2(1 + \alpha^3)^{2/3}} \\ \cos \theta_2 &= \frac{(1 + \alpha^3)^{4/3} + \alpha^4 - 1}{2\alpha^2(1 + \alpha^3)^{2/3}}\end{aligned}\tag{A.7}$$

- For minimum drag and minimum lumen surface:

$$\begin{aligned}\cos \theta_1 &= \frac{(1 + \alpha^3)^{2/3} + 1 - \alpha^2}{2(1 + \alpha^3)^{1/3}} \\ \cos \theta_2 &= \frac{(1 + \alpha^3)^{2/3} + \alpha^2 - 1}{2\alpha(1 + \alpha^3)^{1/3}}\end{aligned}\tag{A.8}$$

Experimental data shows that there is significant spread in the measured angle values around the theoretical curves. Where a vessel was not straight, and many were not, the cursor line was aligned with the vessel at the bifurcation point. The difficulties in determining the enhances the spread of experimental data when compared to the theoretical curve. We can conclude that the angle between the daughter branches is about 90° , with significant spread between 60 and 120 degrees.

A two-dimensional bifurcation provides the shortest route for blood flow from the parent artery to the branches; it would be expected, therefore, that although the arterial tree is highly three-dimensional, arterial bifurcations would be mostly two-dimensional. The measurements are not easy, and only Zamir [49] published detailed measurements of the angle δ between the parent artery and the plane of the two daughter branches. The results indicate that the arterial bifurcations are indeed mostly two-dimensional. The deviations from zero δ are not unreasonable in a biological system.

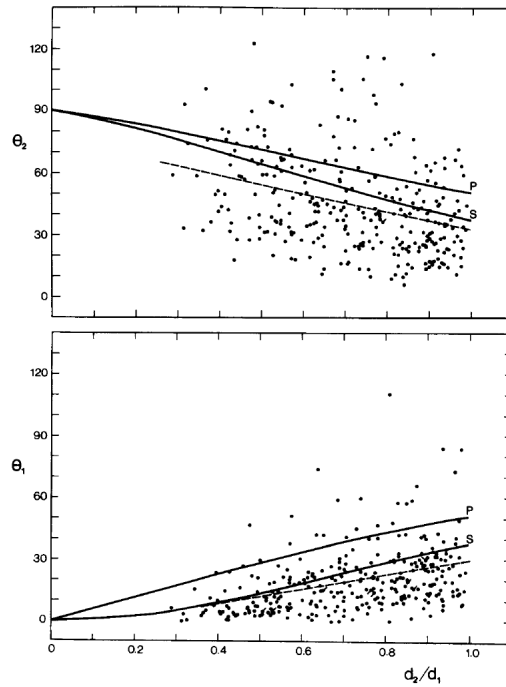


Figure A.4: Measurements of the branching angles from the arterial tree of a rat compared with theoretical curves for minimum power (P) and minimum surface/shear (S). From [49]

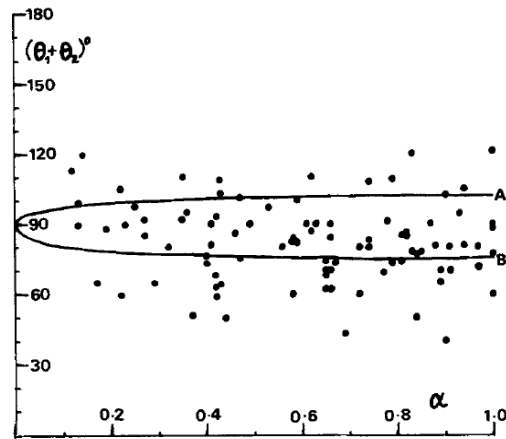


Figure A.5: Measurements of the angle between the daughter branches compared with theoretical curves for minimum surface (A) and minimum power (B). From [48]

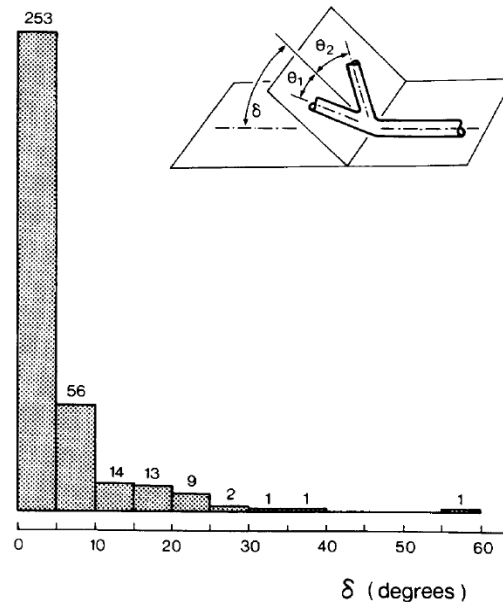


Figure A.6: Measurements of the angle between the parent vessel and the plane of the daughter vessels. From [49]

Appendix B

Helper Routines

B.1 Drawing a Cylinder in Matlab

The single straight cylinder is the basis for generating synthetic bifurcations, used for extensive testing of the detection algorithm. The method is written in vectorial form, so it can be applied in any number of dimensions.

B.1.1 Geometry

To draw a cylinder with radius r and axis between \vec{x}_1 and \vec{x}_2 , we need two elements to determine the intensity value at an arbitrary point:

1. The projection of the point on the line connecting x_1 and x_2 (the cylinder axis)
2. The distance between the point and the cylinder axis

In vectorial form, the line connecting \vec{x}_1 and \vec{x}_2 is given by the parametric form

$$\vec{r}(t) = \vec{x}_1 + t(\vec{x}_2 - \vec{x}_1) \tag{B.1}$$

so points between \vec{x}_1 and \vec{x}_2 correspond to values of parameter t between 0 and 1.

The first item is solved by obtaining \vec{r}_{\parallel} , the component of $\vec{r} = \vec{x} - \vec{x}_1$ parallel to $\vec{r}_{12} = \vec{x}_2 - \vec{x}_1$ (obtained by projection, or scalar/dot product). The value of t is simply the ratio of the norms of \vec{r}_{\parallel} and \vec{r}_{12} :

$$t = \frac{\|\vec{x}_{\parallel}\|}{\|\vec{r}_{12}\|} = \left(\vec{r} \cdot \frac{\vec{r}_{12}}{\|\vec{r}_{12}\|} \right) \frac{1}{\|\vec{r}_{12}\|} = \frac{\vec{r} \cdot \vec{r}_{12}}{\|\vec{r}_{12}\|^2} \tag{B.2}$$

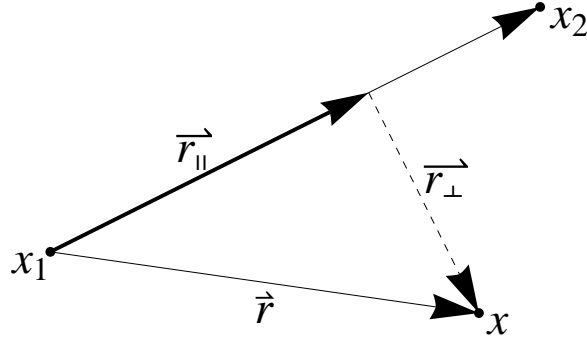


Figure B.1: Geometry used for generating a single cylinder image

The second item is solved by calculating the norm of r_{\perp}^{\rightarrow} , the perpendicular component of r^{\rightarrow} ,

$$d = \|x_{\perp}\| = \|\vec{r} - r_{\parallel}^{\rightarrow}\| = \|\vec{r} - t \cdot r_{12}^{\rightarrow}\| \quad (\text{B.3})$$

In practice, the descriptors for vessel profile use d^2 (Gaussian and parabolic profiles), while others can be reformulated to use it by altering some constants (e.g., rectangular profile), so the squared distance can be directly computed using Pythagoras theorem:

$$d^2 = \|x_{\perp}\|^2 = \|\vec{r}\|^2 - t^2 \cdot \|r_{12}^{\rightarrow}\|^2 = \|\vec{r}\|^2 - \frac{(\vec{r}^{\rightarrow} \cdot r_{12}^{\rightarrow})^2}{\|r_{12}^{\rightarrow}\|^2} \quad (\text{B.4})$$

B.1.2 Matlab Implementation

The above formulas can be easily implemented in any programming language. However, for efficient implementation, language- (and sometimes even platform-) specific formulation must be used. In Matlab, it is better to use its built-in vectorial formulation, since these use high-performance libraries optimized for cache memory and can use multiple cores. From the equations for t and d^2 we can see that there is no need to use the normalized version of t , thus saving some computation time. The program works as follows:

1. Allocate the space for the image;
2. Compute the vector corresponding to the axis and its squared norm;
3. (Dimension-specific part):

- (a) Create volumes for the coordinates of each point (required for the use of vectorized form in Matlab)
 - (b) Compute the components of $\vec{r} = \vec{x} - \vec{x}_1$ for all points in the image
 - (c) Compute $t = \vec{r} \cdot \vec{r}_{12}$ for all points
 - (d) Compute d^2 for all points (Eq. B.4)
4. Using d^2 , compute image intensity for all points in image
 5. Set to 0 all points whose projection falls outside the axis of the cylinder
 6. Optionally, add round ends to the segment

Multiple such branches can be combined into a single bifurcation or tree by overlapping the components with the built-in function **max()**.

Listing B.1: Matlab routine used to generate a single bifurcation branch

```

1 function vol=branch(siz , x1 , x2 , r , profile )
2
3 % Generates a volume filled with a cylinder from x1 to x2 and radius
4 % r in a volume of size siz.
5 %
6 % Input:
7 % siz: a vector containing the size volume of interest
8 % x1 , x2: the points defining the axis of the cylinder , vectors
9 % r: number, the radius of the cylinder
10
11
12 %Number of dimensions in image. Must be 2 or 3
13 ndims=max(size(siz ));
14 % If the ends are rounded or not
15 round=1;
16
17 if nargin<5, profile='rect'; end;
18
19 % Allocate the return volume

```



```

20 vol=zeros(siz);
21 % Vector definig the axis of the cylinder
22 x21=x2-x1;
23 % and its squared norm
24 x21s=dot(x21,x21);
25 % Dimension-specific part
26 if(ndims==2)
27     % Create the volumes of coordinates
28     [X,Y]=ndgrid(1:siz(1), 1:siz(2));
29     % Components of vector x-x0
30     x10_1=X-x1(1);
31     x10_2=Y-x1(2);
32     % Scalar/dot product between x-x1 and x21=x2-x1
33     t=( x10_1*x21(1) + x10_2*x21(2) );
34     % Squared distance to cylinder axis
35     d2=(x10_1.*x10_1 + x10_2.*x10_2 ) -t.*t./x21s;
36 elseif(ndims==3)
37     % Create the volumes of coordinates
38     [X,Y,Z]=ndgrid(1:siz(1), 1:siz(2), 1:siz(3));
39     % Components of vector x-x0
40     x10_1=X-x1(1);
41     x10_2=Y-x1(2);
42     x10_3=Z-x1(3);
43     % Scalar/dot product between x-x1 and x21=x2-x1
44     t=(x10_1*x21(1) + x10_2*x21(2) + x10_3*x21(3));
45     % Squared distance to cylinder axis
46     d2=(x10_1.*x10_1 + x10_2.*x10_2 + x10_3.*x10_3) -t.*t./x21s;
47 end;
48
49 % volume inside cylinder gets value 1, outside gets 0
50 switch profile
51     case { 'rect ', 'square ' }
52         vol(d2<=(r*r))=1;

```

```

53     case 'gauss'
54         vol=exp(-d2/(2*r*r));
55     case 'parab'
56         vol=1-d2/(r*r);
57         vol(vol<0)=0;
58 end;
59 % Set to 0 volume beyond the axes of the cylinder
60 vol(t<0)=0;
61 vol(t>x21s)=0; % t is not normalized
62
63 if(round)
64     % Round end at x1
65     if(ndims==2)
66         d2=(x10_1.*x10_1 + x10_2.*x10_2 );
67     elseif(ndims==3)
68         d2=(x10_1.*x10_1 + x10_2.*x10_2 + x10_3.*x10_3 );
69     end;
70     v2=zeros(siz);
71     switch profile
72         case {'rect', 'square'}
73             v2(d2<=(r*r))=1;
74         case 'gauss'
75             v2=exp(-d2/(2*r*r));
76         case 'parab'
77             v2=1-d2/(r*r);
78             v2(v2<0)=0;
79     end;
80     vol=max(vol , v2);
81
82     % Round end at x2
83     if(ndims==2)
84         x10_1=X-x2(1);
85         x10_2=Y-x2(2);

```

```

86         d2=(x10_1.*x10_1 + x10_2.*x10_2 );
87     elseif(ndims==3)
88         x10_1=X-x2(1);
89         x10_2=Y-x2(2);
90         x10_3=Z-x2(3);
91         d2=(x10_1.*x10_1 + x10_2.*x10_2 + x10_3.*x10_3 );
92     end;
93     v2=zeros(siz);
94     switch profile
95         case {'rect', 'square'}
96             v2(d2<=(r*r))=1;
97         case 'gauss'
98             v2=exp(-d2/(2*r*r));
99         case 'parab'
100            v2=1-d2/(r*r);
101            v2(v2<0)=0;
102     end;
103     vol=max(vol, v2);
104 end;

```

B.2 Generating a 2D Bifurcation

In 2D, generating a synthetic bifurcation is a straightforward implementation of the formulas in A. The morphology of bifurcations as observed in clinical data (summarized there), however, shows significant deviations from the theoretically ideal values. Therefore, the calculated values are modified using random Gaussian variables. The algorithm uses as input the radius of the parent vessel, r_0 and the bifurcation ratio α_0 . Additional parameters needed are the length of each branch, l , and the orientation of the parent branch, θ_0 :

Listing B.2: Generating a bifurcation in 2D

```

1  r0=5;
2  alphaR=1;
3  r2=r0/(1+alphaR^3)^(1/3);

```

```

4  r1=alphaR*r2;
5  th1a=acos((r0^2+r1^2-r2^2)/(2*r0*r1));
6  th1b=acos((r0^4+r1^4-r2^4)/(2*r0^2*r1^2));
7  th1 =normrnd((th1a+th1b)/2,0.7*abs(th1a-th1b));
8  th2a=acos((r0^2-r1^2+r2^2)/(2*r0*r2));
9  th2b=acos((r0^4-r1^4+r2^4)/(2*r0^2*r2^2));
10 th2 =normrnd((th2a+th2b)/2,0.1*abs(th2a-th2b));
11 %Draw branches accordingly
12 r=40; % branch length
13 b0=branch([nx,ny],[nx/2,ny/2],\
14           [nx/2+r*cos(th0),ny/2+r*sin(th0)],\
15           r0,profile);
16 lini=b0;
17 b1=branch([nx,ny],[nx/2,ny/2],\
18           [nx/2-r*cos(th0+th1),ny/2-r*sin(th0+th1)],\
19           r1,profile);
20 lini=max(lini,b1);
21 b2=branch([nx,ny],[nx/2,ny/2],\
22           [nx/2-r*cos(th0-th2),ny/2-r*sin(th0-th2)],\
23           r2,profile);
24 lini=max(lini,b2);

```

B.3 Local Maxima in Matlab

Although Matlab has an extremely large number of functions available, it does not have a function for detecting local maxima. A quick-and-dirty method can be implemented in only two instructions — perform a grayscale dilation using a mask corresponding to the neighborhood to be searched and check which points have the same intensity value in the original image and in the dilated image. Obviously, the second argument of `imdilate()` must be set to an appropriate value for 2D and 3D images; see Matlab internal documentation of `imdilate()` for details.

Listing B.3: Detecting local maxima in Matlab

```
1 b1=imdilate(q1,ones(5,5,5));  
2 b1=(b1==q1);
```

Appendix C

Analysis of the Frangi Vesselness

In 1998, Frangi *et al* [13] proposed a vessel enhancement filter based on scale-space properties of blood vessels. The authors used an analysis of Hessian eigenvalues to select points likely to be on the vessels. Since the blood vessels are quasi-one-dimensional structures (strong variation in two transverse directions – for 3D images, only one direction for 2D images – but much slower variation in the other direction), their main characteristic (for bright structures on dark background) is:

- In 2D images, one of the Hessian eigenvalues is negative and with much larger magnitude than the other
- In 3D images, the two largest eigenvalues are negative and comparable in magnitude, while the third eigenvalue is much smaller in magnitude
- Since vessels are strong maxima in the transverse direction(s), the condition for local maximum is set as a filter: the largest (in magnitude) eigenvalues must be negative. Frangi obtains this criterion for the local maximum with respect to the transverse coordinates, but applying it effectively segments the vessel with a well-known edge detector, the zeros of the second derivative. Frangi does not use the criterion of low gradient since there is no guarantee that the derivative along the axis has a low value.

The sign of the smallest Hessian eigenvalue (second derivative along the axis) is not important. Based on this analysis, they define two geometric measures for the general shape of the second-order (Hessian) ellipsoid. The criteria are then used as arguments to functions which have high value when the criteria are met and low value as the criteria are

farther from the desired value. The criteria are combined in a single formula by simply multiplying them. The method works at any scale; however, there is an optimum scale for each structure where it gives the strongest response. Therefore, the resulting function is evaluated for all spatial points at all scales, then a final image is built by taking for each point the maximum of the detection function across scales. The complete expressions include geometrical constants to express volumes and areas from eigenvalues, but here they are omitted for simplicity.

The first geometrical criterion accounts for deviations from a blob-like structure,

$$\mathcal{R}_B = \frac{\text{Volume}}{(\text{Largest cross-section area})^{3/2}} = \frac{|\lambda_1|}{\sqrt{|\lambda_2\lambda_3|}} \quad (\text{C.1})$$

Since for blobs all eigenvalues are of comparable magnitude while for the other structures the smallest eigenvalue is much smaller, this \mathcal{R}_B must be as large as possible (although it can not be larger than 1, since λ_1 is the smallest eigenvalue in magnitude). This formula is valid only for volumetric images; for 2D images, it becomes simply $\mathcal{R}_B = \frac{|\lambda_1|}{|\lambda_2|}$. To encourage values close to 0, Frangi uses a Gaussian function centered on the ideal value, $\exp(-\mathcal{R}_B^2/(2\beta^2))$. The Gaussian has an additional parameter, its width β , controlling how much the geometrical constraint is allowed to vary from its ideal value.

A low value for \mathcal{R}_B only eliminates point-like structures. The other distinguishes between plate-like and line-like structures; this distinction is needed only in 3D images:

$$\mathcal{R}_A = \frac{\text{Largest cross-section area}}{(\text{largest semiaxis length})^{3/2}} = \frac{|\lambda_2|}{|\lambda_3|} \quad (\text{C.2})$$

Since for a vessel there is strong variation in two direction, the two largest eigenvalues are comparable, and \mathcal{R}_A is close to 1. For a plate structure, strong variation occurs only in one direction, so \mathcal{R}_A is close to 0. To penalize plate-like structures, Frangi uses again the Gaussian function centered at 0 (which encourages plates), but subtracts it from 1, $1 - \exp(-\mathcal{R}_A^2/(2\alpha^2))$.

These criteria only use the *relative* values of the eigenvalues, therefore are very susceptible to noise. To counteract this, Frangi multiplies the resulting function with a saliency-based factor. He chooses as saliency the Frobenius matrix norm of the Hessian,

$$\mathcal{S} = \sqrt{\sum_{i \leq D} \lambda_i^2} \quad (\text{C.3})$$

Another measure for the saliency, which works just as well (in our experiments there was no discernible difference) is the absolute value of the largest (in magnitude) eigenvalue. It

is easy to see why this works: it is the sum of magnitudes for all tensor components — ball, plate, stick.

To encourage large saliency values, Frangi uses a Gaussian-based function, $1 - \exp(-\mathcal{S}^2/(2c^2))$. We note that in this case there is no *a priori* maximum value, so it is useful to have a function that saturates at large values. A saliency factor of the form $\tanh(\mathcal{S}/c)$, which also is 0 at low saliency and saturates at 1 for large saliency, would have worked just as well. With these considerations, the final vesselness becomes

$$\mathcal{V}(\mathbf{x}, s) = \left(1 - \exp\left(-\frac{\mathcal{R}_A^2}{2\alpha^2}\right)\right) \exp\left(-\frac{\mathcal{R}_B^2}{2\beta^2}\right) \left(1 - \exp\left(-\frac{\mathcal{S}^2}{2c^2}\right)\right) \quad (\text{C.4})$$

if λ_2 and λ_3 are negative, the vesselness being 0 otherwise.

This operator has three adjustable parameters. For each of these parameters, Frangi used a value halfway through the allowable range — 0.5 for α and β (since \mathcal{R}_A and \mathcal{R}_B only take values between 0 and 1) and half of the maximum Hessian norm for c at the scale currently investigated. In 2D images there are only two eigenvalues, so the factor corresponding to \mathcal{R}_A is missing.

While the choice of value localization function is irrelevant, some choices are more intuitive than others. For example, to penalize plate structures, Frangi uses $1 - \exp(-\mathcal{R}_A^2/(2\alpha^2))$. Since \mathcal{R}_A takes values only between 0 and 1, and the desired value is 1, a more natural choice for the penalty function is $\exp\left(-(\mathcal{R}_A - 1)^2/(2\alpha^2)\right)$.

The ball/plate/stick (parameters b, p, s) interpretation of the Hessian ellipsoid presented in 3.1 allows us to reinterpret the geometric parameters. It is useful to look at each component relative to the others. Since

$$\lambda_1 = b \quad (\text{C.5})$$

$$\lambda_2 = b + p \quad (\text{C.6})$$

$$\lambda_3 = b + p + s \quad (\text{C.7})$$

then we note that \mathcal{R}_B is simply the normalized ball component; using the largest eigenvalue λ_3 instead of $\sqrt{|\lambda_2\lambda_3|}$ works just as well, so this geometrical parameter becomes

$$\mathcal{R}_B = \frac{b}{b + p + s} \quad (\text{C.8})$$

Let's look now at \mathcal{R}_A . This geometric parameter has an ideal value of 1, so it appears more natural to use $\exp\left(-(\mathcal{R}_A - 1)^2\right)$ to penalize deviations from the central value 1. This

expression can be processed, then the eigenvalues replaced with ball/plate/stick components

$$(1 - \mathcal{R}_A)^2 = \left(1 - \frac{|\lambda_2|}{|\lambda_3|}\right)^2 = \left(\frac{|\lambda_3| - |\lambda_2|}{|\lambda_3|}\right)^2 = \left(\frac{s}{b + p + s}\right)^2 \quad (\text{C.9})$$

In other words, Frangi's criterion for \mathcal{R}_B looks for areas with low relative ball component, while the criterion for \mathcal{R}_A looks for areas with low relative stick component. This is equivalent to look for areas with high relative *plate* component $p/(b + p + s) = (|\lambda_2| - |\lambda_1|)/|\lambda_3|$, close to 1 (since the sum of all three is always 1)

With this analysis, Frangi's 3D vesselness can be reformulated (including the saliency factor) as

$$\mathcal{V} = \exp \left[-\frac{1}{2\alpha^2} \left(1 - \frac{p}{b + p + s}\right)^2 \right] \left(1 - \exp \left(-\frac{\mathcal{S}^2}{2c^2}\right)\right) \quad (\text{C.10})$$

We can now put side by side the two forms of vesselness: the original one \mathcal{V}_F with the geometrical parameters reinterpreted in terms of tensor components, and the reformulated version, with a single term encouraging high plateness, \mathcal{V}_S . For simplicity, the saliency factor is excluded, and the Gaussian parameters are set to the middle of the allowed interval, $\alpha = \beta = 1/2$:

$$\mathcal{V}_F = \exp \left[-2 \left(\frac{s}{b + p + s}\right)^2 \right] \exp \left[-2 \left(\frac{b}{b + p + s}\right)^2 \right] \quad (\text{C.11})$$

$$\mathcal{V}_S = \exp \left[-2 \left(\frac{s + b}{b + p + s}\right)^2 \right] \quad (\text{C.12})$$

Since the ball/plate/stick components b , p , s are all positive, the two expressions have the same effect.

The 2D version of the vesselness filter is pretty obvious: since vessels, as linear structures, have already expressed in terms of low relative ballness. In all cases, the response is calculated at all scales, then the maximum is taken across all scales to obtain the final map. Of course, the response is taken only for points on bright structures, so the largest eigenvalue(s) must be negative.

Since Frangi's vesselness looks for high relative stickness (in 2D images) or plateness (in 3D), then multiplies them by the saliency function, another alternative is to look directly for high *absolute* stickness s (2D) or plateness p (3D), both given by $|\lambda_2| - |\lambda_1|$, the difference of absolute values of the two lowest Hessian eigenvalues. The comparison of the two versions is shown in Figure C.1. In C.1(a) we have the original image, a fragment of a noisy angiogram

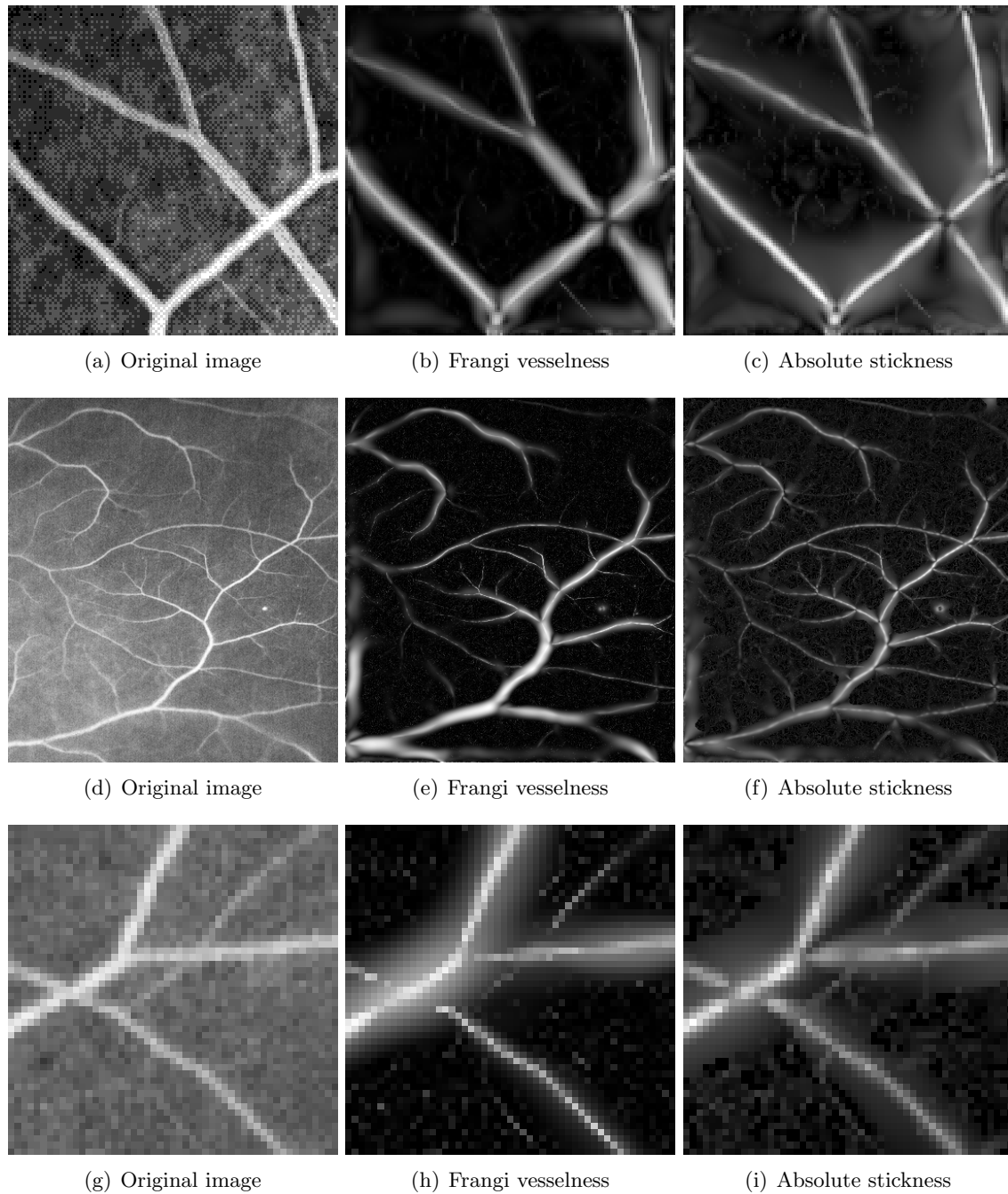


Figure C.1: Comparison of vesselness filters applied to a noisy angiogram (top row) and to a fluorescein-enhanced retinal image (middle row). From left to right: original image, image filtered with Frangi vesselness, and the multiscale stick. Bottom row: detail of a weak vessel in the retinal image

(there are only 8 levels of grey, and most of the apparent shades are dithered). The result of applying the Frangi vesselness is shown in C.1(a), while C.1(c) shows the result of applying the absolute stickness filter alone. The results are similar. While the Frangi vesselness does a better job at suppressing the background, the vessels themselves are better shaped if we use the simple stickness measure. The reason for this difference is shown in Figure C.2. In this figure, the solid line is the Gaussian penalty used by Frangi, while the dashed line is the direct use of the normalized variable. The variables used in the Gaussian penalty are normalized, so they are always between 0 and 1, and the Gaussian parameter is set as in Frangi to half the domain of the variable (0.5). The Gaussian starts with a zero derivative (hence its stronger suppression of low intensity values and noise), but it has an inflexion point at 0.5 where its derivative is maximum. At the end of the interval, the derivative of the Gaussian is smaller than that of the straight line (therefore the vessels appear sharper when using the simple stick component).

Where Frangi wants to enhance *large* values (for example in the case of saliency), he uses a “reverse Gaussian” function $1 - \exp(-\mathcal{S}^2/(2c^2))$. Since the values are normalized so that the maximum value is 1, one might think that a function like $\exp(-\infty - \mathcal{S}^2/(2c^2))$ might be better suited. Indeed, Frangi does not give any justification for the choice of transfer function, and as we saw, any function works as long as it is monotonical. However, a Gaussian penalty centered at the desired value has a flat peak, and thus gives a poorly defined maximum, which is a disadvantage if we want to identify the centerline later.

We note that the small vessel in Figure C.1(g), while it appears distinct to the human eye in the original image, it appears drowned in the signal from the main vessel in the Frangi-enhanced vessels (C.1(h)), but due to the sharper centerline, it appears more distinct when using the simple filter of absolute stickness. We note that the vessel close and parallel to the left edge in the full retinal image appears very diffuse in both enhanced images due to interference from the edge of the image.

In Figure C.3, the same set of filters is applied to an image from the DRIVE database. The original images are in RGB colour format; here we used only the green channel for processing; the red channel is saturated over most of the image, while the blue channel is noisy. The original images are obtained by absorption, so the vessels appear darker than the background. For the purpose of this enhancement, the contrast of the original image was reversed. It is remarkable that the two parallel vessels near the bottom of the image appear distinct in the enhanced images, although their separation comparable with their

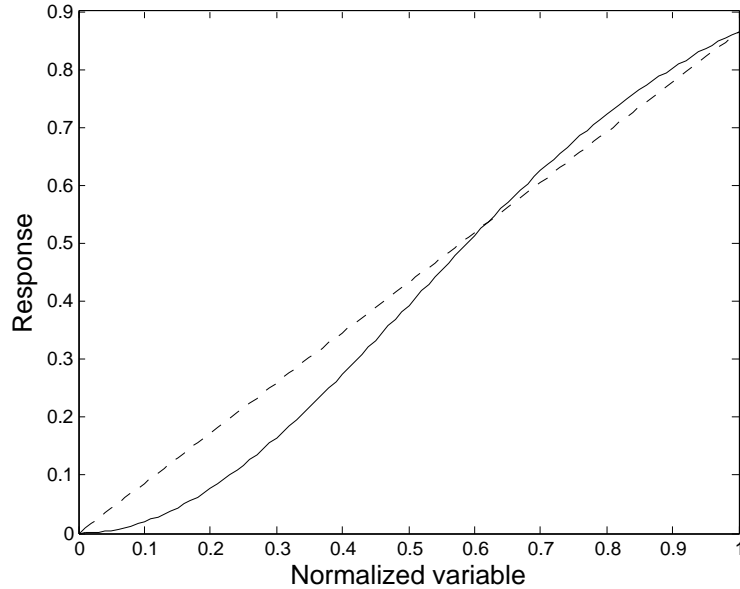


Figure C.2: Transfer function for the Gaussian penalty $1 - \exp(-2x^2)$ (solid line) and the linear transfer x (dashed line)

diameters. Both images were rescaled to a maximum intensity of 1, then amplified by a factor of 2.5 and all values above 1 were set to 1 (since the largest signals are due to the mask, as well as the edge of the optical disk). More of the weaker vessels are visible in the image enhanced with the simple filter of absolute stickness.

Similar results are obtained for 3D images (Figure C.4). The bifurcation is “morphologically correct” - it respects Murray’s cube law and the bifurcation angles (for details, see A). The bifurcation radius ratio is 0.3, approximating the highest area ratio reported in literature of Again, the simple filter for vessel structures (in this case, the plate component of the Hessian tensor) gives comparable results with the full Frangi filter. The main difference is the response at the end of the vessels, much stronger with the simple flatness filter.

The Frangi algorithm stops at this point. However, his approach only uses a small part of the available information. This approach should normally be followed by centerline extraction, similar to the Canny edge detector to extract the centerlines, and by eliminating short, low signal branches (most likely due to accidental grouping of noise pixels). The local direction is required for the directional non-maximum suppression; this is simply the

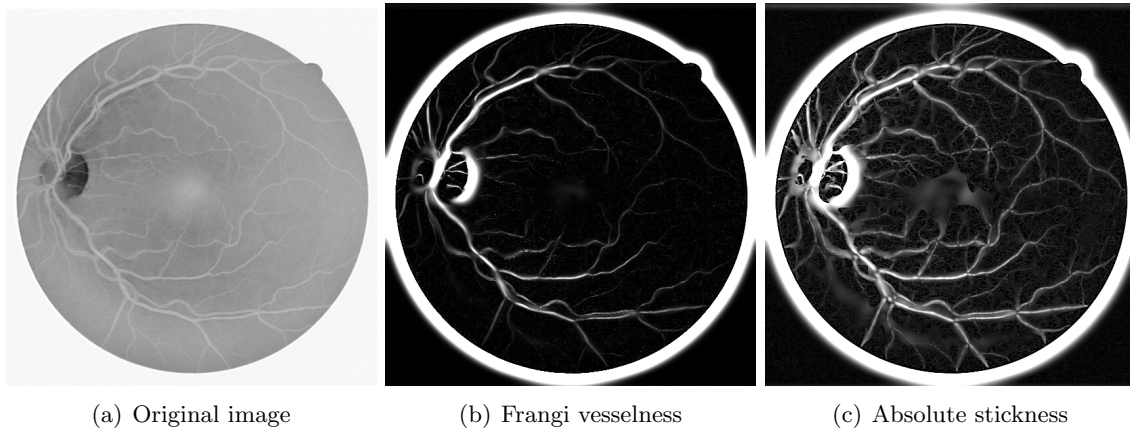


Figure C.3: Comparison of vesselness filters applied to an image from the DRIVE database. From left to right: original image, image filtered with Frangi vesselness, and the multiscale stick.

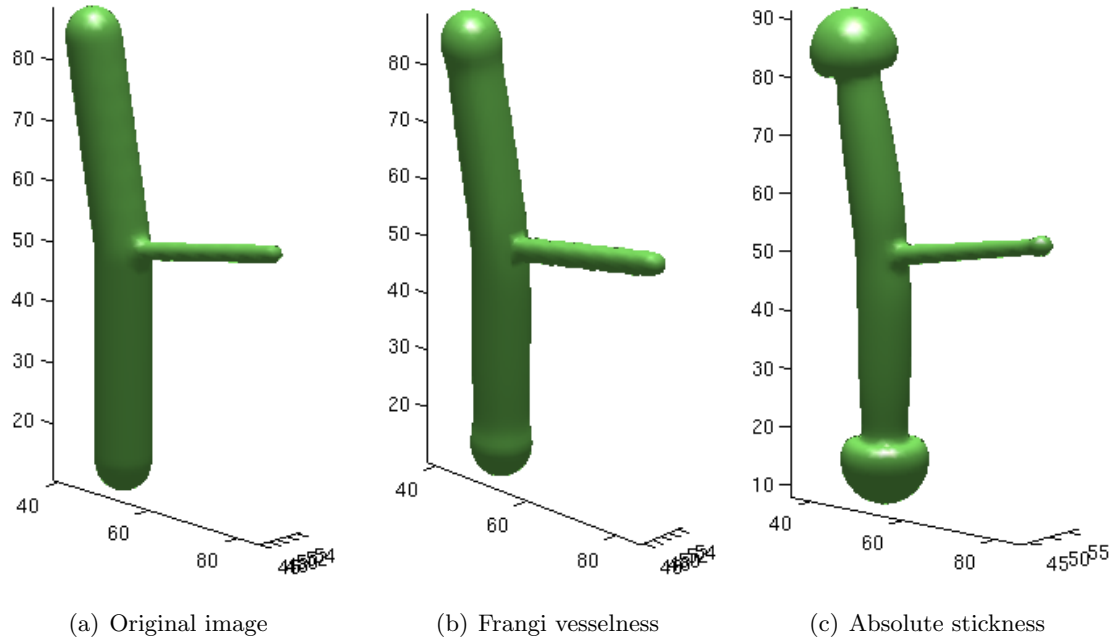


Figure C.4: Comparison of vesselness filters applied to a synthetic 3D bifurcation. From left to right: original image, image filtered with Frangi vesselness, and the multiscale stick.

direction of the eigenvector corresponding to the smallest eigenvalue, \hat{e}_1 . The radius of the vessel can be extracted from another quantity ignored in the original paper, the scale at which the maximum vesselness occurs on the centerline.

The example images also outline the limits of this method. Small vessels, close to the noise limit, are not properly enhanced — especially when they are close to larger vessels. The other limitation, more visible in the DRIVE image, is that the Hessian gives strong responses near edges, giving false positives. As with all scale-space-based methods, the area close to the edges of the image can not be properly processed, even for structures which are quite obvious to the human eye.

Bibliography

- [1] G. Agam, S.G. Armato, and C. Wu. Vessel tree reconstruction in thoracic ct scans with application to nodule detection. *IEEE Transactions on Medical Imaging*, 24(4):486–499, April 2005.
- [2] Shigeo Akimoto, Masako Mitsumata, Toshiyuki Sasaguri, and Yoji Yoshida. Laminar shear stress inhibits vascular endothelial cell proliferation by inducing cyclin-dependent kinase inhibitor. *Circulation Research*, 86:185–190, 2000.
- [3] S.R. Aylward and E. Bullitt. Initialization, noise, singularities, and scale in height ridge traversal for tubular object centerline extraction. *IEEE Transactions on Medical Imaging*, 21(2), February 2002.
- [4] Angelos Barmountis, Baba C. Vemuri, Dena Howland, and John R. Forder. Extracting tractosemas from a displacement probability field for tractography in dw-mri. In *MICCAI '08: Proceedings of the 11th international conference on Medical Image Computing and Computer-Assisted Intervention - Part I*, pages 9–16, Berlin, Heidelberg, 2008. Springer-Verlag.
- [5] Alauddin Bhuiyan, Baikunth Nath, Joselito Chua, and Kotagiri Ramamohanarao. Automatic detection of vascular bifurcations and crossovers from color retinal fundus images. *Signal-Image Technologies and Internet-Based System, International IEEE Conference on*, 0:711–718, 2007.
- [6] Alan C. Bovik, editor. *Handbook of Image and Video Processing (Communications, Networking and Multimedia)*, chapter 4.4, AM-FM Image Models: Fundamental Techniques and Emerging Trends, pages 377–396. Academic Press, Inc., Orlando, FL, USA, 2005.
- [7] E. Buckingham. The principle of similitude. *Nature*, 96:396–397, 1915.
- [8] Juan F. Carrillo, Marcela Hoyos Hernandez, and Maciej Dávila, Eduardo E. and Orkisz. Recursive tracking of vascular tree axes in 3d medical images. *International Journal of Computer Assisted Radiology and Surgery*, 1(6):331–339, April 2007.

- [9] O. Chutatape, L. Zheng, and S.M. Krishnan. Retinal blood vessel detection and tracking by matched gaussian and kalman filters. In *Proceedings of the 20th Annual International Conference of the IEEE Engineering in Medicine and Biology Society*, volume 20, 1998.
- [10] Antonio Colombo. Bifurcational lesions: Searching the solution. *Catheterization and Cardiovascular Interventions*, 65:1718, 2005.
- [11] W.B. Davenport and W.L. Root. *Random Signals and Noise*. McGraw Hill Books Co., NY, 1958.
- [12] Luc M. J. Florack, Bart M. ter Haar Romeny, Jan J. Koenderink, and Max A. Viergever. Scale and the differential structure of images. *Image Vision Comput.*, 10(6):376–388, 1992.
- [13] Alejandro F. Frangi, Wiro J. Niessen, Koen L. Vincken, and Max A. Viergever. Multi-scale vessel enhancement filtering. In *Medical Image Computing and Computer-Assisted Intervention – MICCAI’98*, LNCS, page 130. Springer, 1998.
- [14] Yuan-Cheng Fung. *Biomechanics: circulation*. Springer, 2nd edition, 1997.
- [15] Gösta H. Granlund and Hans Knutsson. *Signal Processing for Computer Vision*. Kluwer Academic Publishers, Norwell, MA, USA, 1995.
- [16] Ghassan Hamarneh and Preet Jassi. Vascusynth: Simulating vascular trees for generating volumetric image data with ground-truth segmentation and tree analysis. *Computerized Medical Imaging and Graphics*, In Press, Corrected Proof:–, 2010.
- [17] C. Harris and M. Stephens. A combined corner and edge detector. In *Proceedings of the 4th Alvey Vision Conference*, pages 147–151, 1988.
- [18] Robert W. Hobson, Samuel E. Wilson, and Frank J. Veith. *Vascular Surgery: principles and practice*. Informa Health Care, 3rd edition, 2003.
- [19] X.Y. Kang, D.H. Liu, J. Zhou, and Y.J. Jin. Simulation of blood flow at vessel bifurcation by lattice boltzmann method. *Chinese Physics Letters*, 22(11):2873–2876, 2005.
- [20] Rudolf Karch, Friederike Neumann, Martin Neumann, and Wolfgang Schreiner. A three-dimensional model for arterial tree representation, generated by constrained constructive optimization. *Computers in Biology and Medicine*, 29:19–38, 1999.
- [21] C. S. Kenney, M. Zuliani, and B.S. Manjunath. An axiomatic approach to corner detection. In *In Proc. of IEEE Conference on Computer Vision and Pattern Recognition*, pages 191–197, 2005.
- [22] Cemil Kirbas and Francis Quek. A review of vessel extraction techniques and algorithms. *ACM Comput. Surv.*, 36(2):81–121, 2004.

- [23] Jan J. Koenderink. The structure of images. *Biological Cybernetics*, 50(5):363–370, August 1984.
- [24] V. Kumar, N. Fausto, and A. Abbas. *Robbins & Cotran Pathologic Basis of Disease*. Elsevier, 7th edition, 2005.
- [25] David Lesage, Elsa D. Angelini, Isabelle Bloch, and Gareth Funka-Lea. A review of 3d vessel lumen segmentation techniques: Models, features and extraction schemes. *Medical Image Analysis*, August 2009.
- [26] Tony Lindeberg. *Scale-Space Theory in Computer Vision*. Kluwer Academic Publishers, Norwell, MA, USA, 1994.
- [27] Tony Lindeberg. Edge detection and ridge detection with automatic scale selection. In *CVPR '96: Proceedings of the 1996 Conference on Computer Vision and Pattern Recognition (CVPR '96)*, page 465, Washington, DC, USA, 1996. IEEE Computer Society.
- [28] Tony Lindeberg. Feature detection with automatic scale selection. *International Journal of Computer Vision*, 30:79–116, 1998.
- [29] David G. Lowe. Object recognition from local scale-invariant features. In *Proceedings of the International Conference on Computer Vision-Volume 2 - Volume 2, ICCV '99*, pages 1150–, Washington, DC, USA, 1999. IEEE Computer Society.
- [30] M. Maddah, H. Soltanian-Zadeh, and A. Afzali-Kushaa. Snake modeling and distance transform approach to vascular centerline extraction and quantification. *Computerized Medical Imaging and Graphics*, 27(6):503–512, 2003.
- [31] H N Mayrovitz and J Roy. Microvascular blood flow: evidence indicating a cubic dependence on arteriolar diameter. *Am J Physiol*, 245(6):H1031–8, 1983.
- [32] C. Mcintosh and G. Hamarneh. Vessel crawlers: 3d physically-based deformable organisms for vasculature segmentation and analysis. In *Computer Vision and Pattern Recognition, 2006 IEEE Computer Society Conference on*, volume 1, pages 1084–1091, 2006.
- [33] Hans Moravec. Sensor fusion in certainty grids for mobile robots. *AI Mag.*, 9(2):61–74, 1988.
- [34] C. D. Murray. The physiological principle of minimum work applied to the angle of branching of arteries. *J. Gen. Physiol.*, 9:835–841, 1926.
- [35] C. D. Murray. The physiological principle of minimum work, i. *Proc. Nat. Acad. Sci.*, 12:207–214, 1926.

- [36] M. Ortega, M.G. Penedo, J. Rouco, N. Barreira, and M.J. Carreira. Retinal verification using a feature points-based biometric pattern. *Journal of Visual Languages and Computing*, 20:8090, 2009.
- [37] Shiqi Ou and Hongzan Bin. Subdivision method to create furcating object with multi-branches. *The Visual Computer*, 21:170–187, 2005.
- [38] T. Pock, R. Beichel, and H. Bischof. A novel robust tube detection filter for 3d centerline extraction. In *Proc Scandinavian Conference on Image Analysis (SCIA)*, volume 3540 of *LNCS*, pages 481–490. Springer, 2005.
- [39] Miranda Poon, Ghassan Hamarneh, and Rafeef Abugharbieh. Live-vessel: Extending livewire for simultaneous extraction of optimal medial and boundary paths in vascular images. In *Medical Image Computing and Computer-Assisted Intervention (MICCAI)*, *LNCS*, pages 444–451, 2007.
- [40] William H. Press, Saul A. Teukolsky, William T. Vetterling, and Brian P. Flannery. *Numerical Recipes in C*. Cambridge University Press, 2nd edition, 1992.
- [41] Rémi Revellin, cois Rousset, Fran David Baud, and Jocelyn Bonjour. Extension of murray’s law using a non-newtonian model of blood flow. *Theoretical Biology and Medical Modelling*, 6(1):7, 2009.
- [42] Jianbo Shi and Carlo Tomasi. Good features to track. In *In Proc. of IEEE Conference on Computer Vision and Pattern Recognition*, pages 593–600, 1994.
- [43] David S. Tuch. Q-ball imaging. *Magnetic Resonance in Medicine*, 52:1358–1372, 2004.
- [44] H.B.M. Uylings. Optimization of diameters and bifurcation angles in lung and vascular tree structures. *Bulletin of Mathematical Biology*, 39:509–520, 1977.
- [45] A.P. Yoganathan and G.P. Chatzimavroudis. *Hemodynamics*, pages 138–151. Springer, 2002.
- [46] M. Zamir. Optimality principles in arterial branching. *Journal of Theoretical Biology*, 62:227–251, 1976.
- [47] M. Zamir. Nonsymmetrical bifurcations in arterial branching. *Journal of General Physiology*, 72:837–845, 1978.
- [48] M. Zamir, J.A. Medeiros, and T.K. Cunningham. Arterial bifurcations in the human retina. *Journal of General Physiology*, 74:537–548, 1979.
- [49] M. Zamir, S.M. Wrigley, and B.L. Langille. Arterial bifurcations in the cardiovascular system of a rat. *Journal of General Physiology*, 81:325–335, 1983.

- [50] D.P. Zarins, C.K. and Giddens, B.K. Bharadvaj, V.S. Sottiurai, R.F. Mabon, and S. Glagov. Carotid bifurcation atherosclerosis. quantitative correlation of plaque localization with flow velocity profiles and wall shear stress. *Circulation research*, 53(4):502-514, 1983.
- [51] J. Zhou, S. Chang, D. Metaxas, and L. Axel. Vascular structure segmentation and bifurcation detection. In *Biomedical Imaging: From Nano to Macro, ISBI 2007*, pages 872–875, 2007.